NONLINEAR OPTICAL EFFECTS AND THEIR APPLICATIONS: FROM PARAMETRIC AMPLIFICATION IN COUPLED WAVEGUIDES TO MODULATION INSTABILITIES IN FIBRE RING RESONATORS

Minji Shi

Doctor of Philosophy

ASTON UNIVERSITY

July 2025

Abstract

Nonlinear optical effects and their applications: from parametric amplification in coupled waveguides to modulation instabilities in fibre ring resonators
Minji Shi
Doctor of Philosophy
2025

This thesis investigates nonlinear optical phenomena in two coupled waveguides and fibre ring resonators, with a particular emphasis on optical parametric amplification (OPA), modulation instability (MI), and optical frequency comb (OFC) generation. The work is divided into two parts.

The first part investigates OPA in dual-core waveguide systems. By exploiting coupling-induced dispersion, we demonstrate flexible dispersion engineering that enables broadband gain, even in normally dispersive waveguides. Analytical and numerical models are developed to assess the impact of pump power and phase fluctuations on system stability. Additionally, we explore intermodal four-wave mixing in dual-core fibres, revealing how frequency-dependent coupling and power imbalance between the waveguides lead to asymmetric gain and signal–idler separation into distinct supermodes. These findings offer design strategies for efficient, robust, and tunable amplifiers in both fibre and integrated photonic platforms.

The second part focuses on MI in nonlinear optical resonators. We study filter-induced MI in a fibre ring cavity with an intracavity amplifier, demonstrating enhanced MI and efficient energy transfer to spectral sidebands. In parametrically driven resonators with quadratic nonlinearity, we analyse filter-induced MI and show its role in enabling tunable OFC generation. Furthermore, we uncover a new dynamical regime in Kerr resonators: period-4 MI, characterised by temporal patterns repeating every four cavity round trips. Analytical gain expressions are derived and validated through numerical simulations.

Together, these results advance the understanding and control of nonlinear wave dynamics in optical systems, providing novel mechanisms for amplification, frequency conversion, and complex temporal pattern formation, with implications for both fundamental science and practical photonic technologies.

Keywords:
Nonlinear optics, Parametric amplification, Coupling dispersion, Modulation instability, Ring resonators, Gain-through-filtering instability, Optical frequency comb

Personal Acknowledgements

First, I would like to express my sincere gratitude to my supervisor, Prof. Auro M. Perego, for guiding me from the fundamentals to advanced concepts in nonlinear optics, for inspiring me with his unwavering passion for research, for encouraging me to network and collaborate more, and for granting me great freedom—not only in exploring topics within the broader scope of my PhD but also in how and where I work.

I acknowledge all my collaborators, Dr. Stefano Negrini, Prof. Matteo Conforti, Prof. Arnaud Mussot, Dr. Nicolas Englebert, Prof. François Leo, Prof. Dmitry V. Skryabin, Dr. Vitor Ribeiro, Dr. Morteza Kamalian-Kopae for their valuable contributions and insightful discussions. I have learned a great deal from their expertise, perspectives, and problem-solving approaches. Their guidance and generosity in sharing knowledge have been an important part of my academic growth.

I would like to thank all my colleagues in the office—Negar Shaabani Shishavan, Dini Pratiwi, Mariia Bastamova, Stepan Bogdanov, Long Nguyen, Sasipim Srivallapanondh, Geraldo Gomes De Luna Junior, Wesley Melo, and Rana Ahmad Bilal Khalid—as well as our group member Alberto Rodriguez Cuevas and the Student Chapter organisers, Karina Nurlybayeva and Aisha Bibi, for contributing to a friendly and intellectually stimulating environment.

I would also like to acknowledge the use of OpenAI's ChatGPT to help improve the readability, grammar, and spelling of the English in this thesis.

I am grateful to all my old friends for consistently sharing their interesting stories and for always being there to listen to mine—it has made everyday life more enjoyable and meaningful.

Finally, I would like to express my deepest gratitude to my parents. Although pursuing an academic path abroad was not their wish, they have never stopped supporting, under-

standing, and encouraging me. Their unconditional belief in me, despite the distance and uncertainty, has been a constant source of strength throughout this journey.

List of Publications

Publications Arising from this Thesis:

[1] M. Shi, V. Ribeiro, and A. M. Perego. Parametric amplification in coupled nonlinear waveguides: the role of coupling dispersion. *Front. Photon.*, 4:1051294, 2023.

[2] M. Shi, V. Ribeiro, and A. M. Perego. On the resilience of dual-waveguide parametric amplifiers to pump power and phase fluctuations. *Appl. Phys. Lett.*, 122(10):101102, 2023.

[3] M. Shi, V. Ribeiro, and A. M. Perego. Parametric amplification based on intermodal four-wave mixing between different supermodes in coupled-core fibers. *Opt. Express*, 31(6): 9760–9768, 2023.

[4] M. Shi, M. Conforti, A. Mussot, and A. M. Perego. Period-4 modulation instability in ring fiber cavities. *Phys. Rev. A*, 111(1):013513, 2025.

[5] M. Shi, N. Englebert, F. Leo, D. V. Skryabin, and A. M. Perego. Modulation instability and frequency comb generation in hybrid quadratic-cubic resonators with spectral filter. *Phys. Rev. A*, 112(2):023522, 2025.

[6] M. Shi, S. Negrini, N. Englebert, F. Leo, M. Conforti, A. Mussot, and A. M. Perego. Amplifier enhanced gain-through-filtering instability in a hybrid kerr cavity. *Opt. Express*, 33(21):43665–43675, 2025.

Additional Publications Completed During my Studies:

[7] V. Ribeiro, M. Shi, and A. M. Perego. Impact of zero-dispersion wavelength fluctuations in a coupled dual-core fiber optical parametric amplifier. *J. Lightwave Technol.*, 41(19): 6235–6243, 2023.

[8] M. Gong, M. Shi, Y. Li, X. Xu, Z. Fei, Y. Qiao, J. Liu, A. He, and X. Liu. Resonant adhesion structure makes negative acoustic radiation force. *Phys. Fluids*, 35(5), 2023.

Contents

Chapter 1

Introduction

Nonlinear optics plays a foundational role in modern photonics, enabling the manipulation of light through intensity-dependent material responses. Among the wide array of nonlinear phenomena, optical parametric amplification (OPA) and modulation instability (MI) are particularly significant due to their applications in signal processing, frequency conversion, and the generation of complex optical states. These effects are central to the operation of devices ranging from amplifiers and oscillators to optical frequency comb (OFC) sources. This thesis investigates nonlinear optical effects across two main platforms—coupled waveguides and fibre ring resonators—focusing on OPA in two coupled waveguides and on the onset and control of MI in fibre ring resonators. In certain regimes, MI also give rise to OFCs, which are explored where relevant.

Before starting the two main topics, in Chapter 2, we introduce the fundamental concepts underlying nonlinear light propagation in guided-wave systems, including key properties of the media: optical loss, chromatic dispersion, and nonlinearities. Then, we formulate the governing pulse-propagation equations in nonlinear dispersive media. And finally, we introduce the four-wave mixing and its applications, including OPA and MI.

In the first part, we first introduce the basic theory utilised for dual-waveguide OPA and emphasise the benefits of using two coupled waveguides for OPA in Chapter 3. Then in Chapter 4, we study the impact of the coupling dispersion on dual-waveguide OPA. Chapter 5 is dedicated to a stability analysis of equally pumped waveguides under fluctuations in relative input power and phase, showing that the amplification scheme remains robust under realistic perturbations. Lastly, in Chapter 6, we investigate intermodal FWM in

dual-core fibres, where frequency-dependent coupling and power imbalance between waveguides lead to asymmetric gain and signal–idler separation into distinct supermodes. These studies establish a theoretical foundation for robust, broadband, and efficient parametric amplification in both fibre and integrated photonic platforms.

In the second part of the thesis, we shifts our focus to MI and OFC generation in fibre ring resonators. Starting with Chapter 7, we introduce the basic models used for describing wave propagation in fibre ring resonators: Ikda map and Lugiato–Lefever equation (LLE), and also the gain-through-filtering (GTF) mechanism. In Chapter 8, we study a GTF cavity with an integrated erbium-doped fibre amplifier (EDFA). This intracavity gain enhances resonator finesse and reduces the threshold for MI onset, leading to more efficient energy transfer to spectral sidebands. In Chapter 9, we analyse MI in parametrically driven ring resonators, where filter-induced spectral asymmetries induce instabilities and, under certain conditions, form OFC. Finally, in Chapter 10, we explore a highly nonlinear regime of Kerr resonators by investigating period-4 (P4) MI—a previously unreported dynamics where the intracavity temporal pattern repeats after four round trips. We derive analytical expressions for the P4 MI gain and verify them via numerical simulations, highlighting new dynamical behaviours in resonators beyond stationary continuous-wave states.

Overall, this thesis presents a unified investigation of nonlinear optical effects—particularly MI and OPA—across guided-wave and resonator platforms. It reveals how coupling, dispersion, and nonlinearities can be harnessed to control MI and enable advanced functionalities such as broadband amplification, frequency conversion, and comb generation. The analytical models and numerical methods developed here provide a foundation for the future design of nonlinear photonic devices with tailored spectral and temporal properties.

Chapter 2

Light propagation in nonlinear media

2.1 Introduction

The propagation of optical pulses in fibres and waveguides is fundamentally governed by the interplay of several key physical effects: attenuation, chromatic dispersion, and optical nonlinearity. Each of these processes plays a distinct role in shaping the temporal and spectral dynamics of light as it travels through a nonlinear dispersive medium. A comprehensive understanding of these effects is essential for designing and optimising photonic systems used in applications ranging from telecommunications to frequency comb generation and ultrafast signal processing.

Losses in optical media lead to an exponential attenuation of the optical signal and set fundamental limits on transmission distance and amplification requirements.

Chromatic dispersion, on the other hand, plays a fundamental role in shaping the dynamics of pulses as they propagate through optical media. When a pulse consists of a broad spectrum of frequency components, any frequency-dependent variation in propagation speed leads to distortion and temporal spreading, which can critically affect the performance of optical communication systems and nonlinear optical processes. Understanding and quantifying this dispersion is essential for designing waveguides and fibres that either minimise pulse distortion or exploit dispersion effects for specific functionalities such as soliton formation or supercontinuum generation [9].

Optical nonlinearity arises from the interaction of intense light fields with a medium, leading to a nonlinear polarisation response. In macroscopic media this response is conveniently described by expanding the polarisation in powers of the electric field, which gives rise to different orders of nonlinear susceptibilities. Two major classes are commonly encountered in guided-wave optics: second-order ($\chi^{(2)}$) and third-order ($\chi^{(3)}$) effects. $\chi^{(2)}$ nonlinearities occur in non-centrosymmetric materials and underlie processes such as second-harmonic generation (SHG), sum- and difference-frequency generation, and optical parametric amplification (OPA). Third-order nonlinearities are present in all materials and include the instantaneous Kerr effect, which gives rise to self-phase modulation (SPM), cross-phase modulation (XPM), and four-wave mixing (FWM), as well as inelastic processes such as stimulated Raman and Brillouin scattering in optical fibres. In semiconductor waveguides, the third-order response also encompasses two-photon absorption (TPA) and the subsequent free-carrier dispersion (FCD) and free-carrier absorption (FCA).

In this thesis we are primarily concerned with refractive nonlinearities that can be modelled by real susceptibilities, in particular the Kerr effect and related parametric interactions, treated within effective $\chi^{(2)}$ and $\chi^{(3)}$ frameworks. Other nonlinear mechanisms—Raman and Brillouin scattering in fibres, and carrier-related effects induced by two-photon absorption in semiconductors—are relevant in many practical situations and can significantly modify the phase matching and gain characteristics. However, their detailed treatment lies outside the scope of the pulse propagation models and analytical results developed in this thesis, and they will be mentioned only briefly for completeness.

To model the evolution of pulses under the combined influence of dispersion and nonlinearity, a central framework is the nonlinear Schrödinger equation (NLSE) and its generalisations [9, 10]. These pulse-propagation equations allow the prediction and analysis of complex behaviours including soliton formation, supercontinuum generation, and instability dynamics.

Among the various nonlinear interactions, FWM is of particular interest due to its broad range of applications in wavelength conversion, parametric amplification, and OFC generation. FWM involves the coherent mixing of multiple optical fields to generate new frequency components, with its efficiency governed by phase-matching conditions, dispersion, and nonlinear interaction length.

This chapter introduces each of these fundamental physical effects in detail, establishing

the groundwork for understanding complex pulse dynamics and nonlinear optical processes in modern photonic systems.

2.2 Losses

Losses in optical fibres and integrated waveguides arise primarily from absorption, scattering, and radiation. These losses are typically quantified by the attenuation coefficient α, measured in units of km^{-1} or cm^{-1}, depending on the platform. The transmitted power $P(z)$ along the propagation direction z decays exponentially as $P(z) = P(0)e^{-\alpha z}$, where $P(0)$ is the input power [9]. In practice, the attenuation is often expressed in decibels per unit length using

$$\alpha_{\mathrm{dB}} = \frac{10}{z}\log_{10}\left(\frac{P(0)}{P(z)}\right) = \frac{10}{\ln 10}\alpha \approx 4.34\alpha. \tag{2.1}$$

In optical fibres, the dominant loss mechanisms include Rayleigh scattering and material absorption, with typical losses as low as 0.2 dB/km at 1550 nm [9]. In integrated waveguides, propagation losses depend strongly on the material platform and fabrication process. Silicon photonics waveguides often exhibit losses in the range of 1–10 dB/cm due to sidewall roughness, strong modal confinement, and two-photon-absorption-related effects [11]. In contrast, silicon nitride waveguides benefit from a wide bandgap and negligible two-photon absorption in the near-infrared, enabling substantially lower propagation losses. Early or less-optimised silicon nitride platforms typically exhibit losses on the order of 0.1 dB/cm [12], while modern low-loss platforms employing optimised geometries and high-temperature annealing have demonstrated propagation losses well below 10 dB/m, approaching the sub-dB/m regime [13]. For the purposes of illustration in later chapters, this thesis adopts a propagation loss of 3 dB/m for silicon nitride, which lies within the performance envelope of contemporary low-loss platforms while remaining a conservative and realistic value for practical integrated waveguide devices.

2.3 Chromatic dispersion

Chromatic dispersion arises from the frequency dependence of the propagation constant $\beta(\omega)$, which governs the phase evolution of a wave in a medium. This frequency dependence leads to different spectral components of a light pulse travelling at different phase

velocities, resulting in temporal broadening of pulses during propagation [9]. In optical media, $\beta(\omega)$ is related to the refractive index $n(\omega)$ by $\beta(\omega) = \frac{n(\omega)\omega}{c}$, where c is the speed of light in vacuum. The frequency dependence of $n(\omega)$ gives rise to material dispersion. In waveguides, however, dispersion also arises from the geometric structure and modal confinement—known as waveguide dispersion—which can cause the effective refractive index to vary with frequency even if the material itself is dispersionless. To characterise overall dispersion, $\beta(\omega)$ is typically expanded in a Taylor series around a central angular frequency ω_0:

$$\beta(\omega) = \sum_{n=0}^{\infty} \frac{\beta_n}{n!}(\omega - \omega_0)^n, \tag{2.2}$$

where $\beta_n \equiv \frac{d^n\beta}{d\omega^n}\Big|_{\omega_0}$. Specifically $\beta_1 = \frac{d\beta}{d\omega}\Big|_{\omega_0}$ corresponds to the inverse group velocity, and $\beta_2 = \frac{d^2\beta}{d\omega^2}\Big|_{\omega_0}$ is the group velocity dispersion (GVD) parameter. A positive β_2 indicates normal dispersion, while a negative β_2 corresponds to anomalous dispersion.

2.4 Nonlinearity

Nonlinearity in optical media arises when the response of the material to an applied electric field becomes non-proportional to the field strength, typically at high optical powers [9, 10]. This behaviour is described by expanding the material's polarisation $\mathbf{P}$ as a power series in the electric field $\mathbf{E}$:

$$\mathbf{P}(\mathbf{r}, t) = \epsilon_0(\chi^{(1)} \cdot \mathbf{E} + \chi^{(2)} : \mathbf{EE} + \chi^{(3)} \vdots \mathbf{EEE} + \ldots), \tag{2.3}$$

where ε_0 is the vacuum permittivity, and $\chi^{(n)}$ are the n-th order susceptibilities.

In non-centrosymmetric materials such as lithium niobate ($LiNbO_3$), the second-order susceptibility $\chi^{(2)}$ is nonzero and enables efficient second-order nonlinear effects, including SHG, sum-frequency generation, and difference-frequency generation. A popular engineered variant, periodically poled lithium niobate (PPLN), achieves quasi-phase matching by periodically inverting the material's crystal orientation, greatly enhancing $\chi^{(2)}$-based interactions [14].

In contrast, in centrosymmetric materials such as silica glass, $\chi^{(2)} = 0$ due to inversion symmetry, and the dominant nonlinearity is the third-order susceptibility $\chi^{(3)}$. This gives rise to the Kerr nonlinearity, where the refractive index depends on the optical intensity: $n =$

$n_0 + n_2 I$. Here, n_0 is the linear refractive index while n_2 (Kerr coefficient) is the nonlinear refractive index related to $\chi^{(3)}$. Kerr nonlinearity leads to phenomena such as SPM, XPM, FWM, which are fundamental in nonlinear fibre optics, supercontinuum generation, and OPA.

Beyond the $\chi^{(2)}$ and instantaneous $\chi^{(3)}$ responses described above, optical media exhibit additional third-order nonlinear processes that can influence propagation depending on the material platform. In silica fibres, stimulated Raman and Brillouin scattering arise from delayed vibrational and acoustic contributions to $\chi^{(3)}$, which introduce frequency-dependent gain and can significantly modify the effective nonlinear response, phase-matching condition, and parametric gain spectrum. Such Raman-induced modifications to optical parametric amplification dynamics have been analysed in birefringent fibres [15], and related effects have been experimentally characterised in the scalar case [16, 17].

In semiconductor waveguides, TPA and the subsequent generation of free carriers lead to FCD and FCA, producing dynamic and absorptive contributions to the effective nonlinearity [18]. These mechanisms become relevant at high optical intensities or in materials with strong two-photon absorption.

While these nonlinear processes are important in many practical contexts, the models developed in this thesis focus primarily on refractive Kerr-type interactions governed by the real part of $\chi^{(3)}$. The scattering-induced and carrier-related nonlinearities mentioned above are therefore not included in the pulse-propagation equations analysed in subsequent sections.

2.5 Pulse-propagation equations in nonlinear dispersive media

In the slowly varying envelope approximation [9], and considering a single transverse mode, it can be derived from Maxwell's equations that the propagation of a polarised optical pulse envelope $A(z,t)$ in a Kerr medium with third-order nonlinearity is governed by the NLSE:

$$\partial_z A = -\frac{\alpha}{2}A - i\frac{\beta_2}{2}\partial_t^2 A + i\gamma(\omega_0)|A|^2 A. \tag{2.4}$$

Here, t denotes the retarded time defined as $t = \tau - \beta_1 z$, with τ being the laboratory time. $\gamma(\omega_0) = \frac{n_2\omega_0}{cA_{\text{eff}}}$ is the nonlinear coefficient, and A_{eff} is the effective mode area determined by the transverse profile of the guided mode. The NLSE is derived under the assumption that the optical field is narrowly centered around a single carrier frequency ω_0, and that all nonlinear interactions of interest occur near this frequency. Although the third-order nonlinear polarisation $P^{(3)}(t) \propto E^3(t)$ generates multiple frequency components—including ω_0, $3\omega_0$, and others—only the component near ω_0 is retained using the rotating wave approximation. Higher-frequency terms, such as third-harmonic generation, are strongly phase-mismatched in typical Kerr media and are neglected in the single-frequency envelope model. This leads to a single governing equation that captures the dominant effects of degenerate four-wave mixing originating from the interaction of spectral components within a single pulse. A more detailed derivation can be found in Appendix A.

In contrast, second-order nonlinear processes inherently involve coupling between different frequency components. In a $\chi^{(2)}$ medium, the second-order polarisation $P^{(2)}(t) \propto E^2(t)$ results in frequency doubling, such that a fundamental wave at frequency ω_0 generates a second-harmonic (SH) wave at $2\omega_0$. Consequently, the optical field must be represented as a sum of two distinct frequency components, and their envelopes must be modeled separately. The slowly varying envelopes of the fundamental field $A(z,t)$ and its SH field $B(z,t)$ obey the following coupled equations [10, 19]:

$$\partial_z A = \left[-\frac{\alpha_{\omega_0}}{2} - i\frac{\beta_2(\omega_0)}{2}\partial_t^2\right] A + i\kappa B A^* e^{-i\Delta\beta z}, \tag{2.5a}$$

$$\partial_z B = \left[-\frac{\alpha_{2\omega_0}}{2} - \Delta\beta_1\partial_t - i\frac{\beta_2(2\omega_0)}{2}\partial_t^2\right] B + i\kappa A^2 e^{i\Delta\beta z}, \tag{2.5b}$$

where α_{ω_0} and $\alpha_{2\omega_0}$ are the attenuation coefficients at the respective frequencies, $\Delta\beta = 2\beta(\omega_0) - \beta(2\omega_0)$ is the phase mismatch, and $\Delta\beta_1 = \beta_1(2\omega_0) - \beta_1(\omega_0)$ denotes the group-velocity mismatch (GVM). The coupling coefficient is given by $\kappa = \frac{2\omega_0 d_{\text{eff}}}{n(2\omega_0)c}$, with d_{eff} being the effective second-order nonlinear coefficient and $n(2\omega_0)$ the refractive index at the harmonic frequency. Unlike in the $\chi^{(3)}$ case, here both frequencies lie within the range of interest and must be explicitly included. The SH field is not merely a small perturbation—it evolves dynamically and exchanges energy with the fundamental wave. Even in the absence of perfect phase matching, the SH field is still locally generated, and the system exhibits phenomena such as oscillatory energy transfer, back-conversion, and temporal

walk-off [9, 10].

2.6 Four-wave mixing and its application

FWM is a nonlinear optical process involving the interaction of four photons, typically enabled by third-order Kerr nonlinearity, where at least two input frequencies are involved. In this process, energy and momentum are exchanged among four interacting photons, typically resulting in the generation of new frequency components [10, 20, 21, 22, 23]. In the degenerate FWM, two input waves share the same frequency, making the process more efficient and easier to implement experimentally. FWM-like phenomena can also arise in second-order nonlinear media through cascaded processes such as phase-mismatched SH generation, which induce an effective third-order response [24, 19, 25].

Depending on whether the process is externally seeded or arises spontaneously, it enables a variety of optical phenomena. In the externally seeded case of FWM, the process is used for OPA and wavelength conversion (WLC), while the spontaneous case gives rise to MI, where no input signal is required.

In this thesis, we focus exclusively on the single-pump degenerate FWM. Using the lossless fibre case ($\alpha = 0$) as an example, we study the evolution equation of the sidebands, beginning with the following ansatz:

$$A(z,t) = A_p(z) + \epsilon(z,t), \tag{2.6}$$

where $A_p(z,t) = \sqrt{P}e^{i\gamma Pz + i\phi_0}$ represents an undepleted pump wave, with the pump power denoted by P and the initial phase by ϕ_0, and $\epsilon(z,t)$ accounts for all other components, mostly the sidebands. Substituting Eq. (2.6) into Eq. (2.4) and considering the small sideband approximation $|\epsilon(z,t)|^2 \ll P$, we obtain the two linearly coupled equations governing the evolution of ϵ,

$$\partial_z \epsilon(z,t) = -i\frac{\beta_2}{2}\partial_t^2 \epsilon(z,t) + i\gamma 2P\epsilon(z,t) + i\gamma P e^{i2(\gamma Pz+\phi_0)}\epsilon^*(z,t). \tag{2.7}$$

If we define η by $\epsilon(z,t) = \eta(z,t)e^{i\gamma Pz+i\phi_0}$, Eq. (2.7) can be rewritten as

$$\partial_z \eta(z,t) = -i\frac{\beta_2}{2}\partial_t^2 \eta(z,t) + i\gamma P\eta(z,t) + i\gamma P\eta^*(z,t). \tag{2.8}$$

Performing a Fourier transform on Eq. (2.8), we obtain

$$\partial_z \begin{pmatrix} \hat{\eta}(z,\Omega) \\ \hat{\eta}^*(z,-\Omega) \end{pmatrix} = M \begin{pmatrix} \hat{\eta}(z,\Omega) \\ \hat{\eta}^*(z,-\Omega) \end{pmatrix} = \begin{pmatrix} i\frac{\beta_2}{2}\Omega^2 + i\gamma P & i\gamma P \\ -i\gamma P & -i\frac{\beta_2}{2}\Omega^2 - i\gamma P \end{pmatrix} \begin{pmatrix} \hat{\eta}(z,\Omega) \\ \hat{\eta}^*(z,-\Omega) \end{pmatrix}. \tag{2.9}$$

which takes the form of the Bogoliubov-de Gennes equation. The matrix M determines the propagation of sidebands in a fibre while neglecting pump depletion, and has the eigenvalues $\pm\lambda$ with $\lambda(\Omega) = \sqrt{-(\frac{\beta_2}{2}\Omega^2 + \gamma P)^2 + (\gamma P)^2}$. Only if $\lambda(\Omega)$ is real-valued will the wave at frequency Ω grow exponentially, that is, become amplified. Two straightforward conclusions follow: the exponential growth of sidebands occurs exclusively in the anomalous dispersion regime ($\beta_2 < 0$); the maximum gain is achieved when $\frac{\beta_2}{2}\Omega^2 + \gamma P = 0$, which corresponds to the wavevector relation $k(\Omega) + k(-\Omega) - 2k(0) + 2\gamma P = 0$, where the term $2\gamma P$ represents the total nonlinear phase shift induced by Kerr self- and cross-phase modulation of the pump and sidebands. This is the nonlinear phase-matching condition that ensures efficient four-wave mixing.

More generally, phase matching is the central requirement for efficient parametric processes such as OPA and MI. In different platforms it can be achieved by exploiting birefringence, modal phase matching in multimode structures, quasi-phase matching, or longitudinal modulation of the dispersion. In the scalar Kerr fibre system considered here, however, phase matching is provided self-consistently by the nonlinear phase shifts associated with the strong pump. The modulational-instability regime discussed below corresponds to the spontaneous case in which this Kerr-induced phase-matching condition is satisfied, whereas OPA and wavelength conversion represent externally seeded implementations of the same underlying four-wave-mixing process.

2.6.1 Parametric amplification and wavelength conversion

In a single-pump OPA or wavelength-conversion scheme, a strong pump wave is injected into the nonlinear medium along with a weaker input signal at a different frequency [26, 27, 28]. Through the nonlinear interaction, energy is transferred from the pump to both the signal and a newly generated idler wave. This coherent energy transfer conserves both

energy and momentum, and the phase-matching condition ensures efficient conversion [26, 21]. Because the process is inherently phase-coherent and adds only the quantum-limited vacuum noise, OPA and WLC are attractive for low-noise optical communications and signal-processing functions. Moreover, the same functionalities have been demonstrated in silicon and silicon-nitride waveguides, which are promising candidates for OPA and WLC in integrated devices [29, 30].

The gain of the OPA is defined as the ratio of the signal output power at propagation distance $z = L$ to its input power at $z = 0$, while the efficiency of WLC is defined as the ratio of the idler output power at propagation distance $z = L$ to the signal input power at $z = 0$. Both OPA and WLC can be categorised into phase-sensitive (PS) and phase-insensitive (PI) cases based on the presence of an injected idler wave. In the PS case, the idler is injected alongside the signal, and their relative phases influence the parametric gain. In contrast, the PI case does not involve any idler injection. In both scenarios, assuming that the signal is blue-detuned, the parametric gain and WLC efficiency can be calculated by

$$G(L,\Omega) = \begin{cases} |\hat{\epsilon}(L,\Omega)|^2/|\hat{\epsilon}(0,\Omega)|^2 = |\hat{\eta}(L,\Omega)|^2/|\hat{\eta}(0,\Omega)|^2 & \text{OPA} \\ |\hat{\epsilon}(L,-\Omega)|^2/|\hat{\epsilon}(0,\Omega)|^2 = |\hat{\eta}(L,-\Omega)|^2/|\hat{\eta}(0,\Omega)|^2 & \text{WLC} \end{cases} \tag{2.10}$$

where $\hat{\eta}(L,\pm\Omega)$ can be determined by the following equation for any propagation distance L:

$$\begin{pmatrix} \hat{\eta}(L,\Omega) \\ \hat{\eta}^*(L,-\Omega) \end{pmatrix} = e^{ML} \begin{pmatrix} \hat{\eta}(0,\Omega) \\ \hat{\eta}^*(0,-\Omega) \end{pmatrix}, \tag{2.11}$$

where $e^{ML} = \cosh(\lambda L)\mathcal{I} + \frac{\sinh(\lambda L)}{L}M$, with $\mathcal{I}$ being the identity matrix [27]. A typical parametric gain profile in the anomalous dispersion regime is illustrated in Fig. 2.1, corresponding to a propagation distance of $L = 0.1$ km. The sidebands around ± 1.7 THz are amplified, which is as required by the phase-matching condition. We find that the analytical predictions, which disregard pump depletion, align perfectly with the simulation results of the NLSE that incorporate pump depletion.

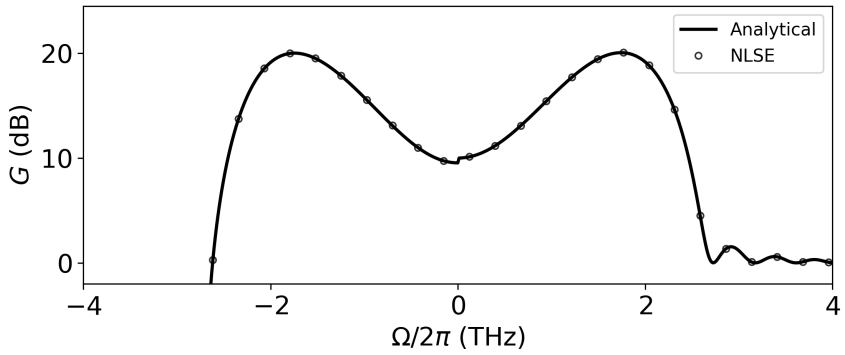

Figure 2.1: The gain profile of a fibre-based OPA. Parameters used are $\gamma = 10$ W^{-1}km^{-1}, $\beta_2 = -0.5$ ps^{2}km^{-1}, $P = 3$ W, and $L = 0.1$ km.

2.6.2 Modulation instability

The spontaneous case of FWM leads to MI, where no input signal is required beyond a strong pump. Small perturbations, including quantum fluctuations and intrinsic noise in the medium, are exponentially amplified through the nonlinear interaction, causing the breakup of a continuous wave (CW) into a train of pulses and the formation of symmetric sidebands around the pump frequency [31, 32].

MI was initially regarded as a drawback in the context of fibre–optic telecommunications, because it converts phase or amplified-spontaneous-emission noise into intensity fluctuations, raising the noise figure and imposing power limits on CW transmission [9]. However, it has since become a valuable tool in unseeded systems aimed at generating OFCs [33, 34, 35], which are light sources whose spectra consist of a series of discrete, equally spaced frequency lines, resembling the teeth of a comb. In these cases, a strong continuous-wave pump propagating in a fibre with anomalous dispersion spontaneously breaks up into symmetric sidebands due to MI, which then seed cascaded FWM. This leads to the formation of a comb-like spectrum with regularly spaced frequency components. When proper phase coherence is maintained—either through pump stabilisation or by embedding the fibre in a cavity—the result can be a true OFC [36, 37], suitable for applications in spectroscopy, metrology, and optical clocks [38, 39]. More broadly, MI is now recognised as a universal phenomenon arising from the NLSE; it occurs not only in optics but also in systems such as Bose–Einstein condensates, plasmas, and hydrodynamic fluids [40, 41, 42], wherever the balance between dispersion and nonlinearity gives rise to instability and pattern formation.

The gain of MI is typically defined in terms of unit length, or sometimes per round trip in the case of resonators. For the dynamics described by Eq. (2.9), the MI gain is usually defined as the maximum eigenvalue of the dynamics matrix M, i.e., $g(\Omega) = 2\mathrm{Re}[\lambda(\Omega)]$, or in decibels per unit length,

$$g_{\mathrm{dB}}(\Omega) = \frac{20}{\ln 10}\mathrm{Re}[\lambda(\Omega)]. \tag{2.12}$$

The MI gain profile for a fibre in the anomalous dispersion regime is illustrated in Fig. 2.2. It is worth commenting on the behaviour at zero frequency detuning. The eigenvalue of matrix M is zero at $\Omega = 0$, so the MI gain $g_{\mathrm{dB}}(\Omega = 0)$ vanishes. In this sense there is no exponential modulational instability exactly at the carrier frequency, in agreement with the standard scalar theory [27]. However, the OPA gain defined in Eq. (2.10) is a finite-length power ratio. At $\Omega = 0$ the linearised evolution matrix becomes nilpotent ($M^2 = 0$), so that $e^{ML} = \mathcal{I} + LM$. For a simple initial condition with a small perturbation at $\Omega = 0$, this leads to $G(L, 0) \simeq 1 + (\gamma PL)^2 > 1$, i.e., a weak polynomial increase with propagation distance rather than an exponential growth. The non-zero value of $G(L, 0)$ in Fig. 2.1 should therefore be interpreted as a finite-length, phase-sensitive mixing effect, not as evidence of a genuine MI sideband at zero frequency.

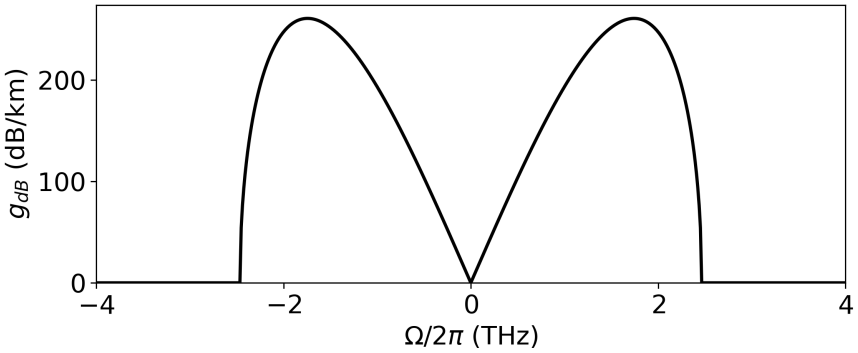

Figure 2.2: The MI gain profile in a fibre. Parameters used are $\gamma = 10\ \mathrm{W^{-1}km^{-1}}$, $\beta_2 = -0.5\ \mathrm{ps^2km^{-1}}$, and $P = 3$ W.

A more detailed discussion of the MI gain specifically in optical ring resonators will be provided in Chapter 7, where we will also address the generation of OFC initiated by MI.

Part I

Parametric amplification in two coupled waveguides

Chapter 3

Basic theory of dual-waveguide parametric amplification

The concept of parametric amplification in two coupled nonlinear waveguides has been discussed broadly in the context of nonlinear optical couplers [43, 44]. Recently, it has been proposed as a viable practical solution for optical communications, characterised by a flat gain profile, phase-matching in the normal dispersion regime—facilitated by coupling contributions—and a 0-dB noise figure in the PS operational mode [45, 46]. Preliminary results have also been reported in dual-core highly nonlinear fibres [47, 48]. Additionally, it has also been demonstrated that if the coupling is selected with appropriate spatial dependencies, it can dynamically compensate for the mismatch arising from pump attenuation [48, 49], thereby addressing a significant issue in integrated amplifiers where attenuation is on the order of 1 dB/m [50]. This coupled waveguides geometry can yield superior performance in terms of bandwidth and bandwidth-gain products under specific parameter selections, compared to both standard and tapered single waveguide silicon nitride parametric amplifiers [51].

In this chapter, we introduce the basic eqution governing the propagation of light in coupled waveguides, considering a frequency-dependent coupling between two waveguides, specifically the coupling dispersion—the second derivative of the coupling strength with respect to frequency evaluated at the pump frequency. Then we derive the linear propagation equations for sidebands and provide the formalism of sinal and idler gain for certain cases. A sketch of the dual-waveguide parametric amplifier is illustrated in Fig. 3.1.

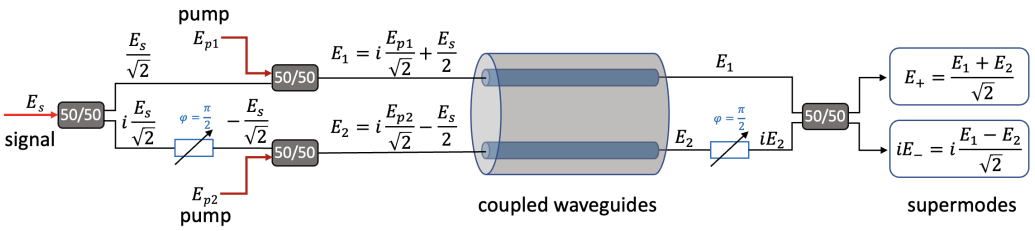

Figure 3.1: Sketch of a dual-waveguide parametric amplifier. A_s is the input signal wave and $A_{p1,p2}$ are the pump waves in the two waveguides respectively. The components denoted by "50/50" are 50/50 couplers. Blue rectangles with a diagonal arrow describe phase shifters, and one can input "+" and "−" supermodes by switching the phase shifter located before the coupled waveguides between $\pm\frac{\pi}{2}$. The second phase shifter and the coupler located after the coupled waveguides enable separation of the amplified supermodes at the output.

3.1 Coupled nonlinear Schrödinger equations

The starting point of our theory consists of the two CNLSEs which rule the propagation of the electric field amplitudes $E^{(1,2)}$ along two identical coupled waveguides:

$$\partial_z E^{(1,2)} = -\frac{\alpha}{2}E^{(1,2)} + i\sum_{n=0}^{\infty}\frac{\beta_n}{n!}(i\partial_t)^n E^{(1,2)} + i\gamma|E^{(1,2)}|^2E^{(1,2)} + i\sum_{n=0}^{\infty}\frac{C_n}{n!}(i\partial_t)^n E^{(2,1)}. \quad (3.1)$$

β_n and C_n are the n-th coefficient of the Taylor expansion of the frequency dependent propagation constant $\beta(\omega)$ and evanescent coupling $C(\omega)$ at pump frequency ω_0 respectively; while γ and α are the nonlinearity and attenuation coefficients; t is the temporal coordinate and z is the spatial evolution coordinate along the longitudinal waveguides dimension. Here, we have utilised the field amplitude E in place of the envelope A and lab time frame instead of retarded time, to maintain a symmetric form between β and C.

3.2 Stationary solutions

Equations (3.1) admit three types of (attenuated) CW solutions, which guide us in designing the pattern of input pump waves:

- Symmetric solution:

$$E_p^{(1,2)}(z) = \sqrt{\frac{P_t}{2}}e^{-\frac{\alpha}{2}z}e^{i[(\beta_0+C_0)z+\gamma\frac{P_t}{2}z_{\text{eff}}+\phi_0]}. \quad (3.2)$$

- Antisymmetric solution:

$$E_p^{(1,2)}(z) = \sqrt{\frac{P_t}{2}} e^{-\frac{\alpha}{2}z} e^{i[(\beta_0 - C_0)z + \gamma\frac{P_t}{2}z_{\text{eff}} + \phi_0 \pm \frac{\pi}{2}]}. \tag{3.3}$$

- Asymmetric solution:

$$E_p^{(1,2)}(z) = \sqrt{P^{(1,2)}} e^{-\frac{\alpha}{2}z} e^{i[\beta_0 z + \gamma P_t z_{\text{eff}} + \phi_0 \pm \frac{1-\text{sgn}(C_0)}{4}\pi]}, \tag{3.4}$$

  with $P^{(1)}P^{(2)}\gamma^2 e^{-2\alpha z} = C_0^2$, which may only holds if $\alpha = 0$ or if coupling is z-dependent.

Here, $P^{(1,2)}$ are the initial powers in two waveguides, $P_t = P^{(1)} + P^{(2)}$ is the total power, $z_{\text{eff}} = \int_0^z e^{-\alpha z'} dz' = (1 - e^{-\alpha z}/\alpha)$ (in absence of losses $z_{\text{eff}} \to z$), ϕ_0 is an arbitrary phase, and $\text{sgn}(C_0)$ represents the sign of C_0.

3.3 Linear evolution equations for sidebands

To study the parametric amplification, we explicitly separate the wave amplitudes $E^{(1,2)}$ into pump waves and sidebands as follows:

$$E^{(1,2)}(z,t) = E_p^{(1,2)}(z) + \epsilon^{(1,2)}(z,t). \tag{3.5}$$

Substituting Eq. (3.5) into Eq. (3.1) and considering the small sideband approximation $\left|\epsilon^{(1,2)}(z,t)\right|^2 \ll P^{(1,2)}$, we obtain the two linearly coupled equations governing the evolution of $\epsilon^{(1,2)}$,

$$\begin{aligned}\partial_z \epsilon^{(1,2)}(z,t) = &-\frac{\alpha}{2}\epsilon^{(1,2)}(z,t) + i\sum_{n=0}^{\infty}\frac{\beta_n}{n!}(i\partial_t)^n \epsilon^{(1,2)}(z,t) \\ &+ i\gamma 2\left|E_p^{(1,2)}\right|^2 \epsilon^{(1,2)}(z,t) + i\gamma\left[E_p^{(1,2)}\right]^2 \epsilon^{*(1,2)}(z,t) + i\sum_{n=0}^{\infty}\frac{C_n}{n!}(i\partial_t)^n \epsilon^{(2,1)}(z,t).\end{aligned} \tag{3.6}$$

If we introduce the supermodes defined by $E^{(\pm)} = [E^{(1)} \pm E^{(2)}]/\sqrt{2} = \left[E_p^{(1)} \pm E_p^{(2)}\right]/\sqrt{2} + \epsilon^{(\pm)}$, where $\epsilon^{(\pm)} = \left[\epsilon^{(1)} \pm \epsilon^{(2)}\right]/\sqrt{2}$ is the sidebands of the supermodes, then Eq. (3.6) can

be rewritten with supermodes as

$$\begin{aligned}\partial_z\epsilon^{(\pm)}(z,t) =& -\frac{\alpha}{2}\epsilon^{(\pm)}(z,t) + i\sum_{n=0}^{\infty}\frac{\beta_n \pm C_n}{n!}(i\partial_t)^n\epsilon^{(\pm)}(z,t)\\ &+ i\gamma\left[\left|E_p^{(1)}\right|^2 + \left|E_p^{(2)}\right|^2\right]\epsilon^{(\pm)}(z,t) + i\gamma\frac{\left[E_p^{(1)}\right]^2 + \left[E_p^{(2)}\right]^2}{2}\epsilon^{*(\pm)}(z,t)\\ &+ i\gamma\left[\left|E_p^{(1)}\right|^2 - \left|E_p^{(2)}\right|^2\right]\epsilon^{(\mp)}(z,t) + i\gamma\frac{\left[E_p^{(1)}\right]^2 - \left[E_p^{(2)}\right]^2}{2}\epsilon^{*(\mp)}(z,t). \qquad (3.7)\end{aligned}$$

Since all the three types of pump waves in two waveguides mentioned above are in phase or out of phase, Eq. (3.7) can be written in a compact form if we defnie $P_d = P^{(1)} - P^{(2)}$ and denote the phase of $E_p^{(1)}$ by $\phi^{(1)}(z)$, i.e., $E_p^{(1)} = \sqrt{\frac{P_t+P_d}{2}}e^{-\frac{\alpha}{2}z}e^{i\phi_p^{(1)}(z)}$, then Eq. (3.7) becomes

$$\begin{aligned}\partial_z\epsilon^{(\pm)}(z,t) =& -\frac{\alpha}{2}\epsilon^{(\pm)}(z,t) + i\sum_{n=0}^{\infty}\frac{\beta_n \pm C_n}{n!}(i\partial_t)^n\epsilon^{(\pm)}(z,t)\\ &+ i\gamma P_t e^{-\alpha z}\epsilon^{(\pm)}(z,t) + i\gamma\frac{P_t}{2}e^{-\alpha z}e^{i2\phi_p^{(1)}(z)}\epsilon^{*(\pm)}(z,t)\\ &+ i\gamma P_d e^{-\alpha z}\epsilon^{(\mp)}(z,t) + i\gamma\frac{P_d}{2}e^{-\alpha z}e^{i2\phi_p^{(1)}(z)}\epsilon^{*(\mp)}(z,t), \qquad (3.8)\end{aligned}$$

whose Fourier counterpart reads

$$\begin{aligned}\partial_z\hat{\epsilon}^{(\pm)}(z,\Omega) =& -\frac{\alpha}{2}\hat{\epsilon}^{(\pm)}(z,\Omega) + i\sum_{n=0}^{\infty}\frac{\beta_n \pm C_n}{n!}(-\Omega)^n\hat{\epsilon}^{(\pm)}(z,\Omega)\\ &+ i\gamma P_t e^{-\alpha z}\hat{\epsilon}^{(\pm)}(z,\Omega) + i\gamma\frac{P_t}{2}e^{-\alpha z}e^{i2\phi_p^{(1)}(z)}\hat{\epsilon}^{*(\pm)}(z,-\Omega)\\ &+ i\gamma P_d e^{-\alpha z}\hat{\epsilon}^{(\mp)}(z,\Omega) + i\gamma\frac{P_d}{2}e^{-\alpha z}e^{i2\phi_p^{(1)}(z)}\hat{\epsilon}^{*(\mp)}(z,-\Omega). \qquad (3.9)\end{aligned}$$

Eq. (3.8) [or Eq. (3.9)] governs the propagation of sidebands. In the chapters 4, 5 and 6, we will discuss various kinds of pump waves based on this equation.

3.4 Parametric gain

Compared with the single-waveguide case, the definition of parametric amplification gain is slightly different in the coupled waveguides, since there are two outputs and two inputs. We consider two kinds of input signals: blue-detuned "−" signal (corresponds to $\hat{\epsilon}^{(-)}(0,\Omega) \neq 0$

and $\hat{\epsilon}^{(+)}(0,\Omega)=0$, with $\Omega>0$) and blue-detuned "+" signal (corresponds to $\hat{\epsilon}^{(+)}(0,\Omega)\neq 0$ and $\hat{\epsilon}^{(-)}(0,\Omega)=0$ with $\Omega>0$). On the output side, it is possible to obtain "+" and "−" signals depending on the style of pump. The signal gain (corresponding to OPA) and idler gain (corresponding to WLC) in such cases are defined as follows:

- blue-detuned "−" signal input:

$$G^{(\pm)}(z,\Omega)=\begin{cases}\frac{|\hat{\epsilon}^{(\pm)}(z,\Omega)|^2}{|\hat{\epsilon}^{(-)}(0,\Omega)|^2} & \text{OPA}\\ \frac{|\hat{\epsilon}^{(\pm)}(z,-\Omega)|^2}{|\hat{\epsilon}^{(-)}(0,\Omega)|^2} & \text{WLC}\end{cases}. \tag{3.10}$$

- blue-detuned "+" signal input:

$$G^{(\pm)}(z,\Omega)=\begin{cases}\frac{|\hat{\epsilon}^{(\pm)}(z,\Omega)|^2}{|\hat{\epsilon}^{(+)}(0,\Omega)|^2} & \text{OPA}\\ \frac{|\hat{\epsilon}^{(\pm)}(z,-\Omega)|^2}{|\hat{\epsilon}^{(+)}(0,\Omega)|^2} & \text{WLC}\end{cases}. \tag{3.11}$$

In this thesis, we focus on blue-detuned signal amplification. However, the red-detuned case can be directly generalised by switching the sign of Ω. Both cases can be further divided into PI and PS regimes, relying on the existence of idler. In the PI case, there is no idler at input, i.e, $\hat{\epsilon}^{(\pm)}(0,-\Omega)=0$. In the PS case, idler is injected together with signal, which can be implemented in numerous scenarios [45, 46]. For illustrative purposes, we limit to an in-phase idler, which will be the case in chapters 4 and 6, that is $\hat{\epsilon}^{(\pm)}(0,-\Omega)=\hat{\epsilon}^{(\pm)}(0,\Omega)$.

3.5 Why two cores?

A flat gain profile is crucial for broadband OPA, as it ensures uniform amplification across a wide spectral range without introducing spectral distortion. Traditional single-core fibres often exhibit strong gain variation due to phase-matching limitations and nonlinear walk-off, as examplified in Fig. 2.1 in Chapter 2. To address this, dual-core fibre designs have been proposed, which allows flat gain profile through careful engineering of the coupling between cores [44, 45, 46]. Such structures enable broadband and flattened gain spectra, making them well-suited for applications requiring high-fidelity amplification over wide wavelength bands.

If we focus on the sidebands of "−" supermode in the symmetrically pumped dual-core fibre, ignore the losses and coupling dispersion, consider the expansion of β only up to the

second order, and define $\hat{\eta}^{(-)}(z,\Omega) = \hat{\epsilon}^{(-)} e^{-i\left(\beta_0 z + \gamma \frac{P_t}{2} z + \phi_0 - \beta_1 \Omega\right)}$, we find

$$\partial_z \begin{pmatrix} \hat{\eta}^{(-)}(z,\Omega) \\ \hat{\eta}^{*(-)}(z,-\Omega) \end{pmatrix} = \begin{pmatrix} i\frac{\beta_2}{2}\Omega^2 - i2C + i\gamma\frac{P_t}{2} & i\gamma\frac{P_t}{2} \\ -i\gamma\frac{P_t}{2} & -i\frac{\beta_2}{2}\Omega^2 + i2C - i\gamma\frac{P_t}{2} \end{pmatrix} \begin{pmatrix} \hat{\eta}^{(-)}(z,\Omega) \\ \hat{\eta}^{*(-)}(z,-\Omega) \end{pmatrix}. \tag{3.12}$$

Thus the modulation instability gain for the "−" supermodes reads

$$g_{\mathrm{dB}}^{(-)}(\Omega) = \frac{20}{\ln 10} \mathrm{Re}\left[\frac{1}{2}\sqrt{-(4C - \beta_2\Omega^2)(4C - 2\gamma P_t - \beta_2\Omega^2)}\right]. \tag{3.13}$$

It can be observed from the terms under the square root in Eq. (3.13) that the gain at $\Omega = 0$ appears when $C < \gamma P_t/2$, which has been discussed in detail in Ref. [52, 44], where $2C/\gamma$ is the critical power at which the symmetric CW solutions become unstable and a pitchfork bifurcation of the CW solutions takes place, giving rise to two stable asymmetric solutions. $C = \gamma P_t/4 \equiv C_c$ is another critical point: for coupling above this value, light launched in one core undergoes complete power transfer to the opposite core with a power-dependent spatial period, whereas for coupling below this value, the coupling is inhibited and the optical field remains essentially confined in the initially excited core. It can also be observed from Eq. (3.13) that the maximum gain appears at $\Omega = 0$ if $C \geq C_c$ in the anomalous dispersion regime, whereas in the normal dispersion regime, the maximum gain appears at $\Omega = 0$ if $C \leq C_c$. $C = C_c$ is the point to achieve a flat gain profile around $\Omega = 0$ [44].

In Fig. 3.2(a) and (c), we illustrate the impact of coupling strength on the MI gain in the anomalous and normal dispersion regimes, respectively. When the coupling strength reaches the critical coupling $C = C_c$ (indicated by the dashed line), we observe that the gain becomes flat in both regimes, which is clearer by observing Fig. 3.2(b) and (d) – the OPA gain with $C = C_c$ for propagation distance $L = 0.1$ km. Parameters used are the same as those in the single-core OPA shown in Fig. 2.1. Therefore, employing two coupled waveguides for OPA can improve the uniformity of the gain profile across a broad bandwidth.

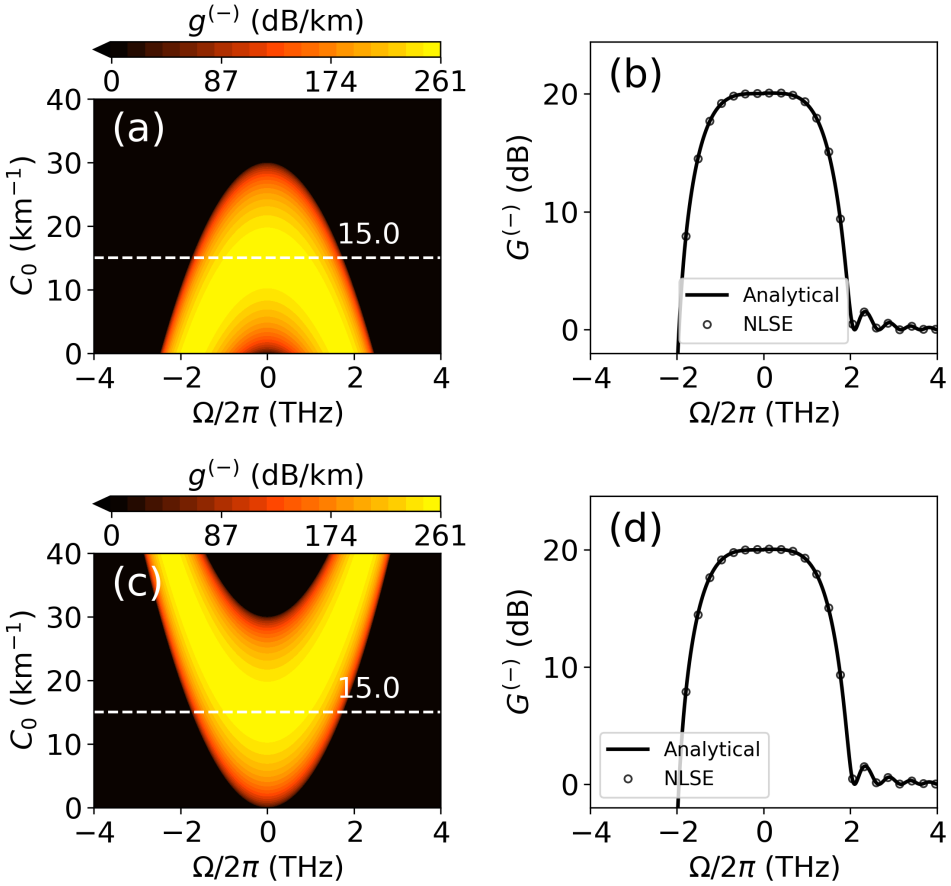

Figure 3.2: (a) and (c) Impact of the coupling strength on the MI gain in anomalous (a) and normal dispersion (c) regime. The coupling $C = C_c$ is indicated by a dashed line. (b) and (d) Flat gain profiles in dual-core OPA in anomalous (b) and normal (d) dispersion regimes. Parameters used are $\gamma = 10$ W^{-1}km^{-1}, $\beta_2 = \mp 0.5$ ps^{2}km^{-1}, $P_t = 6$ W (3 W per waveguide), $L = 0.1$ km, and $C = 15$ km^{-1}.

Chapter 4

The role of coupling dispersion

The work presented in this chapter has been adapted from the following publications:
[1] M. Shi, V. Ribeiro, and A. M. Perego. Parametric amplification in coupled nonlinear waveguides: the role of coupling dispersion. *Front. Photon.*, 4:1051294, 2023.

4.1 Introduction

In Chapter 3, we demonstrated how the coupling strength and coupling dispersion enters into the CNLSEs and mathematically compensate for the individual waveguide dispersion. Also, in Section 3.5, we show how the coupling strength help achieving the a flat gain profile. This chapter is dedicated to a detailed presentation of the impact of coupling dispersion on the gain spectrum of the dual waveguide parametric amplifier.

Indeed, the influence of the frequency dependence of the coupling strength has been investigated previously, particularly in the context of coupled silicon waveguides. In this setting, it facilitates the existence of solitons and MI under conditions where these phenomena would be unattainable within a single, uncoupled waveguide [53, 54, 55]. However, the role of coupling dispersion in parametric amplification has not yet been examined analytically. The impact of the MI spectrum associated with the first coefficient in the Taylor expansion of the coupling around the pump frequency has been theoretically studied in the past for two evanescently coupled core fibres [56, 57] and in generalised forms of the two coupled NLSEs [58, 59, 60, 61]. It has been demonstrated that this term can induce the generation of additional spectral sidebands in both normal and anomalous dispersion regimes,

provided that the pump power distribution is asymmetric between the two waveguides.

In this chapter, we present a different phenomenon; specifically, we show that the second-order term in the expansion can enable complete compensation of the GVD of the individual waveguide when the pump power distribution is symmetric between the two waveguides. We provide analytical formulas for the parametric gain in both the PS and PI regimes, considering characteristic parameters for lossless coupled core fibre and lossy integrated silicon nitride waveguide amplifiers. This offers a novel approach for dispersion engineering, which can be employed in the design of broadband, flat gain, low noise figure, and energy-efficient parametric amplifiers.

4.2 Symmetrically pumped evolution equation for sidebands

To illustrate the role of coupling dispersion, we focus on the symmetric pumped parametric amplification, and show how it enables flat gain profile for one of the system supermode. In this case, we have $\phi_p^{(1)}(z) = (\beta_0 + C_0)z + \gamma\frac{P_t}{2}z_{\text{eff}} + \phi_0$ and $P_d = 0$, then Eq. (3.9) can be simplified as

$$\begin{aligned}\partial_z\hat{\epsilon}^{(\pm)}(z,\Omega) = &-\frac{\alpha}{2}\hat{\epsilon}^{(\pm)}(z,\Omega) + i\sum_{n=0}^{\infty}\frac{\beta_n \pm C_n}{n!}(-\Omega)^n\hat{\epsilon}^{(\pm)}(z,\Omega)\\ &+ i\gamma P_t e^{-\alpha z}\hat{\epsilon}^{(\pm)}(z,\Omega) + i\gamma\frac{P_t}{2}e^{-\alpha z}e^{i2\phi_p^{(1)}(z)}\hat{\epsilon}^{*(\pm)}(z,-\Omega).\end{aligned} \tag{4.1}$$

By introducing $\hat{\eta}^{(\pm)}$ defined as $\hat{\epsilon}^{(\pm)}(z,\Omega) = \hat{\eta}^{(\pm)}(z,\Omega)e^{i\left[\phi_p^{(1)}(z)+\beta_{\text{odd}}(\Omega)z\right]}$, with $\beta_{\text{odd}}(\Omega) = -\sum_{k=0}^{\infty}\frac{\beta_{2k+1}}{(2k+1)!}\Omega^{2k+1}$, Eq. (4.1) and its complex conjugate can be written in matrix form as

$$\begin{aligned}&\partial_z\begin{pmatrix}\hat{\eta}^{(\pm)}(z,\Omega)\\ \hat{\eta}^{*(\pm)}(z,-\Omega)\end{pmatrix} = M_{\pm}\begin{pmatrix}\hat{\eta}^{(\pm)}(z,\Omega)\\ \hat{\eta}^{*(\pm)}(z,-\Omega)\end{pmatrix}\\ &= \begin{pmatrix}-\frac{\alpha}{2} + iK_{\pm}(z,\Omega) \pm iC_{\text{odd}}(\Omega) & i\gamma\frac{P_t}{2}e^{-\alpha z}\\ -i\gamma\frac{P_t}{2}e^{-\alpha z} & -\frac{\alpha}{2} - iK_{\pm}(z,\Omega) \pm iC_{\text{odd}}(\Omega)\end{pmatrix}\begin{pmatrix}\hat{\eta}^{(\pm)}(z,\Omega)\\ \hat{\eta}^{*(\pm)}(z,-\Omega)\end{pmatrix},\end{aligned} \tag{4.2}$$

where $K_{\pm}(z,\Omega) = \beta_{\text{even}}(\Omega) \pm C_{\text{even}}(\Omega) \pm C_0 - C_0 + \gamma\frac{P_t}{2}e^{-\alpha z}$, with $\beta_{\text{even}}(\Omega) = \sum_{k=1}^{\infty}\frac{\beta_{2k}}{(2k)!}\Omega^{2k}$, $C_{\text{even}}(\Omega) = \sum_{k=1}^{\infty}\frac{C_{2k}}{(2k)!}\Omega^{2k}$, $C_{\text{odd}}(\Omega) = -\sum_{k=0}^{\infty}\frac{C_{2k+1}}{(2k+1)!}\Omega^{2k+1}$. Note that β_0 and C_0 are excluded in the definition of β_{even} and C_{even}, respectively. Eq. (4.2) admits an exact solution in the lossless case and an approximate one in the lossy scenario. The solution is formally

$[\hat{\eta}^{(\pm)}(z,\Omega),\hat{\eta}^{*(\pm)}(z,-\Omega)]^T = e^{\int_0^z M_\pm(z')dz'}[\hat{\eta}^{(\pm)}(0,\Omega),\hat{\eta}^{*(\pm)}(0,-\Omega)]^T$, where the exponential expressions read

$$\begin{aligned} e^{\int_0^z M_\pm(z')dz'} &= e^{\pm iC_{\text{odd}}z}e^{-\frac{\alpha}{2}z}N^\pm \\ &= e^{\pm iC_{\text{odd}}z}e^{-\frac{\alpha}{2}z}\begin{pmatrix} \cosh(\rho_\pm)+i\theta_\pm\frac{\sinh(\rho_\pm)}{\rho_\pm} & i\gamma\frac{P_t}{2}L_{\text{eff}}\frac{\sinh(\rho_\pm)}{\rho_\pm} \\ -i\gamma\frac{P_t}{2}L_{\text{eff}}\frac{\sinh(\rho_\pm)}{\rho_\pm} & \cosh(\rho_\pm)-i\theta_\pm\frac{\sinh(\rho_\pm)}{\rho_\pm} \end{pmatrix} \end{aligned} \tag{4.3}$$

with $\theta_\pm = \gamma\frac{P_t}{2}L_{\text{eff}} + \frac{\beta_{\text{even}}\pm C_{\text{even}}}{2}z - C_0 z \pm C_0 z$, $\rho_\pm = \sqrt{(\gamma\frac{P_t}{2}L_{\text{eff}})^2-\theta_\pm^2}$ and $L_{\text{eff}} = \frac{1-e^{-\alpha z}}{\alpha}$ (in the lossless case $L_{eff} = z$ should be used).

4.3 Results

To highlight the role of coupling dispersion in the parametric amplification process, we calculated analytically the gain of ouput signal "−" with respect to the blue-detuned "−" signal input. Referring to Eq. (3.10), we find

$$G(z,\Omega) = \begin{cases} \frac{|\hat{\eta}^{(-)}(z,\Omega)|^2}{|\hat{\eta}^{(-)}(0,\Omega)|^2} = e^{-\alpha z}\frac{|N_{11}^-\hat{\eta}^{(-)}(0,\Omega)+N_{12}^-\hat{\eta}^{*(-)}(0,-\Omega)|^2}{|\hat{\eta}^{(-)}(0,\Omega)|^2} & \text{OPA} \\ \frac{|\hat{\eta}^{(-)}(z,-\Omega)|^2}{|\hat{\eta}^{(-)}(0,\Omega)|^2} = e^{-\alpha z}\frac{|N_{21}^-\hat{\eta}^{(-)}(0,\Omega)+N_{22}^-\hat{\eta}^{*(-)}(0,-\Omega)|^2}{|\hat{\eta}^{(-)}(0,\Omega)|^2} & \text{WLC} \end{cases}, \tag{4.4}$$

where N_{mn}^-, with $m,n = 1,2$, are elements of the matrix N^- defined in Eq. (4.3). Then, we contrasted these theoretical predictions with numerical simulations of the NLSEs [Eqs. (3.1)], which were carried out using the split-step Fourier method (see Appendix B). Although our theoretical framework applies to an arbitrary order of waveguide and coupling dispersion, we have limited our analysis in the following examples to expansions up to the second order. Furthermore, it is noteworthy that the odd terms in the coupling Taylor expansion, represented by C_{odd}, do not contribute to the gain expression associated with the supermodes $\epsilon^{(\pm)}$.

Firstly, we focus on the PI regime, selecting the initial conditions $\hat{\epsilon}^{(2)}(0,\Omega) = -\hat{\epsilon}^{(1)}(0,\Omega) \neq 0$ and $\hat{\epsilon}^{(1)}(0,-\Omega) = \hat{\epsilon}^{(2)}(0,-\Omega) = 0$, which correspond to the excitation of the "−" supermode only. This configuration provides the best performance in terms of noise figure [46], a flat gain profile for identical pump power and phase in the two waveguides, and the compensation of second-order GVD by the second-order coupling dispersion parameter, as will

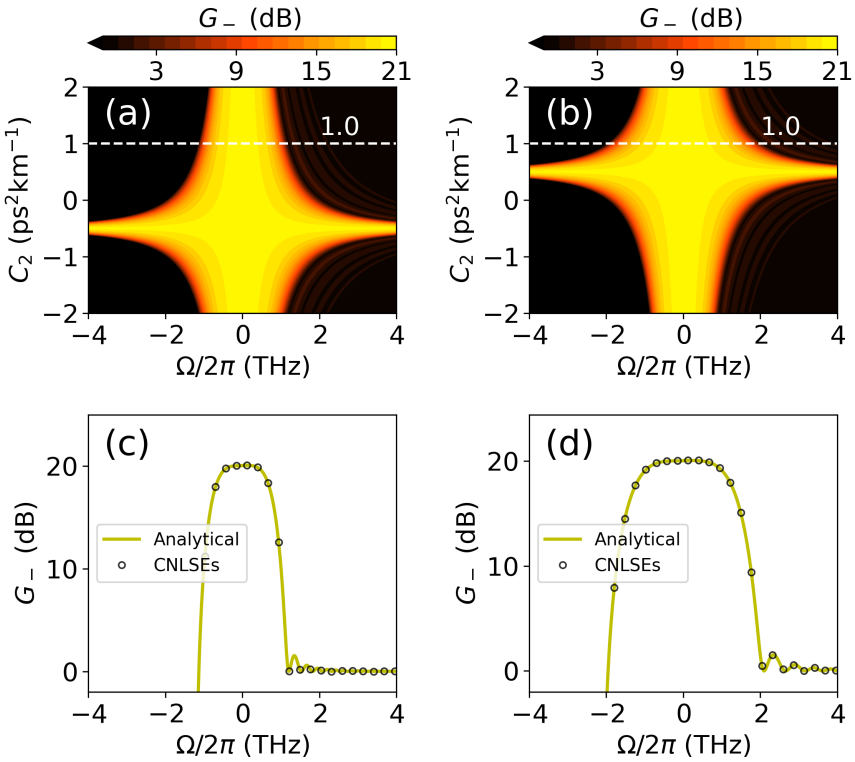

Figure 4.1: Lossless PI amplifier. Map of parametric analytical gain vs frequency and C_2 in anomalous a) and normal b) dispersion regime; and gain spectrum vs frequency comparison between numerics and theory for anomalous c) and normal d) dispersion regime with $C_2 = 1$ ps^{2}km^{-1}. Other parameters used are $\beta_2 = \pm 0.5$ ps^{2}km^{-1}, $\gamma = 10$ W^{-1}km^{-1}, $P_t = 6$ W, $C_0 = 15$ km^{-1} and $z = 0.1$ km.

be further demonstrated in this chapter. Therefore, the gain is given by

$$G_{\mathrm{PI}}(z) = \begin{cases} e^{-\alpha z}|N_{11}^{-}|^2 = e^{-\alpha z}\left(1+S^2\right) & \text{OPA} \\ e^{-\alpha z}|N_{21}^{-}|^2 = e^{-\alpha z}S^2 & \text{WLC} \end{cases}, \tag{4.5}$$

where $S = \gamma \frac{P_t}{2} L_{\mathrm{eff}} \frac{\sinh(\rho_-)}{\rho_-}$.

The C_2 dependent gain for lossless (utilising parameters typical of coupled core fibres) and lossy (employing parameters typical of silicon nitride waveguides) parametric amplifiers is illustrated in Fig. 4.1 (a) and (b) as well as in Fig. 4.2 (a) and (b), respectively, while considering both anomalous and normal dispersion waveguides. The parameters have been selected to satisfy the flat gain requirement, $C_0 = C_c$. The agreement between theoretical predictions and simulations is remarkable, as evidenced by the examples presented in Fig. 4.1 (c) and (d) alongside Fig. 4.2 (c) and (d). It is noteworthy that coupling dispersion, when

appropriately chosen, can effectively compensate for the dispersion of individual waveguides, thereby significantly improve the amplifier's gain bandwidth. The maximum bandwidth is attained when $C_2 = \beta_2$, as clearly illustrated in Fig. 4.1 (a) and (b), as well as in Fig. 4.2 (a) and (b).

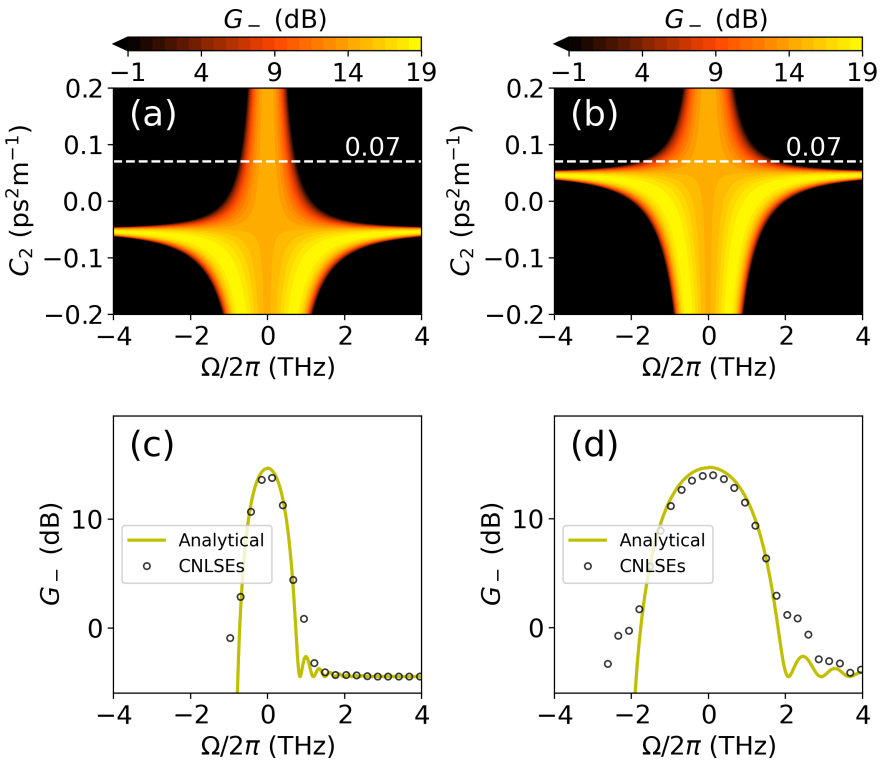

Figure 4.2: Lossy PI amplifier. Map of parametric analytical gain vs frequency and C_2 in anomalous a) and normal b) dispersion regime; and gain spectrum vs frequency comparison between numerics and theory for anomalous c) and normal d) dispersion regime with $C_2 = 0.07$ ps^{2}m^{-1}. Other parameters used are $\beta_2 = \pm 0.05$ ps^{2}m^{-1}, $\gamma = 1.2$ W^{-1}m^{-1}, $P_t = 6$ W, $C_0 = 1.8$ m^{-1}, $z = 1.5$ m and $\alpha = 0.69$ m^{-1} corresponding to 3 dBm^{-1}.

In the PS regime, given $\hat{\epsilon}^{(1)}(0,\Omega)$, we establish the initial conditions as follows: $\hat{\epsilon}^{(1)}(0,-\Omega) = \hat{\epsilon}^{(1)}(0,\Omega)$, $\hat{\epsilon}^{(2)}(0,\Omega) = \hat{\epsilon}^{(2)}(0,-\Omega) = -\hat{\epsilon}^{(1)}(0,\Omega)$. This leads to the relations $\hat{\epsilon}^{(-)}(0,\Omega) = \sqrt{2}\hat{\epsilon}^{(1)}(0,\Omega)$ and $\hat{\epsilon}^{(-)}(0,-\Omega) = \sqrt{2}\hat{\epsilon}^{(1)}(0,\Omega)$. Assuming the phase difference between the signal and pump is ϕ_s, the analytical expression for the gain is given by

$$G_{\mathrm{PS}}(z) \begin{cases} e^{-\alpha z}|N_{11}^{-}e^{i\phi_s} + N_{12}^{-}e^{-i\phi_s}|^2 & \text{OPA} \\ e^{-\alpha z}|N_{21}^{-}e^{i\phi_s} + N_{22}^{-}e^{-i\phi_s}|^2 & \text{WLC} \end{cases}. \tag{4.6}$$

The dependency of the gain on the phase ϕ_s is illustrated in Fig. 4.3 (a) and (b) for the lossy amplifier. We then fixed ϕ_s to maximise the gain and calculated the gain spectrum

both analytically and numerically, as shown in Fig. 4.3 (c) and (d), where the PI gain is also shown for reference. An excellent agreement between theory and simulations is observed in this case as well. It is noteworthy that in this work, we have considered $\epsilon^{(-)}(z,t)$ as the output of the amplifier. If $\epsilon^{(+)}(z,t)$ is selected instead, analogous dispersion compensation effects will occur, but with C_2 having the opposite sign.

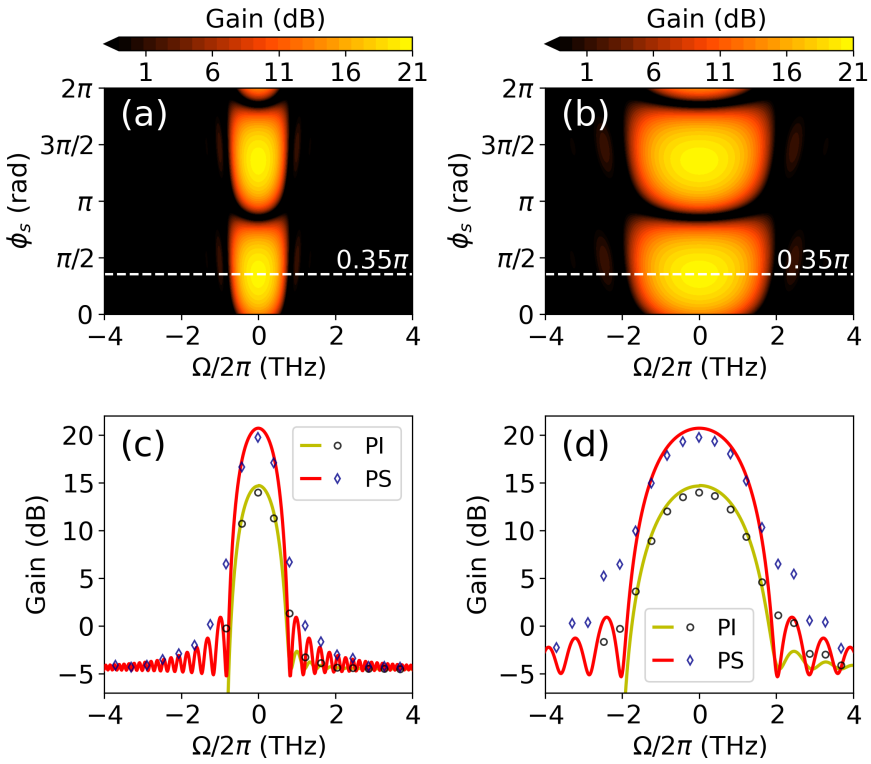

Figure 4.3: Lossy PS amplifier. Map of parametric gain calculated analytically vs frequency and ϕ_s in anomalous a) and normal b) dispersion regime; gain spectrum vs frequency for anomalous c) and normal d) dispersion regime with $\phi_s = 0.35\pi$ comparing numerics with analytics. Other parameters used are $\beta_2 = \pm 0.05$ ps^{2}m^{-1}, $\gamma = 1.2$ W^{-1}m^{-1}, $P_t = 6$ W, $C_0 = 1.8$ m^{-1}, $z = 1.5$ m, $C_2 = 0.07$ ps^{2}m^{-1} and $\alpha = 0.69$ m^{-1} corresponding to 3 dBm^{-1}.

4.4 Conclusions

In conclusion, we have demonstrated that coupling dispersion is a fundamental physical effect that facilitates dispersion engineering in dual-waveguide parametric amplifiers. This effect allows for significant tailoring of the gain spectrum and provides the potential for broadband parametric amplification, even when the individual waveguides exhibit normal dispersion. This powerful tool enhances the versatility of dual-waveguide parametric amplifiers, which are already characterised by features such as a flat gain spectrum, a 0-dB noise

figure, and compensation of losses induced by mismatches. Future research on frequency-dependent coupling for dispersion compensation could be pertinent for fibre amplifiers with numerous cores and for arrays of integrated waveguides with varying coupling topologies, as well as for other photonic devices that involve multiple coupled modes. We remark that, although coupling dispersion is a well-defined theoretical parameter, its controlled manipulation over kilometre-scale lengths in two-core fibres is challenging in practice, since the coupling coefficient is mainly fixed by fabrication constraints such as core separation, refractive-index contrast, and drawing tension. In contrast, integrated coupled-waveguide platforms provide much greater freedom for dispersion engineering: the waveguide separation, cross-sectional geometry, and cladding environment can be lithographically tailored, enabling precise control of both the magnitude and frequency dependence of the coupling. From an experimental perspective, coupling dispersion is therefore expected to be more accessible and tunable in chip-based coupled waveguides than in long multi-core fibres, even though the formal theory presented here applies to both systems. A second remark concerns the relative importance of coupling dispersion compared to other nonlinear processes that are always present in fibres, most notably the delayed Raman response. In standard single-core fibres, Raman-induced nonlinear phase shifts can substantially alter the phase-matching relation and the MI gain spectrum, and a comprehensive study of this interplay has been carried out in the context of birefringent fibres in Ref. [15]. To the best of our knowledge, no analogous systematic investigation exists for two-core fibres. The present work therefore isolates the effect of coupling dispersion within an instantaneous Kerr model; whether coupling dispersion dominates over Raman-induced contributions in real fibre platforms will depend on the specific material parameters and operating regime. A complete quantitative comparison is beyond the scope of this thesis but represents an interesting direction for future studies.

Chapter 5

Impact of pump power and phase fluctuations on the dual-waveguide parametric amplification

---

The work presented in this chapter has been adapted from the following publications:
[2] M. Shi, V. Ribeiro, and A. M. Perego. On the resilience of dual-waveguide parametric amplifiers to pump power and phase fluctuations. *Appl. Phys. Lett.*, 122(10):101102, 2023.

5.1 Introduction

Several impairments may impact the performance of dual-waveguide parametric amplification, such as relative power and phase variations between the pump waves in the two waveguides, random fluctuations of the zero-dispersion wavelength and their correlation across the two waveguides, as well as differences in parameters among the two waveguides—such as GVD and nonlinearity—resulting from the fabrication process [26, 62, 63, 7]. In this study, we focus on the symmetrically and antisymmetrically pumped waveguides, analytically and numerically examine the first of these potential impairments, specifically the impact of pump power and phase fluctuations between the two coupled waveguides on amplifier performance when the two waveguides are pumped with equal power. We derive an analytical formula that characterises the spatial instability—leading to power exchange and oscillations of the CW solutions between the two coupled waveguides during propagation—that

results from the minor and unwanted time-independent perturbations caused by varying input power and phase. We demonstrate that the predictions from our analytical formula correspond well with numerical solutions regarding the propagation of pump waves along the waveguides. Furthermore, we conduct a numerical investigation into the influence of input pump phase and power differences on the amplifier gain, utilising parameters typical of coupled-core silica fibres, as well as integrated silicon nitride waveguides, and show that the amplifier exhibits robustness against fluctuations within realistic experimental control limits.

5.2 Stability of Pump waves — formalism

We first study how the initial input power imbalance and phase difference impact on the propagation of pump waves in two waveguides. Our starting point is the two stationary solutions Eq. (3.2) and Eq. (3.3), which can be rewritten in a compact form as

$$\bar{E}_p^{(1,2)} = \sqrt{\frac{P_t}{2}} e^{-\frac{\alpha}{2}z} e^{i(\phi_p \pm \xi\frac{\pi}{2})}, \tag{5.1a}$$

$$\phi_p = \phi_0 + [\beta_0 + (-1)^{\xi} C_0]z + \frac{\gamma}{2} P_t z_{\text{eff}}, \tag{5.1b}$$

where ξ is 0 for symmetric solutions and 1 for antisymmetric solutions, and $\phi_0 \pm \xi\frac{\pi}{2}$ represent the initial phases of the two pump waves. Then we add small perturbations $\eta_{1,2}$ ($|\eta_{1,2}|^2 \ll P_t$) at pump frequency to the CW solutions $\bar{E}_p^{(1,2)}$, which leads to the following *ansatz*:

$$E_p^{(1,2)}(z) = \bar{E}_p^{(1,2)} + \eta_{1,2}(z) e^{-\frac{\alpha}{2}z} e^{i(\phi_p \pm \xi\frac{\pi}{2})}. \tag{5.2}$$

By redefining P_t as the total power and choosing an appropriate ϕ_0, the initial amplitudes in the two waveguides can always be expressed as

$$E_p^{(1,2)}(0) = \sqrt{\frac{P_t}{2} \pm \frac{P_d}{2}} e^{i(\phi_0 \pm i\frac{\phi_d}{2} \pm \xi\frac{\pi}{2})}, \tag{5.3}$$

where P_d and ϕ_d represent the initial power difference and phase difference, respectively. Assuming $P_d \ll P_t$ and $\phi_d \ll 1$, the amplitudes can be reformulated as

$$\begin{aligned} E_p^{(1,2)}(0) &\approx \left(\sqrt{\frac{P_t}{2}} \pm \frac{P_d}{2\sqrt{2P_t}}\right)\left(1 \pm \frac{\phi_d}{2}\right) e^{i(\phi_0 \pm \xi\frac{\pi}{2})} \\ &\approx \left(\sqrt{\frac{P_t}{2}} \pm \frac{P_d}{2\sqrt{2P_t}} \pm i\frac{1}{2}\sqrt{\frac{P_t}{2}}\phi_d\right) e^{i(\phi_0 \pm \xi\frac{\pi}{2})}. \end{aligned} \tag{5.4}$$

It implies that $\eta_1(0) = -\eta_2(0) = \frac{P_d}{2\sqrt{2P_t}} + i\frac{1}{2}\sqrt{\frac{P_t}{2}}\phi_d$. By substituting Eqs. (5.2) into the coupled NLSEs [Eq. (3.1)], and explicitly expressing $\eta_\pm = a_\pm + ib_\pm$, where $\eta_\pm = \eta_1 \pm \eta_2$, we derive the equations governing the propagation of the real and imaginary parts of the perturbations as follows,

$$\begin{aligned} \partial_z \begin{pmatrix} a_\pm \\ b_\pm \end{pmatrix} =& M_\pm \begin{pmatrix} a_\pm \\ b_\pm \end{pmatrix} \\ =& \begin{pmatrix} 0 & \gamma\frac{P_t}{2}e^{-\alpha z} - K_\pm \\ \gamma\frac{P_t}{2}e^{-\alpha z} + K_\pm & 0 \end{pmatrix} \begin{pmatrix} a_\pm \\ b_\pm \end{pmatrix} \end{aligned} \tag{5.5}$$

where $K_\pm = \gamma\frac{P_t}{2}e^{-\alpha z} + (-1)^\xi(\pm C_0 - C_0)$. As $\eta_+(0) \approx 0$ and $\eta_-(0) \approx \frac{P_d}{\sqrt{2P_t}} + i\sqrt{\frac{P_t}{2}}\phi_d$, the evolution only needs to be calculated for η_-, while η_+ remains negligible. An approximate solution to Eq. (5.5) is given by $(a_-, b_-)^{\mathrm{T}} = e^{\int_0^z M_-(z')dz'}(a_-(0), b_-(0))^{\mathrm{T}}$, where the exponential expression is defined as

$$N = e^{\int_0^z M_-(z')dz'} = \begin{pmatrix} \cosh\rho & \theta\sinh\rho \\ \theta^{-1}\sinh\rho & \cosh\rho \end{pmatrix}, \tag{5.6}$$

with $\rho = \sqrt{-2C_0 z[2C_0 z - (-1)^\xi \gamma P_t z_{\mathrm{eff}}]}$, $\theta = (-1)^\xi 2C_0 z/\rho$. Thus we obtain

$$\begin{aligned} \eta_-(z) =& (\cosh\rho + i\theta^{-1}\sinh\rho)\frac{P_d}{\sqrt{2P_t}} \\ &+ (\theta\sinh\rho + i\cosh\rho)\sqrt{\frac{P_t}{2}}\phi_d. \end{aligned} \tag{5.7}$$

To gain direct insight into the instability of the symmetric pump power solution, we examine the power difference between the two waveguides, defined as $P_-(z) = |u_{p1}|^2 - |u_{p2}|^2$. This

can be evaluated as a function of η_- approximately by

$$\begin{aligned} P_-(z) =& e^{-\alpha z}\left(\left|\sqrt{\frac{P_t}{2}}+\frac{\eta_-}{2}\right|^2-\left|\sqrt{\frac{P_t}{2}}-\frac{\eta_-}{2}\right|^2\right) \\ =& e^{-\alpha z}\left(P_d\cosh\rho+P_t\phi_d\theta\sinh\rho\right) \end{aligned} \tag{5.8}$$

where $\eta_1 = -\eta_2 = \eta_-/2$ is considered. We first focus on the symmetric pump power solution ($\xi = 0$). The characteristic flat broadband gain of coupled waveguide amplifiers is achieved with symmetric pump input when the attenuation is negligible for $\gamma P_t = 4C_0$. Consequently, we will employ this relation throughout the chapter, resulting in $\theta \approx 1$.

5.3 Resilience of parametric amplification: symmetric pump

In realistic symmetrically pumped parametric amplifiers, $\cosh\rho$ is approximately equal to $\sinh\rho$ when the amplifier length L exceeds the nonlinear length L_{NL}, specifically $L > L_{NL} = \frac{1}{\gamma P_t/2}$. For our analysis, we consider $L_{NL} \approx 33$ m for dual-core fibres and $L_{NL} \approx 28$ cm for integrated waveguides. Therefore, the two expressions enclosed by parentheses in Eq. (5.7) are approximately equal.

As the pump power typically exceeds 1 W, fluctuations of approximately 1 mW in power and 1 mRad in phase will yield similar dynamics for the power imbalance P_-. Experimentally, it is generally more challenging — though still feasible — to control phase differences to the mRad level compared to managing power fluctuations or imbalances to the mW level, as we will discuss in more detail later. Hence, we can typically assume that $\sqrt{\frac{P_t}{2}}\phi_d > \frac{P_d}{\sqrt{2P_t}}$, and the initial phase differences in the two waveguides usually represent the dominant effect that can induce substantial pump power imbalance during propagation. In typical experimental setups for optical parametric amplifiers, the noise generated by the pump laser can result in power fluctuations, yielding an optical signal-to-noise ratio (OSNR) ranging from 50 to 70 dB. For a pump laser with an average power of 1 W, this translates to noise power or variance within the sub-μW to μW range. Another source of power fluctuations is the 3-dB coupler that follows the pump laser, which typically consists of a low-power laser source coupled to an erbium-doped fibre amplifier. However, since the two optical waves employed to pump dual-waveguide parametric amplifiers are generally derived from splitting a powerful wave via a 50/50 optical coupler, coupler imperfections primarily con-

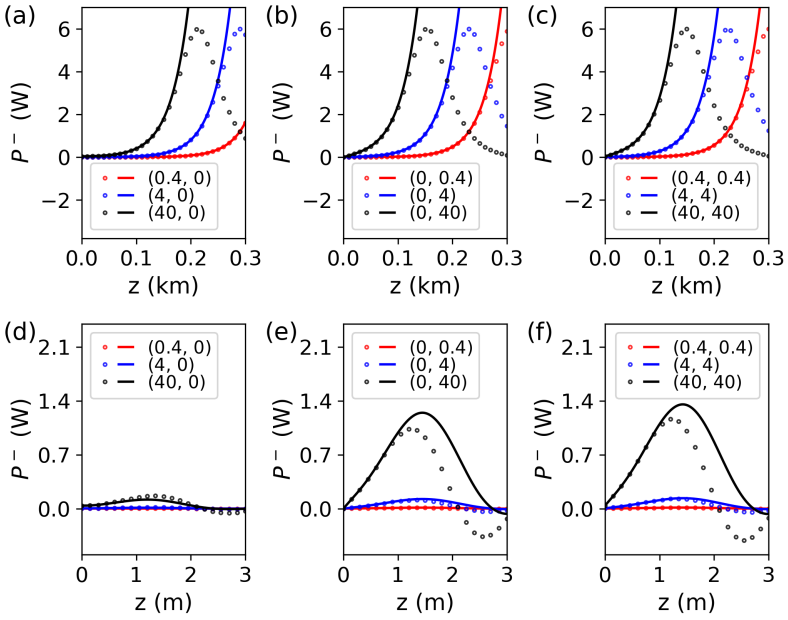

Figure 5.1: Evolution of pump power difference for the symmetric case. P_- evolution without losses calculated analytically (solid) and in numerical simulations (dots) for different values of P_d and ϕ_d shown in the legends, where (x, y) represents $P_d = x$ mW and $\phi_d = y$ mRad. (a)-(c) describe coupled core fibres and parameters used are $\gamma = 10$ W^{-1}km^{-1}, $P_t = 6$ W, $C_0 = 15$ km^{-1} and $\alpha = 0$. (d)-(f) describe lossy integrated waveguides and parameters used are $\gamma = 1.2$ W^{-1}m^{-1}, $P_t = 6$ W, $C_0 = 1.8$ m^{-1} and $\alpha = 0.69$ m^{-1} corresponding to 3 dB $\cdot$ m^{-1}.

tribute to the relative power differences between the two pump waves. The ratio tolerance is approximately ±5% within a 100 nm bandwidth for most standard 50/50 couplers, increasing almost monotonically as the wavelength shifts away from the centre wavelength (in practice, the ratio tolerance is significantly smaller when the pump is positioned at the centre of the coupler's transmission bandwidth). For a reference pump power of about 1 W, this results in a maximum power imbalance of ±50 mW between the pumps, equating to a net difference of 100 mW. It is important to note that the physical power difference between the pumps corresponds to P_d in our notation (as defined in Eqs. (5.3)). Sources of relative phase differences between the two input pump waves are related to variations in their optical paths—after being split at the 50/50 coupler. These variations may arise from alignment issues in the fibre components within the setup or from fabrication precision challenges in the case of integrated waveguides. For instance, an optical path difference of 1 nm corresponds to approximately 6 mRad of phase difference at a wavelength of 1550 nm in silica. The methods available for significantly reducing relative input pump power imbalance and for precisely controlling phase differences will be discussed later in the text.

Examples of the evolution of pump power differences with and without losses (using parameters typical of coupled core fibres and silicon nitride waveguides, respectively) are illustrated in Fig. 5.1. To investigate the worst-case scenario, where pump and phase fluctuations lead to a maximum power difference between the two waveguides, the signs of P_d and ϕ_d are maintained consistently in the following analysis. For each scenario, we assessed the effects of various initial pump power differences — $P_d = 0.4$ mW, 4 mW, 40 mW — as well as the effects of different initial phase differences — $\phi_d = 0.6$ mRad, 6 mRad, 60 mRad (which correspond to optical path differences of approximately ~ 0.1 nm, 1 nm, and 10 nm at a wavelength of $\lambda = 1550$ nm in silica) — and the combined effects of both initial power and phase differences. In the lossless case (Fig. 5.1(a)-(c), the analytical theory aligns closely with the numerical simulation results of the coupled NLSEs, particularly up to the point where most of the power resides in a single waveguide ($P_- \approx P_t$). Notably, larger input perturbations result in P_- becoming significant earlier along the propagation. It is important to note that the simulation results reveal the power exchange between the two waveguides during propagation: power in one waveguide transfers to the other and subsequently returns at the critical point $P_- = P_t$, at which all power is confined to a single waveguide. Since the stability analysis relies on the assumption of small perturbations, this phenomenon is not captured by the analytical calculations. In the lossy case (Fig. 5.1(d)-(f), we observe that P_- exhibits damped oscillations, and the agreement between simulations and theory appears to be quite robust for the parameters considered.

To investigate how the amplifier gain spectrum is affected by the relative input pump phase and power fluctuations, we performed numerical simulations of Eqs. (3.1) using parameters corresponding to both coupled core fibres and integrated lossy coupled waveguide amplifiers, taking into account terms up to the second order in waveguide and coupling dispersion. The simulated amplifiers had characteristics analogous to those used in the perturbation analysis shown in Fig. 5.1, resulting in the key quantity that determines the amplifier gain—the nonlinear phase shift accumulated per waveguide, given by $\gamma P_t L/2$—reaching values of up to 4.5 for dual-core fibres and up to 5.4 for integrated waveguides. These values can be considered realistic for parametric amplifiers employed in optical communications, where the accumulated nonlinear phase shift typically ranges between 3 and 5[64, 65, 30].

We calculated the PI gain spectrum with a blue-detuned "−" signal input. We first examined how the relative pump power and phase difference individually influence the

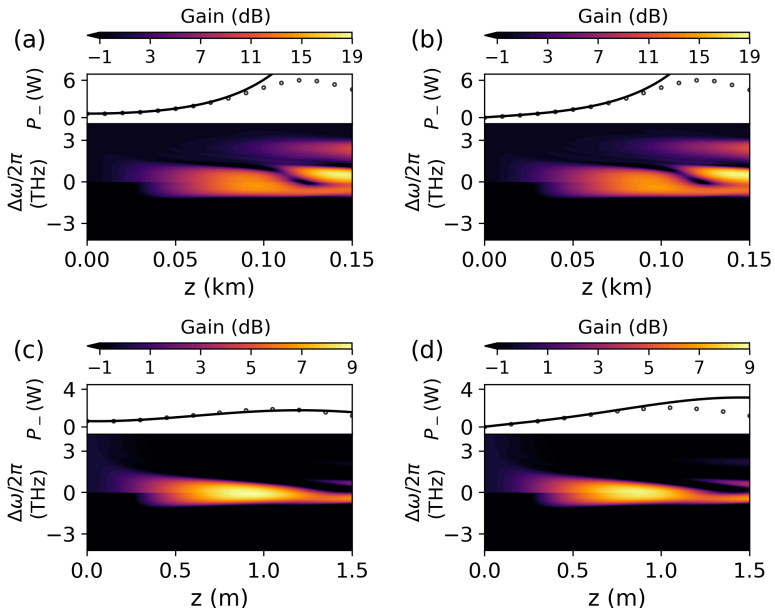

Figure 5.2: PI gain for E_-: equivalence of amplitude and phase fluctuations effects. Map of parametric gain from numerical simulations vs z and frequency. Amplification in lossless coupled core fibres: (a) (P_d = 600 mW, $\phi_d = 0$); (b) ($P_d = 0$,ϕ_d = 100 mRad). Amplification in lossy coupled waveguides: (c) (P_d = 600 mW, $\phi_d = 0$); (d) ($P_d = 0$, ϕ_d = 100 mRad). Evolution of P_- calculated analytically (solid) and numerically (dots) are shown as a reference. Other parameters used in (a)-(b) are: $\beta_2 = -0.5$ ps^{2}km^{-1}, $\gamma = 10$ W^{-1}km^{-1}, $P_t = 6$ W, $\alpha = 0$ km^{-1}, $C_0 = 15$ km^{-1}, $C_1 = -3$ ps $\cdot$ km^{-1} and $C_2 = 1$ ps^{2}km^{-1}; parameters used in (c)-(d) are: $\beta_2 = -0.05$ ps^{2}m^{-1}, $\gamma = 1.2$ W^{-1}m^{-1}, $P_t = 6$ W, $C_0 = 1.8$ m^{-1}, $C_1 = -0.3$ ps$\cdot$m^{-1}, $C_2 = 0.1$ ps^{2}m^{-1} and $\alpha = 0.69$ m^{-1} corresponding to 3 dB $\cdot$ m^{-1}.

amplifier gain spectrum. Specifically, we compared the parametric gain spectrum obtained with parameters of (P_d = 600 mW, $\phi_d = 0$) and ($P_d = 0$, ϕ_d = 100 mRad). From Eq. (5.7), it follows that η_- would remain nearly identical in both scenarios, given the selected total pump power $P_t = 6$ W. The findings are summarised in Fig. 5.2, which includes results for both coupled core fibres and coupled integrated lossy waveguides.

We have then investigated the effect of varying pump power and pump phase fluctuations on the parametric gain, comparing the resulting parametric gain profiles with those observed in the unperturbed scenario. The gain of the sidebands for the lossless dual-core fibre amplifier is illustrated in Fig. 5.3 for supermode E_- and in Fig. 5.4 for supermode E_+. In the case of the lossy integrated waveguide amplifier, the gain is presented in Fig. 5.5 for supermode E_- and in Fig. 5.6 for supermode E_+, respectively. Up to $P_d = 40$ mW and ϕ_d = 40 mRad, we observe that for propagation distances of $z \lesssim 100$ m and $z \lesssim 1$ m for coupled core fibres and integrated waveguides, respectively, the primary effect of amplitude and phase perturbations is a slight reduction in maximum gain, without substantially affecting

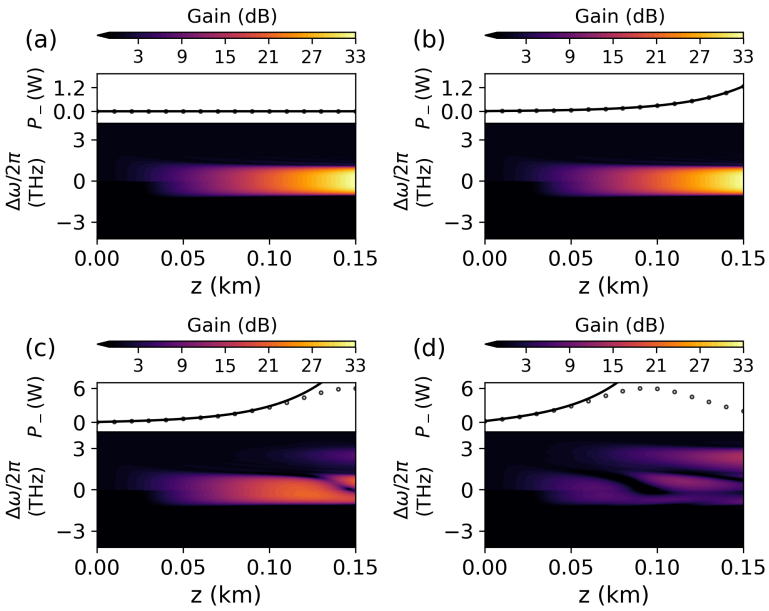

Figure 5.3: Symmetrically pumped lossless PI gain for E_{-}. Maps of parametric gain from numerical simulations vs z and frequency. (a) no fluctuations ($P_d = 0$, $\phi_d = 0$); (b) $P_d = 4$ mW and $\phi_d = 4$ mRad; (c) $P_d = 40$ mW and $\phi_d = 40$ mRad; (d) $P_d = 200$ mW and $\phi_d = 200$ mRad. Evolution of P_{-} calculated analytically (solid) and numerically (dots) are shown as a reference. Remaining parameters used are the same as in Fig. 5.2(a)-(b).

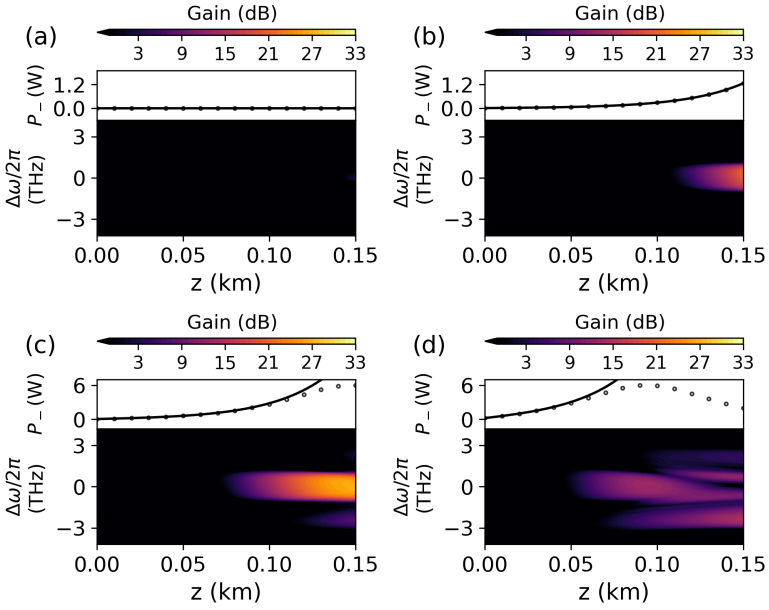

Figure 5.4: Symmetrically pumped lossless PI gain for E_{+}. Map of parametric gain from numerical simulations vs z and frequency. (a) no fluctuations ($P_d = 0$, $\phi_d = 0$); (b) $P_d = 4$ mW and $\phi_d = 4$ mRad; (c) $P_d = 40$ mW and $\phi_d = 40$ mRad; (d) $P_d = 200$ mW and $\phi_d = 200$ mRad. Evolution of P_{-} calculated analytically (solid) and numerically (dots) are shown as a reference. Remaining parameters used are the same as in Fig. 5.2(a)-(b).

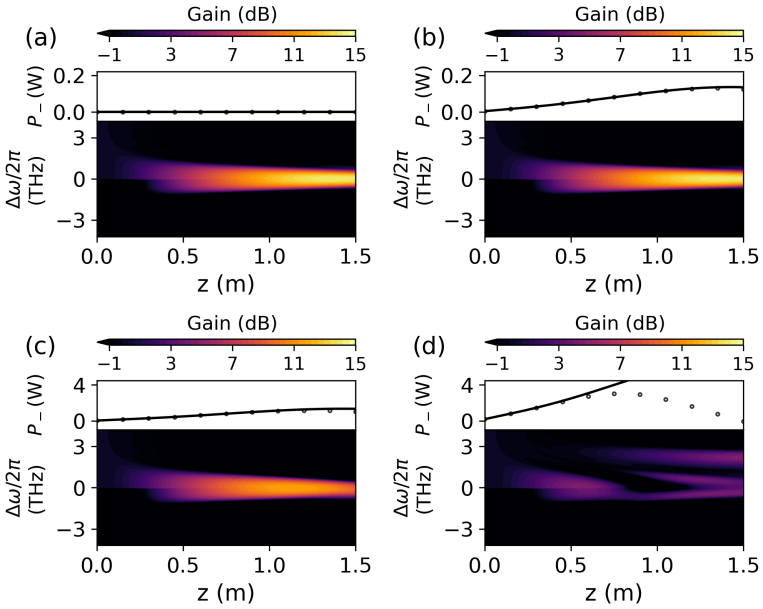

Figure 5.5: Symmetrically pumped lossy PI gain for E_{-}. Maps of parametric gain calculated numerically vs z and frequency. (a) no fluctuations ($P_d = 0$, $\phi_d = 0$); (b) $P_d = 4$ mW and $\phi_d = 4$ mRad; (c) $P_d = 40$ mW and $\phi_d = 40$ mRad; (d) $P_d = 200$ mW and $\phi_d = 200$ mRad. Evolution of P_{-} calculated analytically (solid) and numerically (dots) are shown as a reference. Remaining parameters used are the same as in Fig. 5.2(c)-(d).

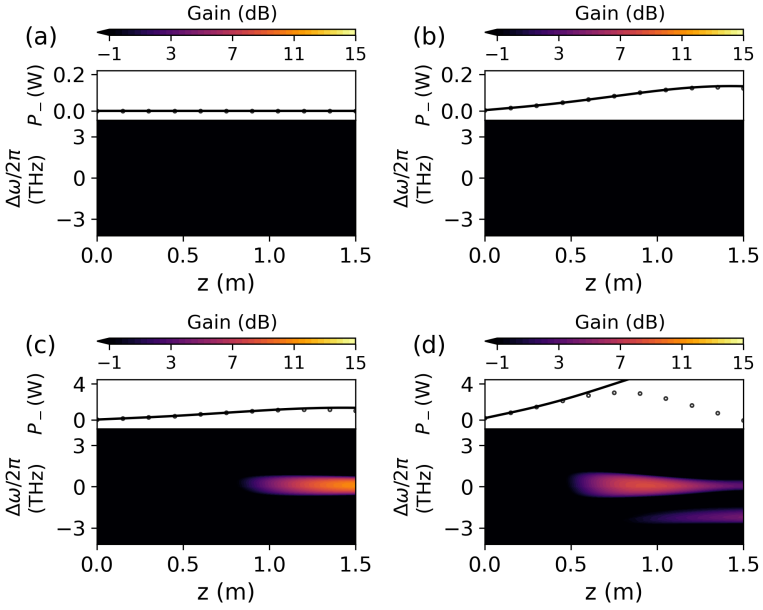

Figure 5.6: Symmetrically pumped lossy PI gain for E_{+}. Map of parametric gain with numerical simulation vs z and frequency. (a) no fluctuations ($P_d = 0$, $\phi_d = 0$); (b) $P_d = 4$ mW and $\phi_d = 4$ mRad; (c) $P_d = 40$ mW and $\phi_d = 40$ mRad; (d) $P_d = 200$ mW and $\phi_d = 200$ mRad. Evolution of P_{-} calculated analytically (solid) and numerically (dots) are shown as a reference. Remaining parameters used are the same as in Fig. 5.2(c)-(d).

the ideal amplifier performance. However, for larger propagation distances and/or for higher values of input power and phase differences (here we consider $P_d = 200$ mW and $\phi_d = 200$ mRad to illustrate a more extreme case), significant modifications of the gain spectrum occur, as well as energy coupling from the input supermode E_- to supermode E_+. This also results in a frequency asymmetric gain spectrum for different supermodes, due to the interplay between power asymmetry in the two waveguides and C_1, the first-order term of the coupling Taylor expansion around the pump frequency. It can indeed be shown that the combination of coupling dispersion and asymmetric pump power among the two waveguides can lead to intermodal four-wave mixing, resulting in coupling between different supermodes and a frequency asymmetric parametric gain spectrum for the individual supermodes as well [3]. We note that significant changes in the gain spectrum begin to occur when most of the pump power is confined to a single waveguide ($P_- \approx P_t$), as illustrated by the evolution of P_- plotted in each case considered.

5.4 Resilience of parametric amplification: antisymmetric pump

In the antisymmetrically pumped ($\xi = 1$) parametric amplifier, the evolution of the pump power difference remains governed by Eq. (5.8), yet ρ remains imaginary at any distance, causing the pump power difference P_- to oscillate around zero. This behaviour is illustrated in Fig. 5.7. In the antisymmetric scenario, the same initial conditions for signals and idlers as in the symmetric case have been considered, resulting in more stable parametric amplification—although without a flat gain profile—as depicted in Figs. 5.8 and 5.9. Here, we observe that spectral gain degradation occurs for much larger perturbation values compared to the symmetric case. Analogously to the symmetric case, substantial changes in the gain spectrum for mode E_- correspond to energy transfer to mode E_+ (not shown here). We have presented the effects of input pump phase and power fluctuations in the PI operational regime. Notably, in the PS scenario, we observe analogous results, which we do not discuss here for brevity. A similar situation arises for a PI amplifier where the input signals are located in supermode E_+ rather than in E_-.

Achieving two nearly identical optical paths for the waves injected into the coupled nonlinear waveguides amplifier may lead to alignment issues that necessitate specialised

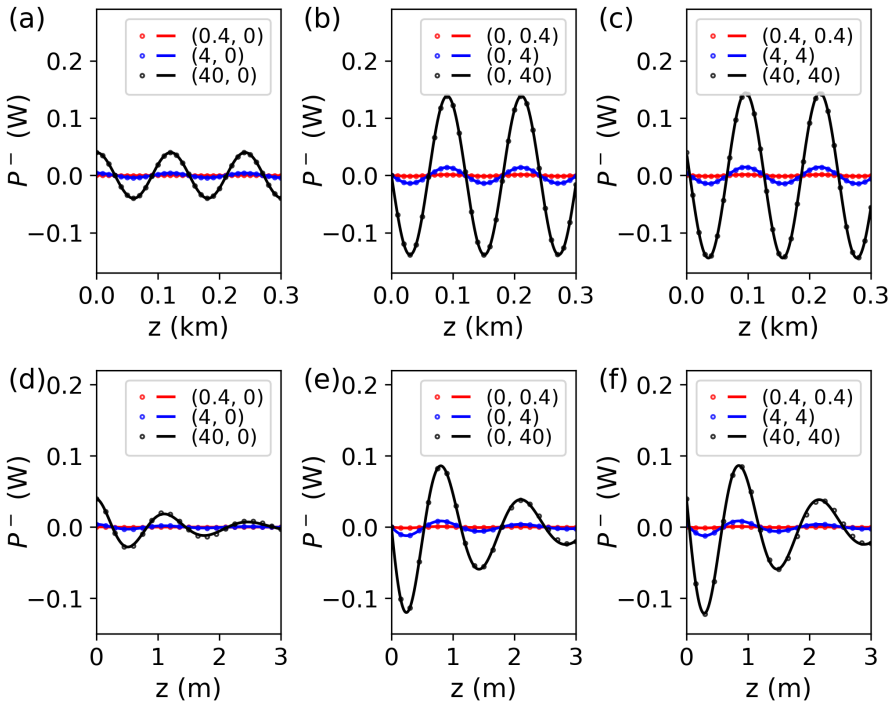

Figure 5.7: Evolution of pump power difference for the antisymmetric case. (a)-(c) Evolution of P_{-} without losses calculated analytically (solid) and in numerical simulations (dots) for different values of P_d and ϕ_d shown in the legends, where (x, y) represents $P_d = x$ mW and $\phi_d = y$ mRad. Parameters used are like Fig. 5.1(a). (d)-(f) Evolution of P_{-} with losses calculated analytically (solid) and in numerical simulations (dots). Parameters used are like Fig. 5.1(d).

equipment for precise compensation. However, existing commercial phase metres [66] allow for phase control on the order of 6 μrad. This indicates that our parameter choices concerning the gain spectrum degradation due to large relative phase differences, as illustrated in the previous figures, constitute a rather pessimistic scenario. A similar pessimistic scenario has indeed been considered for gain degradation due to significant input power differences as well. An analysis based on currently available 50/50 couplers [67], which have a coupling ratio tolerance of $\pm 5\%$, predicts relative differences on the order of ± 50 mW for a 1 W pump in the worst-case scenario. However, it is crucial to emphasise that since the resolution of typical power metres is on the order of sub μW, such imbalances can be corrected, as they are not fundamental, without the need for sophisticated technology; for instance, by utilising variable optical attenuators in each output port of the 50/50 couplers. Therefore, it is likely feasible to achieve the performance depicted in Fig. 5.3, 5.5(a)-(b) with minimal engineering effort and negligible impact on the noise figure.

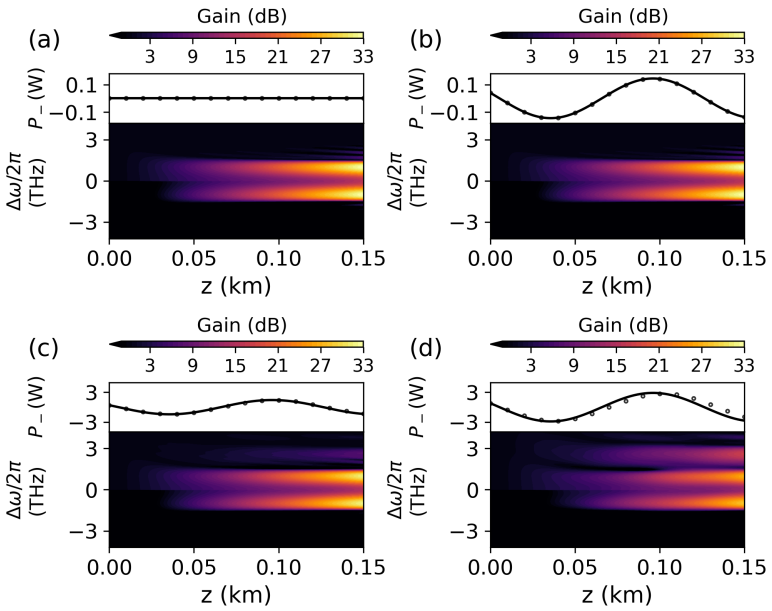

Figure 5.8: Antisymmetrically pumped lossless PI gain for E_{-}. Maps of parametric gain from numerical simulations vs z and frequency. (a) no fluctuations ($P_d = 0$, $\phi_d = 0$); (b) $P_d = 40$ mW and $\phi_d = 40$ mRad; (c) $P_d = 400$ mW and $\phi_d = 400$ mRad; (d) $P_d = 800$ mW and $\phi_d = 800$ mRad. Evolution of P_{-} calculated analytically (solid) and numerically (dots) are shown as a reference. Remaining parameters used are the same as in Fig. 5.2(a)-(b).

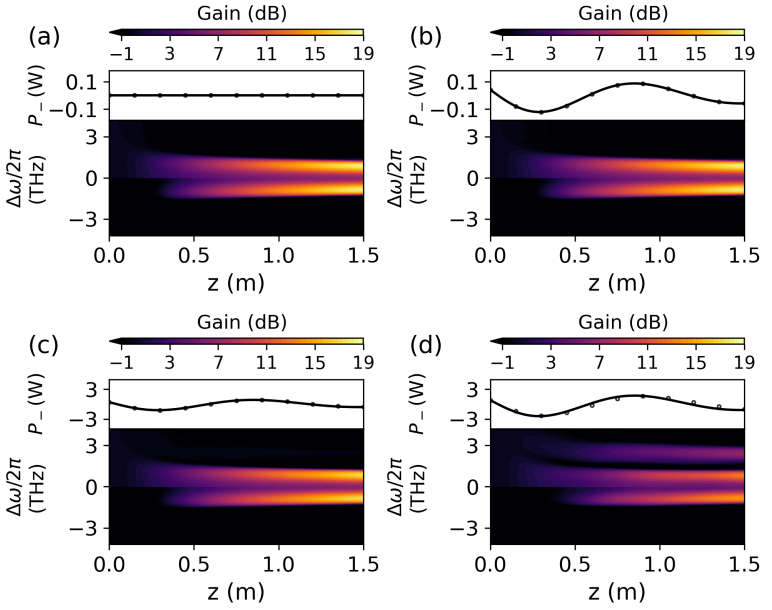

Figure 5.9: Antisymmetrically pumped lossy PI gain for E_{-}. Maps of parametric gain from numerical simulations vs z and frequency. (a) no fluctuations ($P_d = 0$, $\phi_d = 0$); (b) $P_d = 40$ mW and $\phi_d = 40$ mRad; (c) $P_d = 400$ mW and $\phi_d = 400$ mRad; (d) $P_d = 800$ mW and $\phi_d = 800$ mRad. Evolution of P_{-} calculated analytically (solid) and numerically (dots) are shown as a reference. Remaining parameters used are the same as in Fig. 5.2(c)-(d).

5.5 Conclusions

In conclusion, we have presented an analytical theory for the stability of pump waves in an equally pumped dual-waveguide parametric amplifier, considering the effects of relative input power and phase fluctuations. Our analysis predicts the evolution of the pump power difference along the waveguides and agrees well with numerical simulations for realistic parameters. Additionally, we have demonstrated numerically how the instability of pump waves, induced by power and phase fluctuations, affects the amplifier gain spectrum, even for perturbation magnitudes significantly larger than what can be feasibly controlled in experiments. The findings of this study suggest that equally pumped coupled dual-waveguide parametric amplifiers exhibit resilience against pump fluctuations, providing valuable insights for the design of photonic technologies that utilise this amplification scheme.

Chapter 6

Asymmetric parametric gain spectrum in dual-core fibre amplifiers through unbalanced pump waves

---

The work presented in this chapter has been adapted from the following publications:
[3] M. Shi, V. Ribeiro, and A. M. Perego. Parametric amplification based on intermodal four-wave mixing between different supermodes in coupled-core fibers. *Opt. Express*, 31(6): 9760–9768, 2023.

6.1 Introduction

In standard parametric amplification, the Manley–Rowe relations impose that signal and idler grow together, so the idler is inevitably generated and carried along the same spatial mode. In many platforms this is undesirable: the idler introduces an extra noise channel since it originates from vacuum fluctuations, and it occupies an additional spectral band that may interfere with system-level spectral allocation. These considerations motivate the search for regimes in which the signal can be efficiently amplified while the idler is strongly suppressed. The asymmetric gain spectrum in parametric amplifiers has been studied and attributed to factors such as third-order dispersion [68, 69, 70], gain saturation [71], Raman

gain [16, 64], and asymmetric losses between signal and idler waves [72, 73, 74]. While these effects introduce measurable asymmetries, they typically do not reduce the idler gain to a negligible level across a broad bandwidth. Recently, idler suppression has also been demonstrated using interferometric architectures designed to reject unwanted four-wave mixing products [75]. Multimode fibres offer an attractive alternative for amplifying signals while spatially isolating idler waves in distinct optical modes. This is achieved through intermodal four-wave mixing [20, 76, 77, 78, 79]. In this chapter, we demonstrate that coupled core fibres used as parametric amplifiers, when operated in the regime where the two cores are pumped with different powers—due to the frequency dependence of the coupling—can achieve frequency asymmetric gain for the two supermodes of the system. This leads to negligible amplification of idlers in the supermode carrying the signals, eliminating the need for spectral filtering or any form of optical losses, while relying solely on conservative nonlinear dynamics. In Fig. 6.1 the amplifier concept is illustrated pictorially.

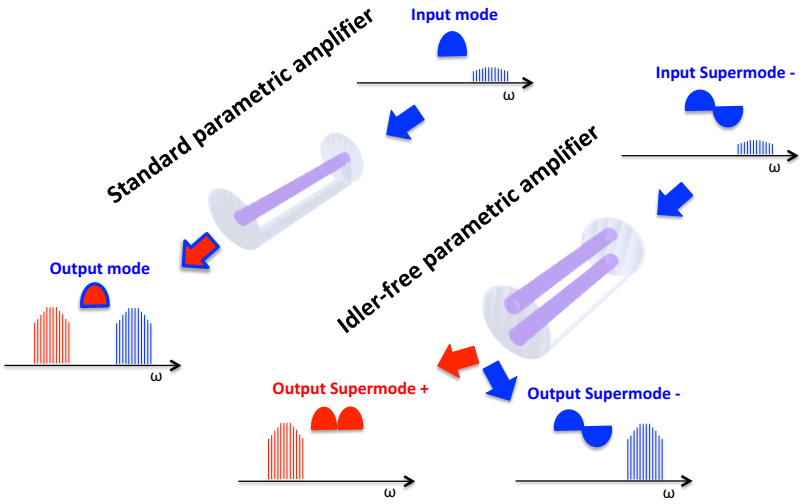

Figure 6.1: Amplifier concept. Schematic of the difference between the standard parametric amplifier, which amplifies signals and generates idlers in the same optical mode, and the asymmetrically pumped dual core fibre parametric amplifier, for which the signals encoded into one supermode are amplified and no idlers are generated in the same supermode.

6.2 Formalism

As discussed in Section 3.2, the coupled waveguides exhibit asymmetric CW solutions for fibres (loss is negligible) when the powers in the two waveguides are related by the equation $P^{(1)}P^{(2)}\gamma^2 e^{-2\alpha z} = C_0^2$. This condition can be equivalently expressed as $P_d =$

$\sqrt{P_t^2-(2C_0/\gamma)^2}$, which implies that the prerequisite $P_t > 2C_0/\gamma$ must be satisfied [80]. By setting $\alpha = 0$, Eq. (3.4) can be concisely rewritten as

$$E_p^{(1,2)}(z) = \sqrt{\frac{P_t+P_d}{2}}e^{i\phi_p^{(1)}(z)}, \quad \phi_p^{(1)}(z) = \phi_0 + \beta_0 z + \gamma P_t z, \tag{6.1}$$

and evolution equations for sidebands Eq. (3.9) becomes

$$\begin{aligned}\partial_z\hat{\epsilon}^{(\pm)}(z,\Omega) =& i\sum_{n=0}^{\infty}\frac{\beta_n \pm C_n}{n!}(-\Omega)^n\hat{\epsilon}^{(\pm)}(z,\Omega) \\ &+ i\gamma P_t\hat{\epsilon}^{(\pm)}(z,\Omega) + i\gamma\frac{P_t}{2}e^{i2\phi_p^{(1)}(z)}\hat{\epsilon}^{*(\pm)}(z,-\Omega) \\ &+ i\gamma P_d\hat{\epsilon}^{(\mp)}(z,\Omega) + i\gamma\frac{P_d}{2}e^{i2\phi_p^{(1)}(z)}\hat{\epsilon}^{*(\mp)}(z,-\Omega).\end{aligned} \tag{6.2}$$

Similar to the procedure done in Section 4.2, by introducing $\hat{\eta}^{(\pm)}$ defined as $\hat{\epsilon}^{(\pm)}(z,\Omega) = \hat{\eta}^{(\pm)}(z,\Omega)e^{i\left[\phi_p^{(1)}(z)+\beta_{\text{odd}}(\Omega)z\right]}$, with $\beta_{\text{odd}}(\Omega) = -\sum_{k=0}^{\infty}\frac{\beta_{2k+1}}{(2k+1)!}\Omega^{2k+1}$, Eq. (6.2) and its complex conjugate can be written in matrix form,

$$\partial_z\begin{pmatrix}\hat{\mathcal{E}}^+\\ \hat{\mathcal{E}}^-\end{pmatrix} = M\begin{pmatrix}\hat{\mathcal{E}}^+\\ \hat{\mathcal{E}}^-\end{pmatrix} = \begin{pmatrix}M_+ & M_c\\ M_c & M_-\end{pmatrix}\begin{pmatrix}\hat{\mathcal{E}}^+\\ \hat{\mathcal{E}}^-\end{pmatrix}. \tag{6.3}$$

Here we defined $\hat{\mathcal{E}}^{\pm}(z,\Omega) = [\hat{\eta}^{(\pm)}(z,\Omega), \hat{\eta}^{(\pm)}(z,-\Omega)]^T$. The matrix M governs the propagation of $\hat{\mathcal{E}}$. The submatrices $M_{\pm}$, which describes the evolution of $\hat{\mathcal{E}}^{\pm}$, and M_c representing the coupling between the modes $\hat{\mathcal{E}}^+$ and $\hat{\mathcal{E}}^-$ induced by pump power difference P_d, read

$$M_{\pm} = \begin{pmatrix}iK_{\pm} \pm iC_{\text{odd}} & i\gamma\frac{P_t}{2}\\ -i\gamma\frac{P_t}{2} & -iK_{\pm} \pm iC_{\text{odd}}\end{pmatrix}, \quad M_c = i\gamma\frac{P_d}{2}\begin{pmatrix}2 & 1\\ -1 & -2\end{pmatrix}, \tag{6.4}$$

respectively, where $K_{\pm}(z,\Omega) = \beta_{\text{even}}(\Omega) \pm C_{\text{even}}(\Omega) \pm C_0$, $\beta_{\text{even}}(\Omega) = \sum_{k=1}^{\infty}\frac{\beta_{2k}}{(2k)!}\Omega^{2k}$, $C_{\text{even}}(\Omega) = \sum_{k=1}^{\infty}\frac{C_{2k}}{(2k)!}\Omega^{2k}$, and $C_{\text{odd}}(\Omega) = -\sum_{k=0}^{\infty}\frac{C_{2k+1}}{(2k+1)!}\Omega^{2k+1}$. $\hat{\mathcal{E}}^{\pm}$ can be computed at an arbitrary propagation distance z as $(\hat{\mathcal{E}}_+(z), \hat{\mathcal{E}}_-(z))^T = N(\hat{\mathcal{E}}_+(0), \hat{\mathcal{E}}_-(0))^T$ with matrix $N = e^{Mz}$.

6.3 Asymmetric parametric amplification gain spectrum

We now examine the parametric gain of the "−" signal output with providing the blue-detuned "−" signal input. To better emphasise the essential conditions for idler-free para-

metric amplification, we first consider the case where $C_2 = 0$. We compared the analytical predictions with numerical simulations of the coupled NLSEs (Eqs. 3.1), which were performed using a split-step Fourier method. In the PI regime, the analytical expression for the gain is given by

$$G_{\mathrm{PI}}(z) = \begin{cases} |N_{33}(z)|^2 & \text{OPA} \\ |N_{43}(z)|^2 & \text{WLC} \end{cases} \tag{6.5}$$

where N_{mn} is the element of the matrix N at m-th row and n-th column. The matrix elements need to be calculated numerically due to their cumbersome form resulting from the matrix exponential e^{Mz}.

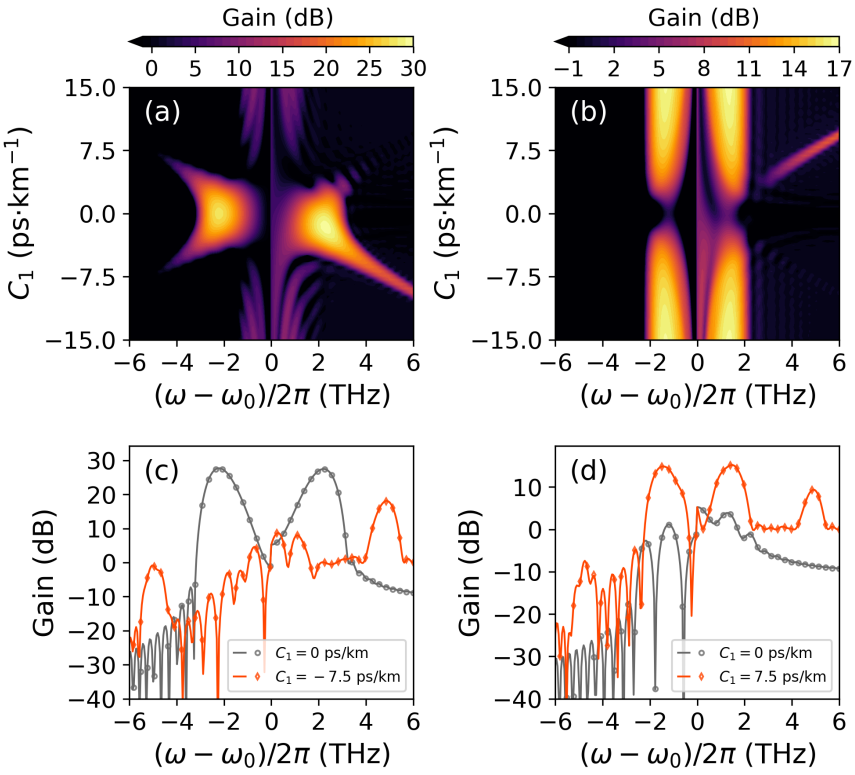

Figure 6.2: PI amplifier with "−" signal input. Map of analytical parametric gain for $E^{(-)}$ vs frequency and C_1 in anomalous (a) and normal (b) dispersion regime, and comparison of gain spectrum vs frequency between theory (continuous line) and numerics (dots) for anomalous (c) and normal (d) dispersion regime with $C_1 = \mp 7.5$ ps $\cdot$ km^{-1} ($C_1 = 0$) shown in orange (gray). Other parameters used are $\beta_2 = \mp 0.5$ ps^{2}km^{-1}, $\gamma = 10$ W^{-1}km^{-1}, $P_t = 5.4$ W, $C_0 = 15$ km^{-1}, $C_2 = 0$, and $z = 0.1$ km.

We illustrate the dependence of the amplifier gain spectrum on C_1 in Fig. 6.2 for (a) anomalous and (b) normal waveguide dispersion, respectively. Additionally, panels (c) and

(d) depict an idler-free operation example for the − supermode. In this latter case, the idler-free operational mode is restricted to the high-frequency range, resulting in a smaller signal gain for the parameters considered. For the selected parameters, the idler-free regime demonstrates a notable gain difference of approximately 20 dB between signal and idler sidebands in both anomalous and normal dispersion regimes. In the normal dispersion scenario, asymmetric gain coexists with symmetric low-frequency sidebands, which necessitate additional filtering to assess the useful signal power in the idler-free spectral lobe. For input signal waves within the interval $(0, \Omega_m]$, we computed the quantities $I_+ = \frac{\int_0^{+\Omega_m} S_-(\Omega')d\Omega'}{\int_{-\Omega_m}^{+\Omega_m} S_-(\Omega')d\Omega'}$ and $I_s = \frac{\int_{s_1}^{s_2} S_-(\Omega')d\Omega'}{\int_{-\Omega_m}^{+\Omega_m} S_-(\Omega')d\Omega'}$. I_+ represents the ratio of the integral of the output spectral power $S_-(\Omega')$ of the "−" supermode for frequencies exceeding the pump frequency to the total power contained in the simulation window $[-\Omega_m = -2\pi \cdot 6, +\Omega_m = 2\pi \cdot 6]$ rad/ps, excluding the pump. Meanwhile, I_s indicates the ratio of the integral of the "−" supermode output spectral power computed within the interval around the asymmetric signal spectral lobe, delineated by s_1 and s_2, to the total power in the full simulation window.

For the anomalous dispersion case — (Fig. 6.2(c) with $C_1 = -7.5$ ps $\cdot$ km^{-1}) — we find $I_+ = 0.96$ and $I_s = 0.79$, indicating that 96% of the power of the − supermode is present in the signal spectrum and that 79% of the power resides within the asymmetric spectral lobe in the interval $[s_1 = 2\pi \cdot 3.85, s_2 = 2\pi \cdot 5.61]$ rad/ps. Performance is less pronounced in the normal dispersion regime — (Fig. 6.2(d) with $C_1 = 7.5$ ps $\cdot$ km^{-1}) — due to the substantial power contained in the low-frequency symmetric sidebands. In this case, we obtain $I_+ = 0.58$ and $I_s = 0.09$, indicating that 58% of the power of the − supermode is in the signal spectrum and 9% is in the asymmetric spectral lobe within the interval $[s_1 = 2\pi \cdot 4.10, s_2 = 2\pi \cdot 5.53]$ rad/ps. Similar results are observed for the PS amplifier discussed below.

The PS operational mode in two coupled waveguide parametric amplifiers can be realised in a variety of scenarios [45, 46]. For the sake of clarity, we specify the initial condition as $\hat{\epsilon}^{(-)}(0, -\Omega) = \hat{\epsilon}^{(-)}(0, \Omega) \neq 0$ and $\hat{\epsilon}^{(+)}(0, -\Omega) = \hat{\epsilon}^{(+)}(0, \Omega) = 0$. Additionally, we assume that the phase difference between signal wave in waveguide 1 and the pump wave is ϕ_s,

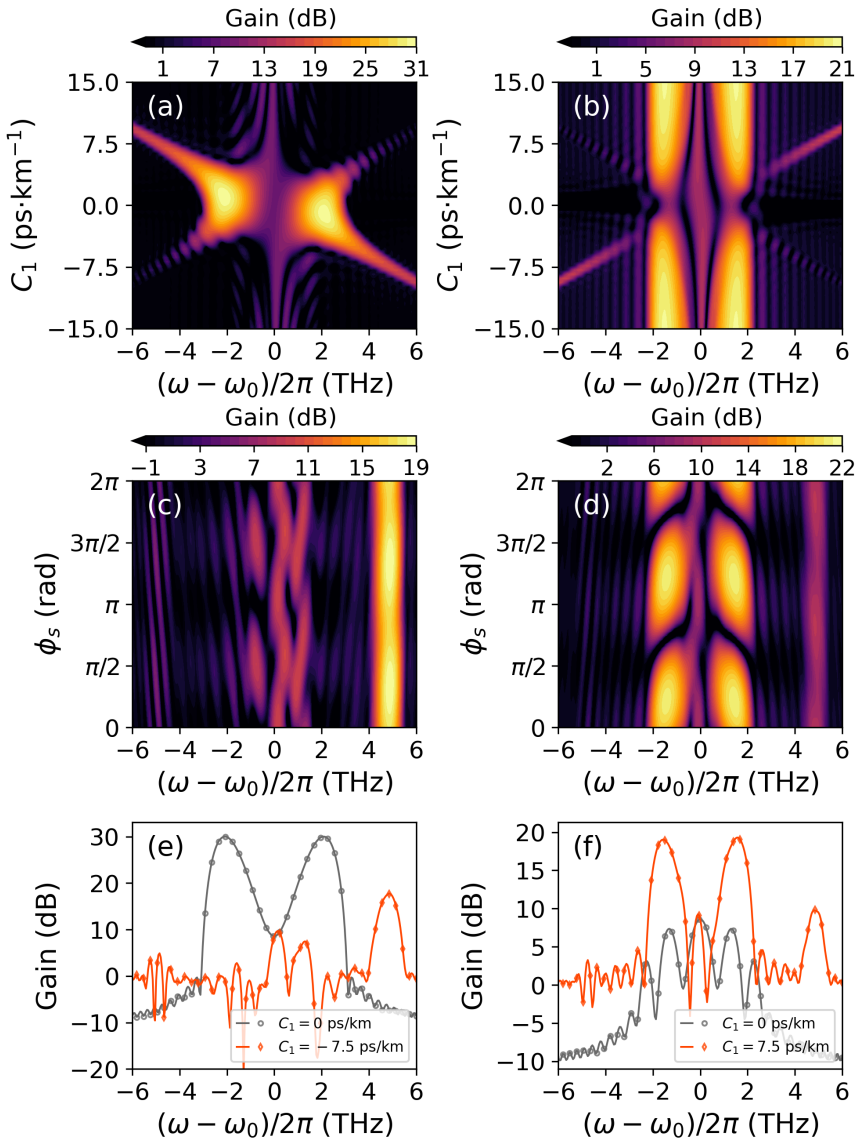

Figure 6.3: PS amplifier with "−" signal input. Map of analytical parametric gain for $E^{(-)}$ vs frequency and C_1 in anomalous (a) and normal (b) dispersion regime with $\phi_s = 0$, and vs frequency and ϕ_s in anomalous (c) and normal (d) dispersion regime with $C_1 = \mp 7.5$ ps$\cdot$km^{-1}; gain spectrum vs frequency comparison between theory (continuous line) and numerics (dots) for anomalous (e) and normal (f) dispersion regime with $\phi_s = 0$ and $C_1 = \mp 7.5$ps$\cdot$km^{-1} ($C_1 = 0$) shown in orange (gray). Remaining parameters are like in Fig. 6.2.

leading to the following expression for gain:

$$G_{\mathrm{PS}}(z) = \begin{cases} |N_{33}(z)e^{i\phi_s} + N_{34}(z)e^{-i\phi_s}|^2, & \text{OPA} \\ |N_{43}(z)e^{i\phi_s} + N_{44}(z)e^{-i\phi_s}|^2, & \text{WLC.} \end{cases} \tag{6.6}$$

The characterisation of the PS amplifier is presented in Fig. 6.3. Additionally, we have examined the dependence of the gain spectrum on the pump power difference P_d, as illustrated in Fig. 6.4 for both PI and PS operational modes. Varying the pump power serves as an effective method for experimentally controlling the amplifier gain. The results indicate a trade-off between maximising the gain and minimising idler amplification. It is important

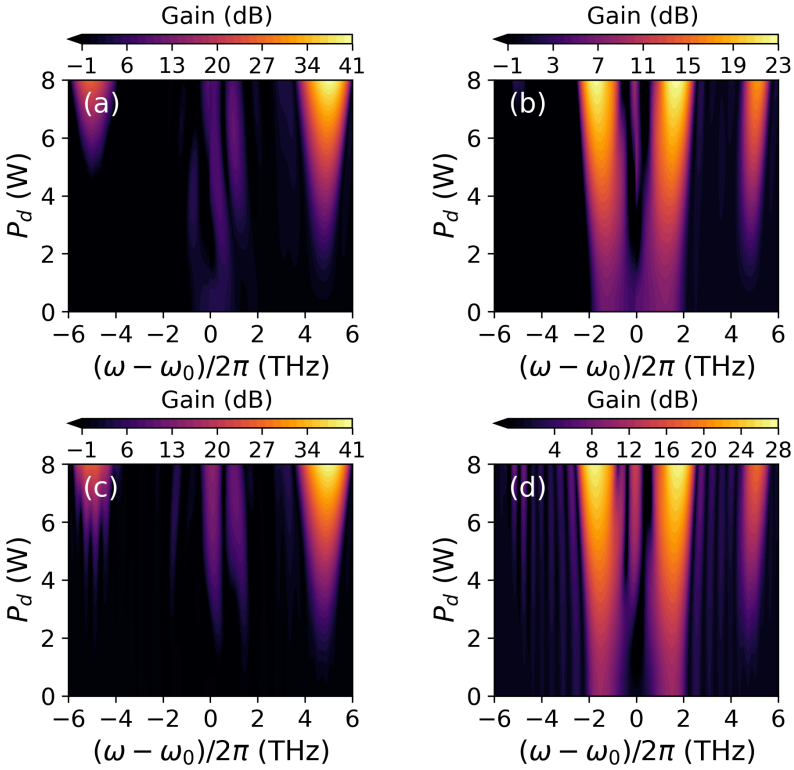

Figure 6.4: P_d-dependency. Map of PI analytical parametric gain for E_- vs frequency and P_d in anomalous (a) and normal (b) dispersion regime; and map of PS parametric analytical gain vs frequency and P_d in anomalous (c) and normal (d) dispersion regime with $\phi_s = 0$. Other parameters used are $C_1 = \mp 7.5$ ps $\cdot$ km^{-1}, $\beta_2 = \mp 0.5$ ps^{2}km^{-1}, $\gamma = 10$ W^{-1}km^{-1}, $C_0 = 15$ km^{-1}, $C_2 = 0$, and $z = 0.1$ km. The variation of P_d depicted corresponds to a change of P_t in the interval $[3, 8.5]$ W.

to stress that the gain asymmetry for signal and idler waves between different supermodes discussed here is not related to odd dispersion terms β_{odd}, which in our system results in a simple phase factor as it can be appreciated from the definition of $\hat{\eta}^{(\pm)}$. Furthermore, while the impact of C_1 on the MI spectrum in asymmetrically pumped dual core fibres has been investigated in [56, 57], in those works the frequency asymmetric gain spectrum for different supermodes was not observed, possibly because the focus was on the eigenvalue spectrum of the CW stability problem (which is symmetric in frequency) and the parametric gain was not calculated by fully solving the signals and idlers equations. Both in the PI

and PS regime, the amplifier asymmetric gain spectrum is due to the combined action of the unbalanced pump power distribution between the two waveguides and of the frequency dependency of the coupling. Notably, $P_d \neq 0$ causes supermodes mixing as it can be clearly seen from Eqs. 6.3 and 6.4 showing that the supermode coupling matrix M_c is nonvanishing only if $P_d \neq 0$. In that case, even if one supermode only is injected inside the amplifier, the nonlinear dynamics couples energy into the other supermode too. If $C_1 \neq 0$ is further satisfied, while the four-wave mixing process keeps its symmetric spectral feature, then the signals remain located in one supermode while the idlers are located in the other supermode. This point can be observed in Fig. 6.5, where "+" supermode is amplified with "−" signal input. As in the normal dispersion the signal-idler separation between supermodes

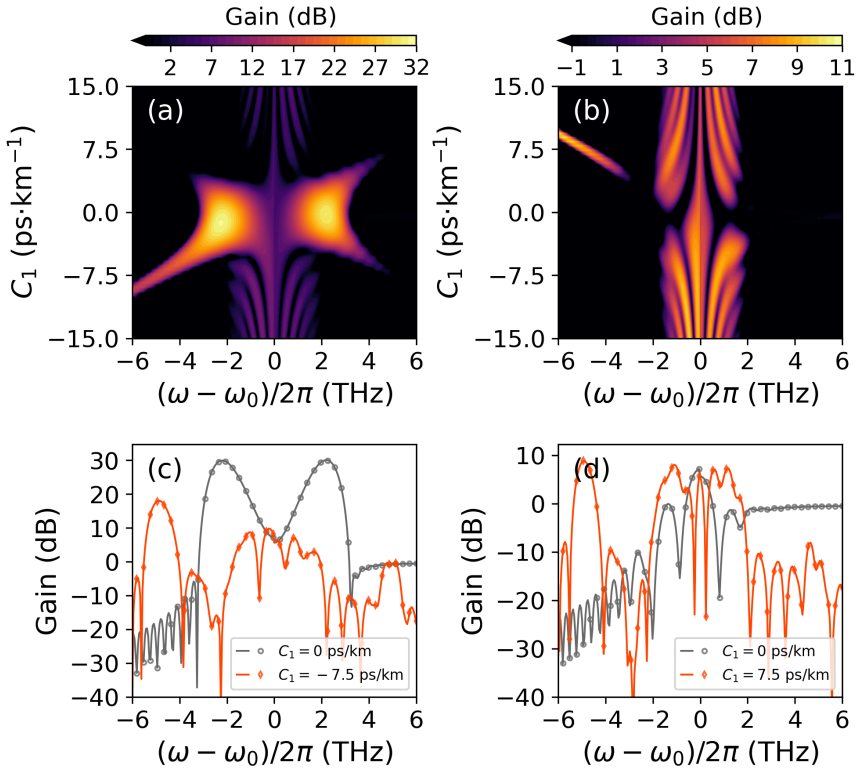

Figure 6.5: PI amplifier with "−" signal input. Map of analytical parametric gain for $E^{(+)}$ vs frequency and C_1 in anomalous (a) and normal (b) dispersion regime; and comparison of gain spectrum vs frequency between theory (continuous line) and numerics (dots) for anomalous (c) and normal (d) dispersion regime with $C_1 = \mp 7.5$ ps $\cdot$ km^{-1} ($C_1 = 0$) shown in orange (gray). Other parameters used are $\beta_2 = \mp 0.5$ ps^{2}km^{-1}, $\gamma = 10$ W^{-1}km^{-1}, $P_p = 5.4$ W, $C_0 = 15$ km^{-1}, $C_2 = 0$, and $z = 0.1$ km.

is not complete and it does not apply in the low frequency range, the anomalous dispersion regime the most attractive for a full separation of signals and idlers. An analytical expression for the gain difference in dB between the two supermodes as a function of the

dominant eigenvector $\mathbf{v}_1 = (v_1, v_2, v_3, v_4)^T$ of matrix M can be derived (see Appendix C.1) and reads: $G^{\pm}_{\text{diff}} = 10\log\frac{|e_{s\pm}|^2}{|e_{i\pm}|^2} = 10\log\left|\frac{v_{2\mp1}}{v_{3\mp1}}\right|^2$. A further intuitive picture of the reason for the frequency asymmetric gain of the two supermodes can be provided by considering that in the asymmetric operational regime signal waves for the individual waveguides modes ($\hat{\epsilon}^{(1,2)}(z,\Omega)$) exhibit a π phase difference, while idlers ($\hat{\epsilon}^{(1,2)}(z,-\Omega)$) have no phase difference (see Appendix C.2). We can attribute the origin of this phase-shift to the interplay between the asymmetric pump power distribution between the two cores and C_{odd} — the odd part of the frequency dependent coupling — which are the necessary ingredients for the intermodal four-wave mixing to occur. As supermodes "±" are defined by the sum/difference between individual waveguides modes respectively, i.e., $E_{\pm} = (E_1 \pm E_2)/\sqrt{2}$, this unequal phase difference translates, due to interference, into the fact that one supermode is idler-free and the other one is signal-free (at least in a certain frequency bandwidth). While the supermode carrying the signals can be used for idler-free amplification purpose, the supermode carrying the idlers, E_+ in our examples, can be used for wavelength conversion applications. The two supermodes can be easily extracted at the amplifier output by a simple combination of a phase shifter and a coupler, as shown in Fig. 3.1.

We have furthermore verified through numerical simulations that the undepleted pump approximation assumed in the analytical theory is excellent for the parameters used in this study (input signals power $\sim 10^{-12}$ W) as pump depletion is negligible, resulting in an about $10^{-9}\%$ of pump power reduction between output and input. The validity of this assumption can also be appreciated indirectly from the nice agreement between theory and simulations across the whole chapter.

6.4 Conclusions

In conclusion, we have presented parametric amplification facilitated by intermodal four-wave mixing in a dual-core optical fibre. We have demonstrated that the interaction between frequency-dependent coupling and pump power imbalance in two coupled nonlinear waveguides is the primary factor for achieving signal and idler separation through frequency-asymmetric gain for the two system supermodes. Our findings indicate that this separation is feasible using realistic dual-core fibre parameters. Our rigorous analytical theory aligns closely with the results of numerical simulations and will serve as a guide for the future de-

sign of experimental demonstrations of the proposed concept. It aims to optimise idler-free amplifier performance—specifically in areas such as bandwidth, maximum gain, and energy efficiency—as well as to investigate potential impairments. Moreover, our framework can be adapted to describe coupled waveguides composed of different materials, such as silicon and silicon nitride. The results discussed in this chapter have the potential to enable a more efficient utilisation of bandwidth in optical parametric amplification and may also have applications for wavelength conversion.

Part II

Modulation instability and frequency comb generation in fibre ring resonators

Chapter 7

Basic theory of fibre ring resonators

MI in fibre ring resonators was observed for the first time in 1988 [81]. MI in fibre ring resonators is different from that in open fibres discussed in Section 2.6.2, where anomalous dispersion is required, cavity-enhanced MI can occur even in the normal dispersion regime due to parametric gain enabled by the periodic boundary conditions (BCs) and detuned pumping [82, 83]. This intracavity MI serves as a precursor to OFC generation and temporal pattern formation in passive and active resonators. The underlying physics can be described using models such as the Ikeda map or mean-field equations like the LLE [84, 82, 83]. Understanding MI in resonators is crucial for designing Kerr comb systems, mode-locked fibre lasers, and microresonator-based photonic devices [85, 86].

As mentioned in Section 2.6.2, OFCs have crucial applications including precision spectroscopy, optical atomic clocks, high-capacity coherent communications, and astronomical spectrograph calibration [38]. A wide range of platforms can be employed to generate OFCs, including mode-locked lasers [87], electro-optic modulation techniques [88], and externally driven resonators, both in micro-scale [89] and fibre-based implementations [90]. Among these, fibre resonators have historically served as a foundational testbed for OFC generation strategies—many of which were later translated to integrated platforms. Notable examples include the observation of cavity soliton formation [91]. In specific configurations, fibre resonators can also achieve quality (Q) factors on the order of several million, enabling OFC generation in both single-mode [92, 93, 94] and multimode [95] regimes.

In the context of fibre-based cavities, a recently developed method known as GTF has enabled tunable-repetition-rate OFC generation in passively driven ring resonators [96, 97]. The key principle of this technique is to exploit the phase contribution of a spectral filter to achieve perfect phase matching between a strong pump and weak sidebands in the normal dispersion regime of the cavity. This facilitates the onset of MI, resulting in the generation of symmetric sidebands around the pump, one of which lies near the filter resonance. Subsequent cascaded four-wave mixing generates higher-order sidebands, ultimately forming an OFC whose line spacing can be tuned by adjusting the detuning between the pump and the filter.

In this chapter, we will introduce the fundamental mathematical tools for describing optical wave propagation in fibre ring resonators, specifically the Ikeda map model and the LLE. Building upon these models, we will examine the MI. At the end of this chapter, we will present the GTF instability and GTF-based OFC generation, which will serve as the foundation for Chapters 8 and 9.

7.1 Ikeda map model

The wave envelope $A_n(z,t)$ evolving in a co-moving reference frame with temporal coordinate t and spatial coordinate z inside a fibre ring cavity of length L, with n denoting the round trip number, is governed by the NLSE. Along with the corresponding BCs, the complete dynamics of $A_n(z,t)$ inside the cavity is given by

$$\frac{\partial A_n}{\partial z} = -i\frac{\beta_2}{2}\frac{\partial^2 A_n}{\partial t^2} + i\gamma|A_n|^2 A_n, \tag{7.1a}$$

$$A_{n+1}(0,t) = \rho e^{i\varphi_0} A_n(L,t) + \theta\sqrt{P_{\text{in}}}. \tag{7.1b}$$

Here, β_2 denotes the GVD, γ is the Kerr nonlinearity coefficient, θ is the coupler transmission coefficient, and $\rho = \xi\sqrt{1-\theta^2}$ is the effective power reflection coefficient, with loss coefficient ξ accounting for fibre loss and splicing loss. The linear phase accumulation over a round trip is given by φ_0 (modulo 2π), and P_{in} is the input pump power. Eqs. (7.1) is commonly referred to in the literature as the Ikeda map. Strictly speaking, this is a generalized Ikeda map, since Ikeda's original works did not include GVD and were formulated for dispersionless Kerr cavities [98]. The inclusion of GVD extends the model to the

regime relevant for fibre-ring resonators. The Ikeda-type dynamics has been experimentally investigated in fibre-based systems, notably in the pioneering work of Nakatsuka et al. [99], demonstrating period-doubling bifurcations.

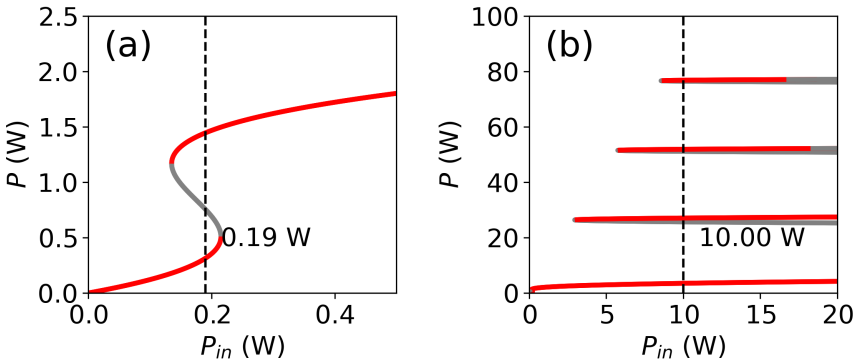

Figure 7.1: Stationary CW solutions. (a) bistability at $P_{\text{in}} = 0.19$ W. (b) multistability at $P_{\text{in}} = 10$ W. Red and gray parts represent stable and unstable CW solutions, respectively. Parameters: $\varphi_0 = -0.1\pi$, $\gamma = 2.5$ W^{-1}km^{-1}, $\rho = \sqrt{0.8}$, $\theta = \sqrt{0.1}$, $L = 0.1$ km, and $\beta_2 = 0.4$ ps^2/km.

By setting $\frac{\partial A_n}{\partial t} = 0$ and $A_{n+1}(0) = A_n(0)$, we find the stationary solutions of Eqs. (7.1): $A_n(z) = A_p(z) = \sqrt{P}e^{i\gamma Pz}$, where the intracavity power is given by $P = \frac{\theta^2 P_{\text{in}}}{1+\rho^2-2\rho\cos(\varphi_0+\gamma PL)}$. Figs. 7.1 demonstrated the relation between the intracavity power and input power. The red parts indicate that the CW solutions are stable against zero-mode perturbations, whereas the gray parts denote unstable CW solutions. From Figs. 7.1(a), we can see that varying the input power allows us to access monostable and bistable regimes. Furthermore, as depicted in Figs. 7.1(b), increasing the input power can lead to the emergence of multistability. The stability of CW solutions is basically determined by examining whether the MI gain at $\Omega = 0$ larger than 0.

7.2 MI analysis based on Ikeda map

The MI analysis of the cavity dynamics based on Ikeda map is a Floquet analysis, which can be divided into two parts: the NLSE and the BCs. Following Section 2.6, starting from

$$A_n(z,t) = A_p(z) + \epsilon_n(z,t), \tag{7.2}$$

where ϵ_n is the perturbations, we can derive a evolution equation for perturbations $\eta_n(z,t) = \epsilon_n(z,t)e^{-i\gamma Pz}$ governed by the matrix M_{evo} (denoted by M in Section 2.6) as follows:

$$\partial_z \begin{pmatrix} \hat{\eta}_n(z,\Omega) \\ \hat{\eta}_n^*(z,-\Omega) \end{pmatrix} = M_{\text{evo}} \begin{pmatrix} \hat{\eta}_n(z,\Omega) \\ \hat{\eta}_n^*(z,-\Omega) \end{pmatrix}. \tag{7.3}$$

Applying this equation to one-round trip propagation, we find

$$\begin{aligned} \begin{pmatrix} \hat{\eta}_n(L,\Omega) \\ \hat{\eta}_n^*(L,-\Omega) \end{pmatrix} &= N_{\text{evo}} \begin{pmatrix} \hat{\eta}_n(0,\Omega) \\ \hat{\eta}_n^*(0,-\Omega) \end{pmatrix} \\ &= \begin{pmatrix} \cosh(qL) + iKL\frac{\sinh(qL)}{qL} & i\gamma PL\frac{\sinh(qL)}{qL} \\ -i\gamma PL\frac{\sinh(qL)}{qL} & \cosh(qL) - iKL\frac{\sinh(qL)}{qL} \end{pmatrix} \begin{pmatrix} \hat{\eta}_n(0,\Omega) \\ \hat{\eta}_n^*(0,-\Omega) \end{pmatrix}. \end{aligned} \tag{7.4}$$

with $K(\Omega) = \frac{\beta_2}{2}\Omega^2 + \gamma P$, and $q(\Omega) = \sqrt{(\gamma P)^2 - K^2(\Omega)}$ being one of the eigenvalues of M_{evo} (another one is $-q$).

On the other hand, from the BCs Eq. (7.1b), we find

$$\hat{\eta}_{n+1}(0,\Omega) = \rho e^{i(\varphi_0+\gamma PL)}\hat{\eta}_n(L,\Omega), \tag{7.5}$$

which in the matrix form reads

$$\begin{aligned} \begin{pmatrix} \hat{\eta}_{n+1}(0,\Omega) \\ \hat{\eta}_{n+1}^*(0,-\Omega) \end{pmatrix} &= N_{\text{BC}} \begin{pmatrix} \hat{\eta}_n(L,\Omega) \\ \hat{\eta}_n^*(L,-\Omega) \end{pmatrix} \\ &= \begin{pmatrix} \rho e^{i(\varphi_0+\gamma PL)} & 0 \\ 0 & \rho e^{-i(\varphi_0+\gamma PL)} \end{pmatrix} \begin{pmatrix} \hat{\eta}_n(L,\Omega) \\ \hat{\eta}_n^*(L,-\Omega) \end{pmatrix}. \end{aligned} \tag{7.6}$$

Finally, the wave in two consecutive round trips are related by the following equation:

$$\begin{pmatrix} \hat{\eta}_{n+1}(0,\Omega) \\ \hat{\eta}_{n+1}^*(0,-\Omega) \end{pmatrix} = N \begin{pmatrix} \hat{\eta}_n(L,\Omega) \\ \hat{\eta}_n^*(L,-\Omega) \end{pmatrix}, \tag{7.7}$$

where we have defined the Floquet matrix $N = N_{\text{evo}}N_{\text{BC}}$, and the Floquet multipliers, i.e., eigenvalues of N read

$$\lambda_\pm = \rho\left(\Delta \pm \sqrt{\Delta^2 - 1}\right), \tag{7.8}$$

where

$$\Delta(\Omega) = \cosh(qL)\cos(\varphi_0 + \gamma PL) - \frac{KL\sinh(qL)}{qL}\sin(\varphi_0 + \gamma PL). \tag{7.9}$$

Then the MI gain per round trip reads $G \sim \lambda^2$, with $\lambda = \max(|\lambda_+|, |\lambda_-|)$, and the gain in decibels per unit length reads

$$g_{\mathrm{dB}} = \frac{20}{L}\log_{10}\lambda. \tag{7.10}$$

In Fig. 7.2(a), MI gain calculated by this equation is illustrated.

A non-zero MI gain corresponds to $\lambda > 1$, which requires $|\Delta| > (\rho^2 + 1)/2\rho$. In the good cavity limit, i.e., $\rho \approx 1$, this is approximately equivalent to $|\Delta| > 1$. Considering $2\gamma P \ll |\beta_2\Omega^2/2|$, i.e., $|\Omega| \gg 2\sqrt{\gamma P/|\beta_2|}$, we have $q(\Omega) \approx \pm iK(\Omega)$, which leads to

$$\Delta \approx \cos(KL + \varphi_0 + \gamma PL) = \cos(\frac{\beta_2}{2}\Omega^2 L + \varphi_0 + 2\gamma PL). \tag{7.11}$$

The potentially unstable frequencies maximise $|\Delta|$ and satisfy the following phase matching condition:

$$\frac{\beta_2}{2}\Omega^2 L + \varphi_0 + 2\gamma PL = k\pi, \tag{7.12}$$

where Ω is the frequency detuning of the sidebands with respect to the pump, and $k = 0, \pm1, \pm2, ...$ [100, 101, 97]. Physically, KL is the phase shift acquired by the propagation on top of the CW, while $\varphi_0 + \gamma PL$ is the phase shift of CW over one round trip. The modulation mode reaches maximum gain when the total phase shift over one round trip is an integer multiple of π. More specifically, an even k (or a real and positive λ) corresponds to a period-1 (P1) MI, in which the intracavity CW solution develops a harmonic temporal modulation that repeats identically every round trip. This behaviour is characteristic of operation close to the cavity resonance ($\varphi_0 = 0$). In contrast, an odd k (or a real and negative λ) corresponds to a period-2 (P2) MI, where the modulation alternates between successive round trips, as illustrated in Fig. 7.2(b). Such alternation reflects operation close to the antiresonance condition ($\varphi_0 = \pi$).

7.3 Lugiato-Lefever equation

Originally the LLE was derived by Lugiato and Lefever in the context of diffractive driven Kerr resonators [84] and subsequently by Haelterman, Trillo and Wabnitz to describe passive

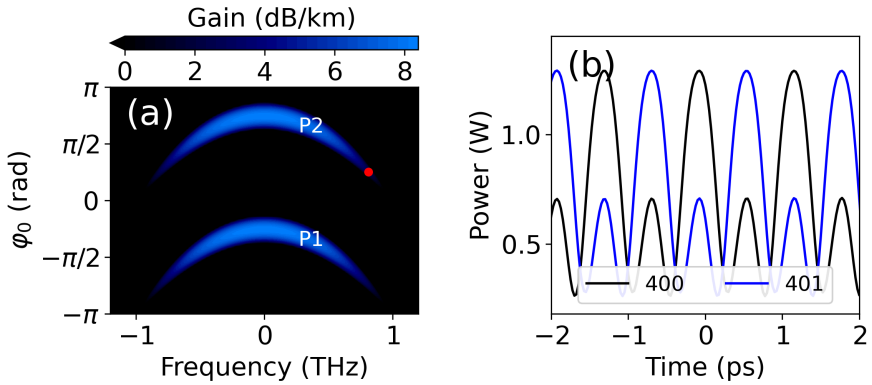

Figure 7.2: (a) MI gain map vs φ_0 with fixed intracavity power $P = 0.55$ W. (b) Simulation results with $P_{\text{in}} = 6.32$ W: intracavity power of two consecutive round trips (400 and 401) in the modulationally unstable regime indicated by the red dot in (a). Parameters used are $\varphi_0 = 0.25\pi$, $\gamma = 2.5$ W^{-1}km^{-1}, $\rho = \sqrt{0.8}$, $\theta = \sqrt{0.1}$, $L = 0.3$ km, and $\beta_2 = 0.4$ ps^2/km.

driven ring fibre resonators [82, 83]. LLE is an approximate model for describing wave propagation in a driven, dissipative Kerr cavity. While it simplifies the full field dynamics by averaging over each round trip (mean-field approximation), it remarkably captures many of the essential features that govern the behaviour of nonlinear resonators. These include the onset of MI, the generation and stabilisation of Kerr frequency combs, the formation of temporal cavity solitons, and the emergence of periodic or chaotic patterns depending on system parameters.

If we use Z to denote the total distance the envelope passed through, i.e., $Z = nL + z$, the envelope $A_n(z,t)$ can be simply represented by $A(Z,t)$. That is $A(Z,t) = A_n(z,t)$ with $z = Z \pmod L$ and $n = \lfloor \frac{Z}{L} \rfloor$. The propagation of field $A(Z,t)$ is approximately governed by the LLE as follows:

$$L\partial_Z A = (-\alpha_T + i\varphi_0 - i\frac{\beta_2}{2}L\partial_t^2 + i\gamma L|A|^2)A + \theta\sqrt{P_{\text{in}}} \tag{7.13}$$

where α_T is the effective field loss, usually approximated by $\alpha_T = 1 - \rho$.

A CW solution of LLE is of the form $A(Z,t) = A_p = \sqrt{P}\,e^{i\phi_0}$, where P and ϕ_0 are the power and phase, respectively. Substituting this solution form into Eq. (7.13), we find the relationship between the intracavity power P and the input power P_{in}:

$$P = \frac{\theta^2 P_{\text{in}}}{\alpha_T^2 + (\varphi_0 + \gamma P L)^2}. \tag{7.14}$$

The power relation is illustrated in Fig. 7.3(a)-(b). We observe both monostability and

bistability, similar to the results obtained from the Ikeda map, as shown in Fig. 7.3(a). However, in the case of LLE, no multistability can be observed and only the lowest branch of the CW solution can be reproduced, as shown in Fig. 7.3(b).

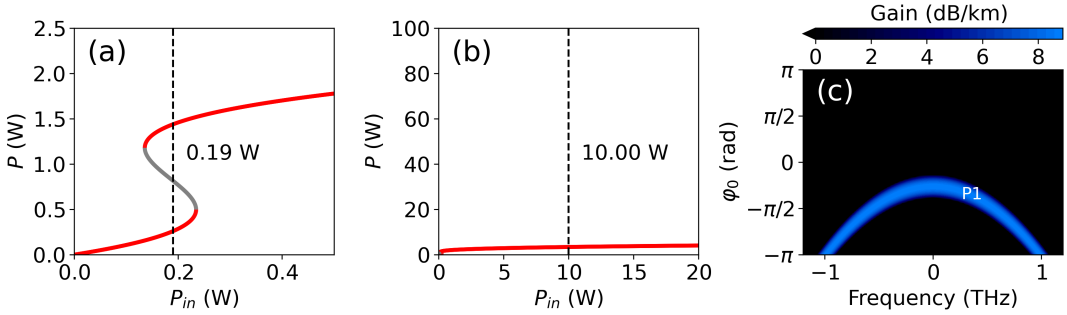

Figure 7.3: (a) Stationary CW solutions for LLE. Bistability appears around $P_{\text{in}} = 0.19$ W. Parameters used are the same as those in Fig. 7.1. (b) MI gain vs φ_0 calculated based on LLE. Parameters used are the same as those in Fig. 7.2.

7.4 MI analysis based on LLE

Akin to the MI analysis based on Ikeda map, to do an LLE-based MI analysis, we start from the following assumption:

$$A(Z,t) = A_p + \epsilon(Z,t), \tag{7.15}$$

where ϵ is the perturbations. Substituting Eq. (7.15) into the LLE [Eq. (7.13)], the evolution equation of ϵ can be derived:

$$\partial_Z \epsilon = \left[\frac{-\alpha_T + i\varphi_0}{L} - i\frac{\beta_2}{2}\partial_t^2\right]\epsilon + i\gamma 2P\epsilon + i\gamma P e^{i2\phi_0}\epsilon^*. \tag{7.16}$$

Performing Fourier transform, we obtain

$$\partial_Z \begin{pmatrix} \hat{\epsilon}(Z,\Omega) \\ \hat{\epsilon}^*(Z,-\Omega) \end{pmatrix} = M \begin{pmatrix} \hat{\epsilon}(Z,\Omega) \\ \hat{\epsilon}^*(Z,-\Omega) \end{pmatrix} = \left[d\mathcal{I} + \begin{pmatrix} S & V \\ V^* & -S \end{pmatrix}\right] \begin{pmatrix} \hat{\epsilon}(Z,\Omega) \\ \hat{\epsilon}^*(Z,-\Omega) \end{pmatrix}, \tag{7.17}$$

where we have defined $d = -\frac{\alpha_T}{L}$, $S = i\frac{\varphi_0}{L} + i\frac{\beta_2}{2}\Omega^2 + i2\gamma P$, and $V = i\gamma P e^{i2\varphi_0}$. The matrix M has two eigenvalues $\lambda_\pm(\Omega) = d \pm \sqrt{S^2(\Omega) + |V|^2}$, thus the MI gain reads

$$g_{\text{db}} = \frac{20}{\ln 10}\text{Re}[\lambda_+(\Omega)]. \tag{7.18}$$

The MI gain is illustrated in Fig. 7.3(c). Compared to the Ikeda map, LLE is able to capture the P1 MI gain band, but not able to reproduce the P2 MI gain band.

7.5 GTF instability and GTF-based OFC generation

In this section, we provide a detailed presentation of the mathematical models used to describe the GTF instability. We also analyse the analytical MI gain and examine the generation of OFCs with tunable repetition rates, as demonstrated through both simulations and experimental results. The discussion is primarily based on Refs. [96, 97].

7.5.1 Mathematical model

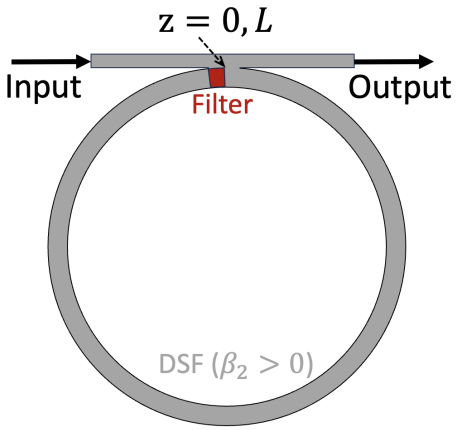

Figure 7.4: Setup schematic: a fibre ring cavity with an incorporated spectral filter before the coupler.

A GTF cavity is illustrated in Fig. 7.4, comprising three components: a dispersion-shifted fibre (DSF, $\beta_2 > 0$ at the driving frequency), a narrowband spectral filter, and a fibre coupler. A spectral filter located at $z = z_F$ modifies the field as [97]

$$A_n(z_F+, t) = h(t) \star A_n(z_F-, t), \tag{7.19}$$

where the symbol $\star$ denotes convolution in time, i.e., for two arbitrary functions $f(t)$ and $g(t)$, $f \star g = \int_{-\infty}^{\infty} f(t-t')g(t')\,dt'$. Here, $h(t)$ is the impulse response and $H(\omega) = \int_{-\infty}^{\infty} h(t)e^{i\omega t}$ is the transfer function. We adopt, without loss of generality, a higher-order Lorentzian filter

with

$$H(\Omega) = e^{F(\Omega)+i\psi(\Omega)}, \tag{7.20a}$$

$$F(\Omega) = b\frac{a^4}{(\Omega-\Omega_f)^4+a^4}, \tag{7.20b}$$

$$\psi(\Omega) = ba\frac{(\Omega-\Omega_f)[(\Omega-\Omega_f)^2+a^2]}{\sqrt{2}[(\Omega-\Omega_f)^4+a^4]}, \tag{7.20c}$$

where a (rad/ps) sets the bandwidth, $b < 0$ controls the depth, and Ω_f is the central frequency. The amplitude and phase profiles of $H(\Omega)$ are examplified in Fig. 7.5. Notably, $\psi(\Omega) \neq 0$ at $\Omega = 0$, which adds a linear phase shift per round trip and leads to a redefined effective detuning given by $\varphi_0' = \varphi_0 + \psi(0)$.

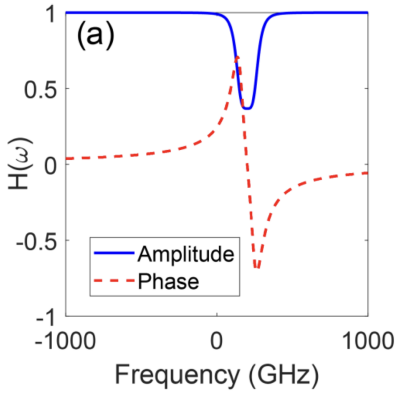

Figure 7.5: Amplitude and phase of the filter [97].

If we include the effect of the spectral filter into BCs, we find [97]:

$$A_{n+1}(z=0,t) = \rho e^{i\varphi_0} h(t) \star A_n(z=L,t) + \theta\sqrt{P_{\text{in}}}. \tag{7.21}$$

which together with the NLSE governs the dynamics of the wave envelope $A_n(z,t)$.

If we consider that near $z = z_F$, Eq. (7.19) can be written as

$$\frac{\partial A_n(z,t)}{\partial z} = \delta(z-z_F)\,(\Phi + i\Psi) \star A_n(z,t), \tag{7.22}$$

with Φ and Ψ the inverse Fourier transforms of $F(\Omega)$ and $\psi(\Omega)$, respectively, a generalised LLE for the cavity with spectral filtering can be derived [97]:

$$L\partial_z A = [-\alpha_T + i\varphi_0 + (\Phi + i\Psi)\star]A + \left(-i\frac{\beta_2}{2}L\partial_t^2 + i\gamma L|A|^2\right)A + \theta\sqrt{P_{\text{in}}}. \tag{7.23}$$

7.5.2 GTF instability

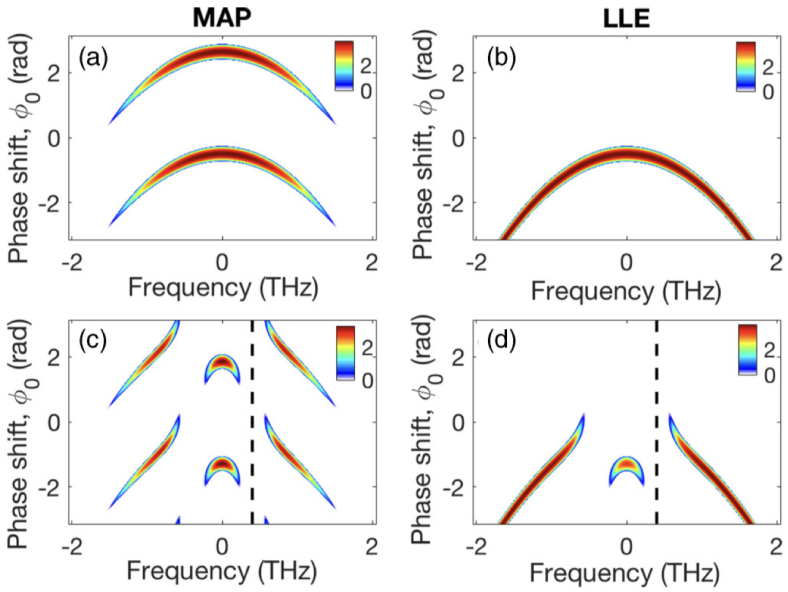

Figure 7.6: MI gain of the fibre ring resonator in the normal dispersion regime without spectral filtering calculated by Ikeda map (a) and LLE (b). MI gain of the fibre ring resonator in the normal dispersion regime with blue-detuned spectral filtering calculated by Ikeda map (c) and LLE (d). The dashed lines indicate the central frequency of the spectral filter. [97].

Both the Ikeda map and LLE are applicable for MI analysis. A comprehensive formulation is provided in Ref. [97]. The MI gain calculated based on these two models is illustrated in Fig. 7.6. Compared to the case without spectral filtering [(a) and (b)], the incorporation of spectral filter breaks the normal MI gain band, and enables GTF instability [(c) and (d)]. The new MI gain bands emerge near the filter central frequency and at the frequency symmetric with respect to the pump, since only the even part of the filter. Depending on whether the filter is placed on the red- or blue-shifted side of the pump, these bands appear either on the inner or outer side relative to the filter central frequency [97]. Although the LLE typically fails to capture the P2 MI, it is sufficient to describe the GTF instability. As we will see in the next section, it is adequate for generating OFCs.

It is worth mentioning that although the spectral filter is asymmetric, the MI gain remains symmetric with respect to $\Omega = 0$. This is because the linearised Kerr–NLSE dynamics always couples the frequency components Ω and $-\Omega$ as a conjugate pair, so the Floquet eigenvalues depend only on the even part of any frequency-dependent phase term.

7.5.3 Tunable OFC generation

Initiated by GTF instability, the cascaded FWM can finally lead to the generation of OFCs. In Fig. 7.7, simulations performed through split-step Fourier method demonstrates the generation of OFCs based on both Ikeda map and LLE. In Fig. 7.7(a)-(b), the evolution of the temporal patterns over round trips are shown. The final stable patterns are shown in Fig. 7.7(c) and the corresponding power spectrum is shown in Fig. 7.7(d).

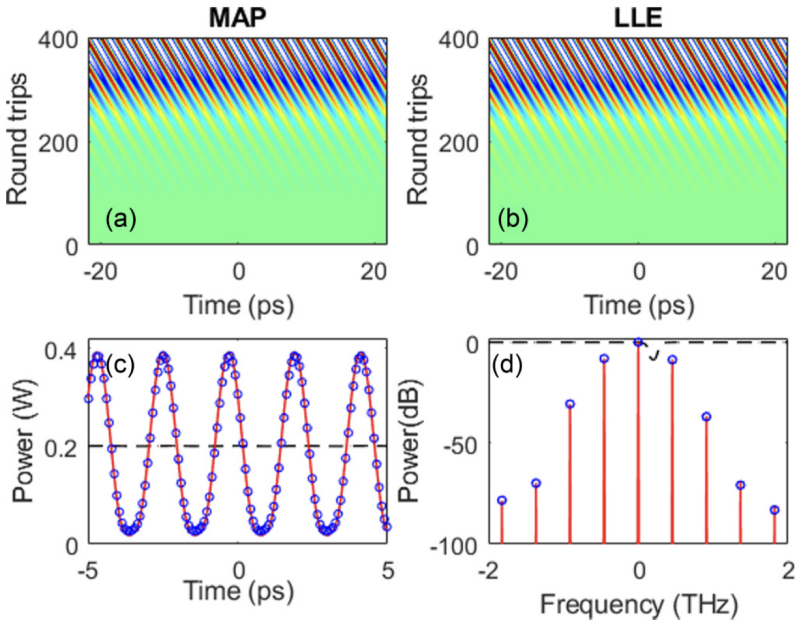

Figure 7.7: The evolution of the power over round trips simulated by Ikeda map (a) and LLE (b). The stable temporal pattern (c) and the corresponding power spectrum (d). [97].

As the location of GTF instability is linked to the offset between the filter central frequency and the pump frequency, it is feasible to control either of these parameters to alter the repetition rate of the generated OFCs. This concept has been demonstrated in experiments [96], and the results are shown in Fig. 7.8. From Fig. 7.8(b), it can be observed that as the offset between the pump frequency and the filter central frequency increases, the offset between the first comb line and the pump also increases, indicating a reduction in the OFC repetition rate.

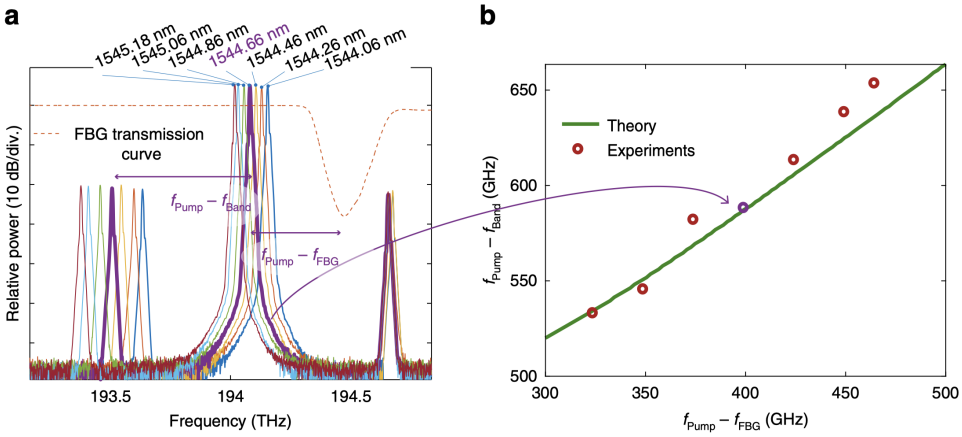

Figure 7.8: Tunable OFC. (a) Output spectra for various pump wavelengths. (b) Relation between the OFC repetition rate and the offset frequency between pump and filter.

Chapter 8

Amplifier enhanced Gain-Through-Filtering instability in a hybrid Kerr cavity

---

The work presented in this chapter has been adapted from the following publications:
[6] M. Shi, S. Negrini, N. Englebert, F. Leo, M. Conforti, A. Mussot, and A. M. Perego. Amplifier enhanced gain-through-filtering instability in a hybrid kerr cavity. *Opt. Express*, 33(21):43665–43675, 2025.

8.1 Introduction

GTF-based OFCs have been demonstrated in passive ring fibre resonators. However, these systems often require high pump power to overcome the MI threshold due to their inherently low finesse. Motivated by recent progress in hybrid active-passive fibre ring cavities—particularly those demonstrating low-background cavity solitons without filters [102, 103]—this work investigates the role of optical amplification in enhancing the GTF process. Specifically, we incorporate an intracavity EDFA to study its impact on OFC generation. We extend the theoretical framework introduced in Section 7.5 to account for amplifier dynamics and develop a formalism suitable for both analytical and numerical analysis of GTF in an active-passive fibre resonator. The theoretical predictions are validated experimentally, showing strong agreement with the observed results.

The inclusion of the intracavity amplifier significantly improves the conversion efficiency

from the pump to the OFC sidebands, effectively lowering the MI threshold and reducing the required input pump power.

8.2 Ikeda map model

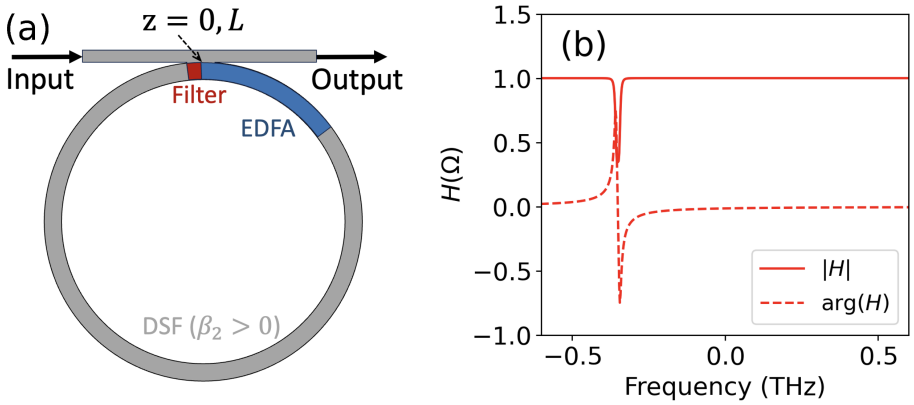

Figure 8.1: (a) Setup schematic: a fibre ring cavity consisting of an amplifier (EDFA), a passive fibre with normal dispersion (DSF), and a filter. (b) Amplitude and phase profiles of the filter transfer function $H(\Omega)$. Parameters used are $a = 0.043$ rad/ps, $b = -1.06$, and $\Omega_f/(2\pi) = -0.35$ THz.

We consider a ring cavity as illustrated in Fig. 8.1(a), comprising four components: an EDFA, a dispersion-shifted fibre (DSF, $\beta_2 > 0$ at the driving frequency), a narrowband filter, and a fibre coupler. The amplitude and phase profiles of filter transfer function $H(\Omega)$ are shown in Fig. 8.1(b), with parameters matching those used in the experimental setup (see Section 8.5). With the incorporation of EDFA, we need to separate the propagation equations for the envelope in the EDFA and DSF as follows:

$$0 \le z \le L_1: \quad \frac{\partial A_n}{\partial z} = \left(\frac{g}{2} + \frac{g}{2\Omega_g^2}\frac{\partial^2}{\partial t^2} - i\frac{\beta_2^{(1)}}{2}\frac{\partial^2}{\partial t^2} + i\gamma^{(1)}|A_n|^2 \right) A_n, \tag{8.1}$$

$$L_1 < z \le L: \quad \frac{\partial A_n}{\partial z} = \left(-i\frac{\beta_2^{(2)}}{2}\frac{\partial^2}{\partial t^2} + i\gamma^{(2)}|A_n|^2 \right) A_n. \tag{8.2}$$

Here, the indices 1 and 2 label the EDFA and passive fibre, respectively, and the total cavity length is denoted by $L = L_1 + L_2$. $\beta_2^{(1),(2)}$ represent the GVD coefficients, while $\gamma^{(1),(2)}$ are the Kerr nonlinearity coefficients. Ω_g denotes the angular frequency bandwidth of the gain. The EDFA gain is modeled following [104, 102] as $g(z) = \frac{g_0}{1+(P_{\text{sat}}t_R)^{-1}\int_0^{t_R}|A_n(z,t)|^2 dt}$, where g_0 is the small-signal gain, P_{sat} is the saturation power, and t_R is the round-trip time.

In the scenario involving a short pulse compared to the round-trip time, the term

$(P_{\text{sat}}t_R)^{-1}\int_0^{t_R}|A_n(L_1,t)|^2dt$ can be approximated by an integral over a certain time window, i.e., $\frac{r_D}{P_{\text{sat}}}t_W^{-1}\int_{t_W}|A_n(L_1,t)|^2dt$, where t_W is the width of the simulation time window, $r_D \equiv t_D/t_R$ is the time ratio between the pulse width t_D and the round-trip time t_R, and $\int_{t_W}$ represents the integral over t_W. Hence, we obtain $g = \frac{g_0}{1+(P_{\text{sat}}t_W)^{-1}\int_{t_W} r_D|A_n(L_1,t)|^2dt}$.

The stationary quasi-CW solution of the cavity is given by $A_n(z) = \sqrt{P_n(z)}e^{i\phi_n(z)}$, with real amplitude $\sqrt{P_n(z)}$ and phase $\phi_n(z)$. The gain is then expressed as $g = \frac{P_{\text{sat}}}{P_{\text{sat}}+r_D P_n(L_1)}g_0$, depending on the ratio r_D. The quantities P_n and ϕ_n can be obtained by solving Eqs. (8.1) and (8.2), which yield

$$0 \le z \le L_1: \quad P_n(z) = P_n(0)e^{gz},\ \phi_n(z) = \phi_n(0) + \gamma^{(1)}P_n(0)\frac{1}{g}(e^{gz}-1), \tag{8.3}$$

$$L_1 < z \le L: \quad P_n(z) = P_n(L_1),\ \phi_n(z) = \phi_n(L_1) + \gamma^{(2)}(z-L_1)P_n(L_1), \tag{8.4}$$

leading to

$$P_n(L) = P_n(0)e^{gL_1}, \tag{8.5}$$

$$\phi_n(L) = \phi_n(0) + \gamma^{(1)}P_n(0)\frac{1}{g}(e^{gL_1}-1) + \gamma^{(2)}P_n(0)L_2e^{gL_1}. \tag{8.6}$$

Considering the BCs for the steady-state solution, we obtain

$$A_{n+1}(0) = \rho e^{i\varphi_0}H(0)A_n(L) + \theta\sqrt{P_{\text{in}}}. \tag{8.7}$$

Finally, the requirement $A_{n+1}(0) = A_n(0)$ yields the implicit form of the steady-state solution:

$$\sqrt{P(0)} - \sqrt{P(0)}\mu e^{i\nu} = \theta\sqrt{P_{\text{in}}}e^{-i\phi(0)} \tag{8.8}$$

where $\mu = \rho e^{\frac{gL_1}{2}+F(0)}$ and $\nu = \varphi_0' + \gamma^{(1)}P(0)\frac{1}{g}(e^{gL_1}-1) + \gamma^{(2)}P(0)L_2e^{gL_1} = \varphi_0' + \gamma^{(1)}P(L_1)\frac{1}{g}(1-e^{-gL_1}) + \gamma^{(2)}P(L_1)L_2$. Taking the square modulus of both sides of Eq. (8.8), we obtain

$$P(L_1)e^{-gL_1}\left[1+\mu^2-2\mu\cos\nu\right] = \theta^2P_{\text{in}}, \tag{8.9}$$

by which the intracavity power $P(L_1)$ can be determined. The relationship between the injected and intracavity powers is shown in Fig. 8.2.

If we assume that the nonlinear phase shift is small compared to the linear phase φ_0',

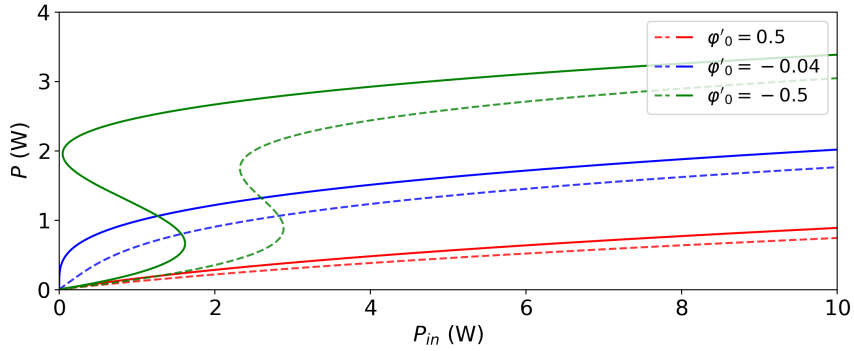

Figure 8.2: Relation between input and intracavity power calculated by the Ikeda map with EDFA (solid lines) and without EDFA (dashed lines). Parameters used are $\rho = \sqrt{0.65}$, $\theta = \sqrt{0.03}$, $g_0 = 4.87$ dB/m, $P_{\text{sat}} = 500$mW, $r_D = 1.3/451$, $\gamma^{(1)} = 1.3$ W^{-1}km^{-1}, $\gamma^{(2)} = 3$ W^{-1}km^{-1}, $L_1 = 0.33$ m, $L_2 = 85$ m, and $a = 0.043$ rad/ps, $b = -1.06$ and $\Omega_f/(2\pi) = -0.35$ THz.

Eq. (8.8) yields the following power relation:

$$P(0) \approx \frac{\theta^2 P_{\text{in}}}{\left|1 - \rho' e^{i\varphi_0'}\right|^2} = \frac{\theta^2 P_{\text{in}}}{1 + \rho'^2 - 2\rho' \cos\varphi_0'}, \tag{8.10}$$

where we define $\rho' = \rho e^{\frac{gL_1}{2} + F(0)}$. The maximum power occurs when $\varphi_0' = 2k\pi$, giving $P(0) = \frac{\theta^2 P_{\text{in}}}{(1-\rho')^2}$. We then seek the value of φ_0' that yields half the maximum power, i.e.,

$$\frac{\theta^2 P_{\text{in}}}{1 + \rho'^2 - 2\rho' \cos\varphi_0'} = \frac{1}{2} \frac{\theta^2 P_{\text{in}}}{(1-\rho')^2}. \tag{8.11}$$

If we focus on values of φ_0' close to zero, we can approximate $\cos\varphi_0' \approx 1 - \frac{\varphi_0'^2}{2}$. This leads to $\varphi_0' = \pm\frac{1-\rho'}{\sqrt{\rho'}}$. Thus, the full width at half-maximum (FWHM) of φ_0' is $\frac{2(1-\rho')}{\sqrt{\rho'}}$, and the finesse of the ring cavity is given by

$$\mathcal{F} = \frac{\pi\sqrt{\rho'}}{1-\rho'}. \tag{8.12}$$

8.3 Modulation instability analysis

To analyse the stability of the steady state, we consider the following *ansatz*:

$$A_n(z,t) = \left[\sqrt{P(z)} + \eta_n(z,t)\right] e^{i\phi(z)}, \tag{8.13}$$

where $P(z)$ and $\phi(z)$ denote the power and phase of the steady state, respectively, and $\eta_n(z,t)$ is a perturbation satisfying $|\eta_n(z,t)| \ll \sqrt{P(z)}$.

Substituting Eq. (8.13) into Eqs. (7.21), (8.1), and (8.2), we derive the evolution equations for $\eta_n(z,t)$ as follows:

$$\text{BC}: \quad \eta_{n+1}(0,t) = \rho e^{i[\varphi_0+\phi_n(L)]} h(t) \star \eta_n(L,t), \tag{8.14}$$

$$0 \le z \le L_1: \quad \frac{\partial \eta_n}{\partial z} = \frac{g}{2}\left(1 + \frac{1}{\Omega_g^2}\frac{\partial^2}{\partial t^2}\right)\eta_n - i\frac{\beta_2^{(1)}}{2}\frac{\partial^2 \eta_n}{\partial t^2} + i\gamma^{(1)}P(z)(\eta_n + \eta_n^*), \tag{8.15}$$

$$L_1 < z \le L: \quad \frac{\partial \eta_n}{\partial z} = -i\frac{\beta_2^{(2)}}{2}\frac{\partial^2 \eta_n}{\partial t^2} + i\gamma^{(2)}P(z)(\eta_n + \eta_n^*), \tag{8.16}$$

where we assume the gain is unaffected by the small perturbation, so that $g = \frac{P_{\text{sat}}}{P_{\text{sat}}+r_D P_n(L_1)} g_0$.

Next, we decompose the perturbation into its real and imaginary parts as $\eta_n = a_n + ib_n$, and denote their Fourier transforms by $\hat{a}_n(z,\Omega)$ and $\hat{b}_n(z,\Omega)$, respectively. We then obtain the evolution equation for the vector $(\hat{a}_n, \hat{b}_n)^T$ as follows:

$$\begin{aligned}\text{BC}: \quad & \begin{pmatrix} \hat{a}_{n+1}(0,t) \\ \hat{b}_{n+1}(0,t) \end{pmatrix} = \mathcal{N}_{\text{BC}} \begin{pmatrix} \hat{a}_n(L,t) \\ \hat{b}_n(L,t) \end{pmatrix} \\ & = \rho \begin{pmatrix} \cos[\varphi_0 + \phi_n(L) - \phi_n(0)] & -\sin[\varphi_0 + \phi_n(L) - \phi_n(0)] \\ \sin[\varphi_0 + \phi_n(L) - \phi_n(0)] & \cos[\varphi_0 + \phi_n(L) - \phi_n(0)] \end{pmatrix} \begin{pmatrix} H_+ & -H_- \\ H_- & H_+ \end{pmatrix} \begin{pmatrix} \hat{a}_n(L,t) \\ \hat{b}_n(L,t) \end{pmatrix}\end{aligned} \tag{8.17}$$

$$0 \le z \le L_1: \quad \frac{\partial}{\partial z}\begin{pmatrix} \hat{a}_n \\ \hat{b}_n \end{pmatrix} = M_1 \begin{pmatrix} \hat{a}_n \\ \hat{b}_n \end{pmatrix} = \left[\frac{g}{2}\left(1 - \frac{\Omega^2}{\Omega_g^2}\right) + \begin{pmatrix} 0 & -\frac{\beta_2^{(1)}\Omega^2}{2} \\ \frac{\beta_2^{(1)}\Omega^2}{2} + 2\gamma^{(1)}P(z) & 0 \end{pmatrix}\right] \begin{pmatrix} \hat{a}_n \\ \hat{b}_n \end{pmatrix}, \tag{8.18}$$

$$L_1 < z \le L: \quad \frac{\partial}{\partial z}\begin{pmatrix} \hat{a}_n \\ \hat{b}_n \end{pmatrix} = M_2 \begin{pmatrix} \hat{a}_n \\ \hat{b}_n \end{pmatrix} = \begin{pmatrix} 0 & -\frac{\beta_2^{(2)}\Omega^2}{2} \\ \frac{\beta_2^{(2)}\Omega^2}{2} + 2\gamma^{(2)}P(z) & 0 \end{pmatrix} \begin{pmatrix} \hat{a}_n \\ \hat{b}_n \end{pmatrix}, \tag{8.19}$$

where we introduced the evolution matrices $M_{1,2}$ and the boundary-condition matrix $\mathcal{N}_{\text{BC}}$. Here, H_+ and H_- denote the Fourier transforms of the even and odd components of the

response function $h(t)$, respectively. These can be evaluated using the following formulae:

$$H_+(\Omega) = \int \frac{h(t)+h^*(t)}{2} e^{i\Omega t} dt = \frac{H(\Omega)+H^*(-\Omega)}{2} \tag{8.20a}$$

$$H_-(\Omega) = \int \frac{h(t)-h^*(t)}{2i} e^{i\Omega t} dt = \frac{H(\Omega)-H^*(-\Omega)}{2i}. \tag{8.20b}$$

The perturbations in the same round trip at $z = L$ and at $z = 0$ are related by

$$\begin{pmatrix} \hat{a}_n(L) \\ \hat{b}_n(L) \end{pmatrix} = \mathcal{N}_{\text{evo}} \begin{pmatrix} \hat{a}_n(0) \\ \hat{b}_n(0) \end{pmatrix} = e^{\int_{L_1}^{L} M_2(z)dz} e^{\int_0^{L_1} M_1(z)dz} \begin{pmatrix} \hat{a}_n(0) \\ \hat{b}_n(0) \end{pmatrix}, \tag{8.21}$$

where we have introduced the transformation matrix $\mathcal{N}_{\text{evo}}$, which is induced by the propagation through the EDFA and the fibre over one round trip. We have also adopted an integral approximation, which is valid under the assumption that $M_{1,2}(z)$ do not vary too rapidly along z. Since the two integrals evaluate to $\int_0^{L_1} P(z)dz = P(0)(e^{gL_1}-1)/g = P(L_1)(1-e^{-gL_1})/g$ and $\int_{L_1}^{L} P(z)dz = P(L_1)L_2$, respectively, we obtain

$$\mathcal{N}_{\text{evo}} = e^{\left(1-\frac{\Omega^2}{\Omega_g^2}\right)\frac{gL_1}{2}} \begin{pmatrix} \cos(k_2L_2) & -\frac{\beta_2^{(2)}\Omega^2}{2k_2}\sin(k_2L_2) \\ \frac{2k_2}{\beta_2^{(2)}\Omega^2}\sin(k_2L_2) & \cos(k_2L_2) \end{pmatrix} \begin{pmatrix} \cos(k_1L_1) & -\frac{\beta_2^{(1)}\Omega^2}{2k_1}\sin(k_1L_1) \\ \frac{2k_1}{\beta_2^{(1)}\Omega^2}\sin(k_1L_1) & \cos(k_1L_1) \end{pmatrix}, \tag{8.22}$$

where $k_1 = \sqrt{\frac{\beta_2^{(1)}\Omega^2}{2}\left[\frac{\beta_2^{(1)}\Omega^2}{2} + \frac{2\gamma^{(1)}(1-e^{-gL_1})P(L_1)}{gL_1}\right]}$ and $k_2 = \sqrt{\frac{\beta_2^{(2)}\Omega^2}{2}\left[\frac{\beta_2^{(2)}\Omega^2}{2} + 2\gamma^{(2)}P(L_1)\right]}$, and

$$\mathcal{N}_{\text{BC}} = \rho \begin{pmatrix} \cos(\Delta\varphi) & -\sin(\Delta\varphi) \\ \sin(\Delta\varphi) & \cos(\Delta\varphi) \end{pmatrix} \begin{pmatrix} H_+ & -H_- \\ H_- & H_+ \end{pmatrix}, \tag{8.23}$$

with $\Delta\varphi = \varphi_0 + \gamma^{(1)}\frac{1}{g}(1-e^{-gL_1})P(L_1) + \gamma^{(2)}P(L_1)L_2$. Finally, $\mathcal{N} = \mathcal{N}_{\text{BC}}\mathcal{N}_{\text{evo}}$ governs the evolution of the perturbations over one round trip:

$$\begin{pmatrix} \hat{a}_{n+1}(0,\Omega) \\ \hat{b}_{n+1}(0,\Omega) \end{pmatrix} = \mathcal{N}(\Omega) \begin{pmatrix} \hat{a}_n(0,\Omega) \\ \hat{b}_n(0,\Omega) \end{pmatrix}. \tag{8.24}$$

If we denote the eigenvalues of $\mathcal{N}$ as $\lambda_{1,2}$, the MI gain in decibels per unit length reads

$$g(\Omega) = \frac{20}{L}\log_{10}\max\{|\lambda_1|, |\lambda_2|\}. \tag{8.25}$$

8.4 Analytical and numerical results

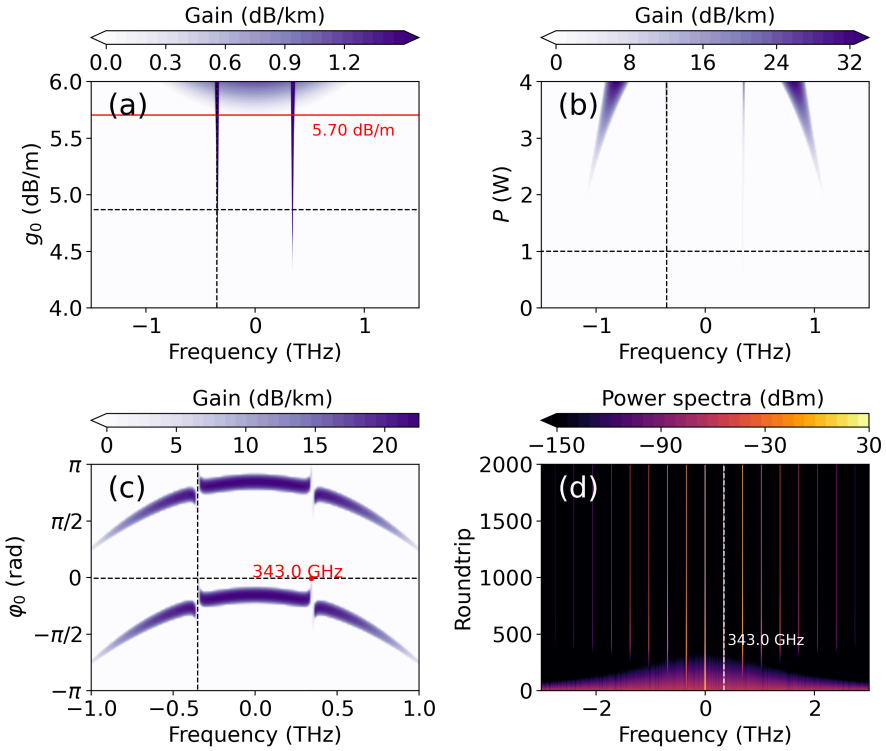

Figure 8.3: MI gain map and simulations via Ikeda map. (a) MI gain vs g_0, the red solid line indicates $\rho e^{\frac{gL_1}{2}} = 1$. (b) MI gain vs intracavity power. (c) MI gain vs linear phase shift φ_0. (d) power spectrum evolution from simulations. Parameters used are $P = 1.0$ W, $\beta_2^{(1)} = -23$ ps^{2}km^{-1}, $\beta_2^{(2)} = 1.2$ ps^{2}km^{-1}, $\Omega_g/(2\pi) = 4$ THz, $\varphi_0' = -0.04$, and others are like Fig. 8.2.

Using Eq. (8.25), we show the dependence of MI gain on various parameters in Fig. 8.3(a)–Fig. 8.3(c). The horizontal dashed line in each figure indicates the parameter used in the other two figures, while the vertical dashed lines denote the filter central frequency. Fig. 8.3(a) shows the evolution of MI gain vs the unsaturated amplifier gain g_0. The setup consistently operates below the lasing threshold, specifically $\rho e^{\frac{gL_1}{2}} < 1$, as indicated by the red line at 5.7 dB/m. We observe two symmetric side lobes appearing on both sides of the pump and close to the filter central frequency, as in passive GTF cavities. Similar lobes also appear in Fig. 8.3(b), which shows the dependence of MI gain on the intracavity power P. In Fig. 8.3(c), the relationship between the MI gain and the linear phase shift φ_0 is presented. It clearly illustrates the influence of the filter on the MI gain, resulting in upward and downward tails around the filter central frequency. The evolution of the spectrum via simulation is shown in Fig. 8.3(d), demonstrating perfect agreement with the theoretical

predictions of Eq. (8.25) regarding the frequency positions of the generated sidebands.

Fig. 8.4 shows the output spectra for different amplifier gain values when the input power is set to 1.0 W. As the amplifier gain increases from 4.57 dB/m to 5.25 dB/m, more sidebands are generated.

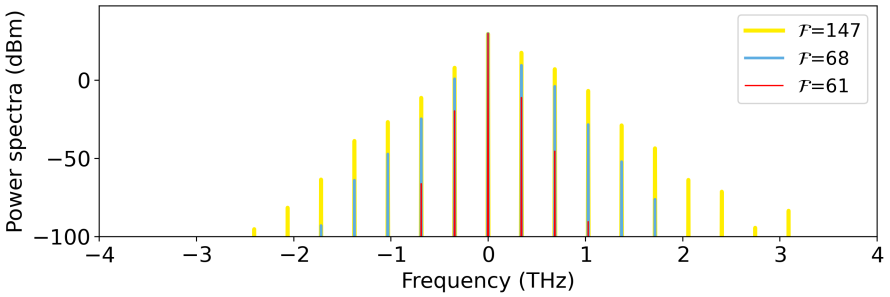

Figure 8.4: Output spectra for various amplifier gain. Power spectrum with effective finesse being (a) $\mathcal{F} = 61$ ($g_0 = 4.55$ dB/m), (b) $\mathcal{F} = 68$ ($g_0 = 4.7$ dB/m), and (c) $\mathcal{F} = 147$ ($g_0 = 5.4$ dB/m). Parameters used are the same as those in Fig. 8.3, except that input power P_{in} is fixed at 1 W.

8.5 Experimental setup

Based on the theoretical results discussed above, our collaborators at Université de Lille designed the experimental setup to test these predictions. The experimental work was carried out primarily by Stefano Negrini at Université de Lille. A schematic of the cavity is shown in Fig. 8.5(b). The main part of the cavity consists of 80 m of DSF with a normal dispersion of $\beta_2^{(2)} = 1.2$ ps^{2}km^{-1}. A 90/10 coupler is used to inject signals into the cavity, while a 99/1 tap coupler is used to extract them. The employed filter is an FBG with a centre wavelength of $\lambda_f = 1547.97$ nm, modeled by the Lorentzian profile in Eqs. 7.20 using parameters $a = 43$ rad/ns and $b = -1.06$. The amplifier, labeled as EDF in the diagram, consists of a $L_2 = 0.33$ m erbium-doped fibre segment, connected to the passive fibre via two wavelength division multiplexers (WDMs). The EDF is pumped by a laser diode (LD pump) at 1490 nm, injected through one of the WDMs. This configuration allows separation between the amplifier pump and the signal wavelengths. The full setup is shown in Fig. 8.5(a). The laser pump is a CW tunable laser with a maximum output power of 44 mW and a linewidth of less than 100 Hz. Its frequency can be rapidly adjusted using an externally controllable piezo actuator, which is used to stabilise the cavity, as detailed below.

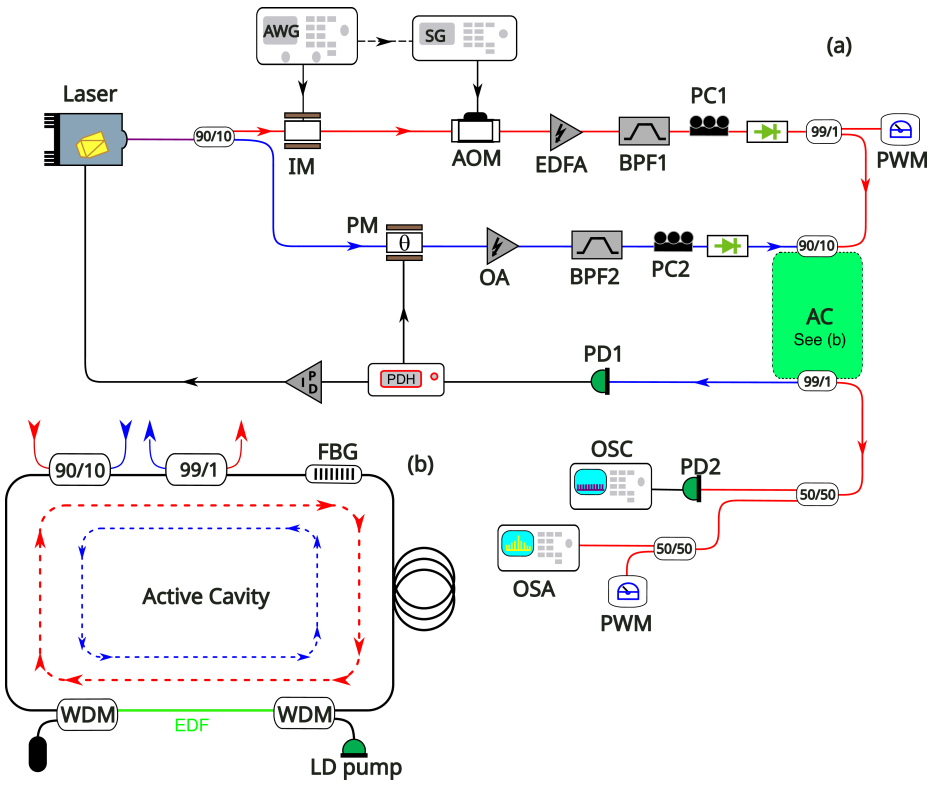

Figure 8.5: Scheme of the experimental setup and cavity. (a) Experimental setup. IM: intensity modulator; AOM: acousto-optic modulator; PM: phase modulator; EDFA: erbium-doped fibre amplifier; OA: optical amplifier; BPF1/2: band-pass filters; PC1/2: polarisation controllers; PDH: Pound-Drever-Hall module; PID: proportional-integral-derivative controller; OSC: oscilloscope; OSA: optical spectrum analyser; PWM: power metres; AC: active cavity. (b) Schematic of the active cavity. LD pump: laser diode pump; WDM: wavelength-division multiplexer; EDF: erbium-doped fibre; FBG: fibre Bragg grating.

The pump is first divided into two parts by a 90/10 coupler, with 90% allocated to the strong driving signal and 10% to the control signal. The two signal paths are indicated in the schematic with red and blue lines, respectively. The driving signal is shaped into a pulse train using an intensity modulator (IM) with a pulse width of $t_D = 1.3$ ns and a repetition rate of $t_R = 451$ ns. This pulse train then passes through an acousto-optic modulator (AOM), introducing a frequency shift of 200 MHz. This shift enables precise control of the cavity detuning by adjusting the pump frequency relative to the nearest cavity resonance. The signal is subsequently amplified by a commercial erbium-doped fibre amplifier (EDFA) and filtered by BPF1 to suppress any residual amplified spontaneous emission from the EDFA. A polarisation controller (PC1) aligns the signal with one of the cavity's polarisation axes, and an optical isolator prevents back reflections from reaching the amplifier. Given the cavity's high sensitivity to external disturbances such as vibrations, noise, and

temperature fluctuations, a feedback control loop is necessary to maintain the driving signal in phase with the intracavity signal. The control system employed in this experiment is based on the well-established Pound-Drever-Hall (PDH) technique [105], which utilises a phase modulator (PM), a PDH controller, and a proportional-integrative-derivative (PID) actuator to stabilise the laser frequency.

As shown by the blue path in Fig. 8.5(a), 10% of the pump signal is modulated by the PM. The modulated signal passes through a chain consisting of an optical amplifier (OA), a filter (BPF2), a polarisation controller (PC2), and an isolator—similar to the driving signal path, but at significantly lower power to avoid stimulated Brillouin scattering. After being injected into the cavity, the signal is retrieved from one of the outputs and converted into an electrical signal (black path) using a photodiode (PD1). This electrical signal is processed by the PDH and PID controllers to generate a correction signal, which is applied directly to the piezo input of the laser pump. This feedback mechanism continuously adjusts the pump frequency, compensating for any disturbances in the intracavity field and maintaining coherence and stability of the entire system.

8.6 Experimental results

In the experiment, we have observed the spontaneous generation of spectral sidebands due to the GTF process in our system. We have explored the impact of the EDFA by recording different spectra as a function of different cavity finesse values obtained by varying the amplifier gain, while carefully maintaining the cavity below the lasing threshold.

Fig. 8.6 presents a comparison of spectra obtained from simulations and experiments for various input powers. The powers are all normalised to the zero mode. A good agreement between the simulations and experimental results is observed in both the sideband power and position, as illustrated in Fig. 8.6(c). Furthermore, an excellent agreement is noted regarding the input power threshold, as demonstrated in Fig. 8.6(a) and Fig. 8.6(b).

In Fig. 8.7, we present the dependency of the input power threshold on the amplifier gain. We observe that the input pump power threshold for sideband generation decreases as the amplifier gain increases. The experimental results show good agreement with the numerical ones, where the MI threshold corresponds to sidebands exceeding a power level of -72.5 dBm/Hz, determined by the noise level. In contrast, the analytical thresholds are

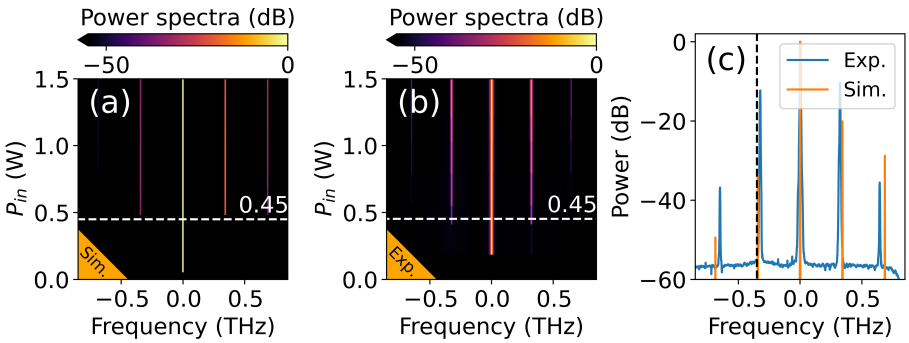

Figure 8.6: Numerical and experimental power spectra. (a) Numerical spectra and (b) experimental spectra vs input pump power with $g_0 = 4.76$ dB/m. The dashed horizontal lines indicate the input power threshold. (c) Comparison of spectra between simulation and experiment for a selected input power power $P_{\text{in}} = 1.36$ W. The dashed vertical lines indicate the filter central frequency. Parameters used are like those in Fig. 8.3.

based on whether the MI gain is greater than 0, without considering the noise level, which results in a lower threshold.

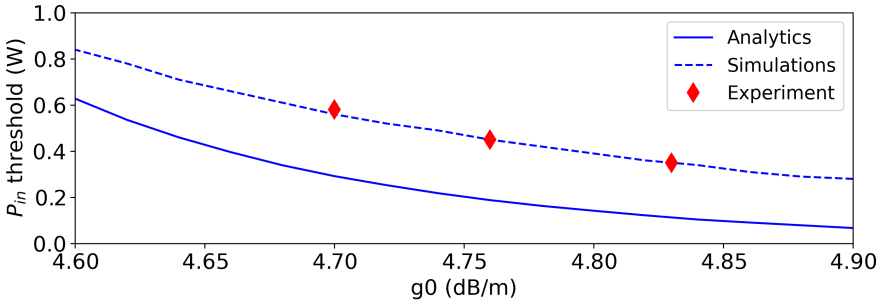

Figure 8.7: Input power threshold vs amplifier gain obtained from analytics, numerics, and experiments. Parameters used are like those in Fig. 8.3.

8.7 Conclusions

By integrating an EDFA into the GTF fibre cavity and precisely adjusting the pump current to maintain the cavity below the lasing threshold, we successfully reduced the total losses, thereby increasing the resonator finesse. Consequently, we observed a decreased power threshold for GTF instability and enhanced energy transfer to spectral sidebands. These findings lay the foundation for advancing the efficiency and spectral bandwidth of GTF-induced OFC sources.

Chapter 9

Optical frequency comb generation in Kerr-quadratic resonators with spectral filtering

---

The work presented in this chapter has been adapted from the following publications:
[5] M. Shi, N. Englebert, F. Leo, D. V. Skryabin, and A. M. Perego. Modulation instability and frequency comb generation in hybrid quadratic-cubic resonators with spectral filter. *Phys. Rev. A*, 112(2):023522, 2025.

9.1 Introduction

Resonators exploiting quadratic nonlinearity have emerged as a promising platform for OFC generation [25, 106, 107, 108, 109]. Unlike Kerr resonators, which rely solely on intrinsic third-order nonlinearities, quadratic resonators enable strong nonlinear interactions at significantly lower power thresholds due to the larger magnitude of second-order susceptibility. In typical implementations, only the fundamental field is resonant within the resonator, while the SH field is not. Despite this, the nonlinear coupling between the two fields—mediated by SHG—can lead to a range of complex dynamics, including MI and OFC generation [25]. A key theoretical insight is that under phase-mismatched conditions, cascaded $\chi^{(2)}$ processes can emulate an effective third-order nonlinearity, producing Kerr-like effects such as self-phase modulation and four-wave mixing [24, 19]. This effective nonlinearity arises from the back-action of the SH field onto the fundamental and can be

engineered in sign and strength depending on the phase-matching configuration. Recent work by Englebert et al. [106] has further demonstrated that stable quadratic soliton combs can form in singly resonant quadratic resonators, where parametric down-conversion drives coherent sech-shaped signal waves. As such, quadratic resonators offer a flexible and efficient platform for realising OFCs with dynamics reminiscent of those in Kerr systems, while retaining the benefits of strong second-order interactions.

In this chapter, we propose a new route to OFC generation in hybrid quadratic–cubic resonators by extending the concept of GTF, as introduced in Section 7.5, to parametrically driven resonators containing a periodically poled fibre (PPF) [110, 111], which is a silica fibre in which an effective second-order nonlinearity is induced by thermal or ultraviolet poling and then periodically modulated along the propagation direction to provide quasi-phase-matching, in direct analogy with PPLN. Although the $\chi^{(2)}$ in PPF is typically much weaker than in lithium niobate, the same coupled-envelope equations describing fundamental and SH fields apply under the slowly varying envelope approximation. Our approach involves integrating an asymmetric spectral filter into a doubly resonant quadratic cavity, allowing control over the phase-matching condition for sideband growth. By exploiting the filter-induced phase shift, we demonstrate analytically and numerically that MI can be initiated even in regimes where traditional phase matching is not satisfied. The resulting MI sidebands are further amplified via cascaded processes, ultimately forming a tunable-repetition-rate OFC. This work builds upon the foundational studies in quadratic resonators and extends the GTF technique to the domain of quadratic nonlinear media.

9.2 Generalised parametrically driven NLSE

Quadratic resonators can be modeled using either coupled-mode theory—especially relevant for integrated platforms [112, 113, 114]—or a mean-field, parametrically driven NLSE, which is commonly employed for fibre cavities [106, 25, 107]. In this work, we consider a ring cavity composed of an SMF, a PPF section, a spectral filter, and input–output couplers, as sketched in Fig. 9.1. In the PPF and SMF, the optical wave envelope propagates according

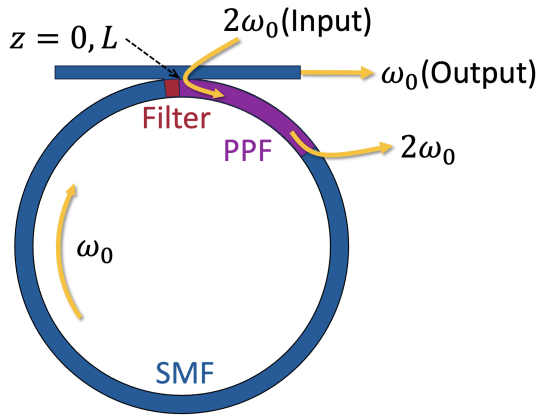

Figure 9.1: Sketch of the setup consisting of a single-mode fibre (SMF), a section of periodically poled fibre (PPF), a spectral filter, and the input and output couplers.

to

$$\frac{\partial A_n}{\partial z} = \left(-\frac{\alpha^{(1)}}{2} - i\frac{\beta_2^{(1)}}{2}\frac{\partial^2}{\partial t^2}\right) A_n + i\kappa B_{\text{in}} A_n^* e^{-i\hat{k}(0)z} + i\kappa^2 A_n^* \left[A_n^2 \star J\right] \tag{9.1}$$

$$\frac{\partial A_n}{\partial z} = \left(-\frac{\alpha^{(2)}}{2} - i\frac{\beta_2^{(2)}}{2}\frac{\partial^2}{\partial t^2} + i\gamma^{(2)}|A_n|^2\right) A_n, \tag{9.2}$$

respectively, where

$$J(z,t) = \frac{1}{2\pi}\int_{-\infty}^{\infty} \frac{1 - e^{-i\hat{k}(\Omega)z}}{\hat{k}(\Omega)} e^{-i\Omega t} \mathrm{d}\Omega, \tag{9.3}$$

$$\hat{k}(\Omega) = -i\frac{\alpha^{(1)}}{2} + \Delta\beta - \Delta\beta_1\Omega - \frac{\beta_{2,B}}{2}\Omega^2. \tag{9.4}$$

$A_n(z,t)$ is the slowly varying envelope of the field at $\omega = \omega_0$, t is the retarded time, z the propagation distance, and n the round trip index. $L_{1,2}$ denotes the lengths of the cavity components, where the index 1 represents the PPF and the index 2 represents the SMF (this convention applies to other variables as well). The total cavity length is denoted by $L = L_1 + L_2$. The coefficient $\beta_2^{(1,2)}$ denots the GVD at ω_0, $\alpha^{(1,2)}$ is the attenuation constants, and κ and $\gamma^{(2)}$ are the second- and third-order nonlinear coefficients. In Eq. (9.1), B_{in} is the pump amplitude at $2\omega_0$ (its phase is set to zero without loss of generality), $\Delta\beta = 2\beta(\omega_0) - \beta(2\omega_0)$ is the phase-mismatch parameter, $\Delta\beta_1 = \beta_1(2\omega_0) - \beta_1(\omega_0)$ the inverse-group-velocity difference, and $\beta_{2,B}$ the GVD at $2\omega_0$—its phase-matching contribution is

negligible compared with $\Delta\beta_1$. In Eq. (9.3), Ω is the offset frequency relative to $2\omega_0$; henceforth, we redefine $\Omega = \omega - \omega_0$ as the offset from ω_0. The quadratic nonlinearity at ω_0 thus acts as a Kerr-like term filtered by J.

It is worth mentioning that Eq. (9.1) is an effective single-field mean-field equation derived from Eqs. (2.5) by assuming that the intracavity field A varies negligibly over a single round trip [25]. This assumption is valid only when the SH field does not remain phase-coherent with the fundamental over long propagation distances. Such a situation occurs in the presence of a large GVM, where temporal walk-off causes rapid dephasing between the fundamental and the SH wave.

Figure 9.2(a) shows the amplitude and phase of $H(\Omega)$ for representative parameters of the spectral filter, which has been introduced in detail in Section 7.5.

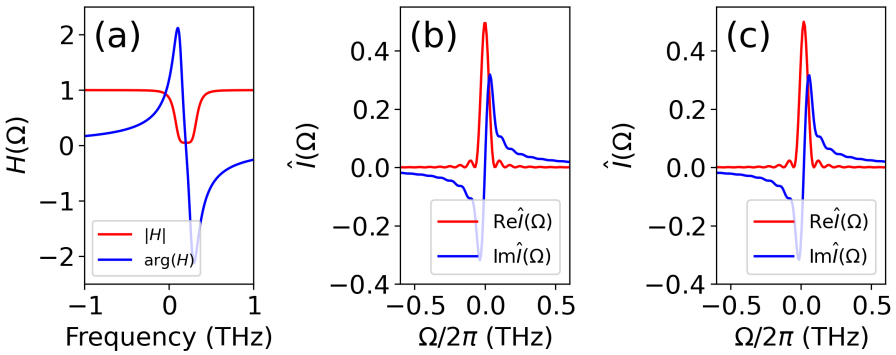

Figure 9.2: (a) Amplitude and phase profiles of $H(\Omega)$. (b), (c) Real and imaginary parts of $\hat{I}(\Omega)$ for $\Delta\beta = 0$ in (b) and $\Delta\beta = 46.5$ m^{-1} in (c). Filter parameters: $a = 0.6$ rad/ps, $b = -3$, and $\Omega_f/(2\pi) = 0.2$ THz. PPF parameters: $\alpha^{(1)} = 0.069$ km^{-1} (0.3 dB/km), $\Delta\beta_1 = 350$ ps/m, $\beta_{2,B} = 10$ ps^2/km, and $L_1 = 4$ cm.

The general BCs for the envelope $A_n(z,t)$ read

$$A_{n+1}(0,t) = \rho e^{i\varphi_0} A_n(L,t) + \theta e^{i\varphi_T}\sqrt{P_{\text{in}}}, \tag{9.5}$$

where ρ^2 and θ^2 are the power reflection and transmission coefficients of the coupler, respectively. Here P_{in} is the power and φ_T the initial phase of the injected wave at ω_0, while φ_0 is the linear phase accumulated over one round trip, modulo 2π. In this work we set $P_{\text{in}} = 0$; pump injection can be incorporated straightforwardly when exploring more complex scenarios.

Defining $Z = z + nL$, $\alpha_T = -\ln\rho + \frac{1}{2}(\alpha^{(1)}L_1 + \alpha^{(2)}L_2)$, $\beta_2 = [\beta_2^{(1)}L_1 + \beta_2^{(2)}L_2]/L$, and $\gamma = \gamma^{(2)}L_2/L$, we obtain the generalised, parametrically driven NLSE with spectral

filtering:

$$\begin{aligned} L\frac{\partial A}{\partial Z} =& (-\alpha_T + i\varphi_0)A + (\Phi + i\Psi) \star A \\ &+ \left(-i\frac{\beta_2}{2}L\frac{\partial^2}{\partial t^2} + i\gamma L|A|^2\right) A \\ &+ i\kappa L_{\text{eff}} B_{\text{in}} A^* - (\kappa L_1)^2 \left(I \star A^2\right) A^*, \end{aligned} \tag{9.6}$$

with

$$I(t) = \int_0^{L_1} J(z,t)\, dz = \frac{1}{2\pi}\int_{-\infty}^{\infty} \hat{I}(\Omega) e^{-i\Omega t}\, d\Omega, \tag{9.7a}$$

$$L_{\text{eff}} = \int_0^{L_1} e^{-i\hat{k}(0)z'}\, dz' = L_1 e^{-i\hat{k}(0)L_1/2} \operatorname{sinc}\left[\frac{\hat{k}(0)L_1}{2}\right], \tag{9.7b}$$

where $\hat{I}(\Omega) = \left[1 - i\hat{k}(\Omega)L_1 - e^{-i\hat{k}(\Omega)L_1}\right] / \left[\hat{k}^2(\Omega)L_1^2\right]$ [25]. The profiles of $\hat{I}(\Omega)$ for $\Delta\beta = 0$ and $\Delta\beta \neq 0$ are plotted in Figs. 9.2(b) and 9.2(c). Further discussion of $\hat{I}(\Omega)$ is provided in Section 9.4. We emphasise that the cavity is driven by the $\chi^{(2)}$ response of the PPF at ω_0, while the pump at $2\omega_0$ is non-resonant and circulates only within the PPF section.

9.3 Stationary solutions

We assume a CW solution of Eq. (9.6) in the form $A(Z,t) = \sqrt{P}\, e^{i\xi}$, where P and ξ are the power and phase, respectively. Substituting into Eq. (9.6) yields the trivial solution $P = 0$ and a non-trivial branch ($P \neq 0$). The power and phase of the non-trivial solution satisfy the implicit system

$$\begin{aligned} &\left|-\alpha_T + i\varphi_0 + F(0) + i\psi(0) + P\left[i\gamma L - (\kappa L_1)^2 \hat{I}(0)\right]\right|^2 \\ =& |\kappa L_{\text{eff}} B_{\text{in}}|^2, \end{aligned} \tag{9.8a}$$

$$\frac{-\alpha_T + i\varphi_0 + F(0) + i\psi(0) + P\left[i\gamma L - (\kappa L_1)^2 \hat{I}(0)\right]}{-i\kappa L_{\text{eff}} B_{\text{in}}} = e^{-i2\xi}. \tag{9.8b}$$

Figure 9.3(a) and Fig. 9.3(b) plot the intracavity power P vs the input pump power $P_B = |B_{\text{in}}|^2$ (solid lines) for fixed $\varphi_0' = \varphi_0 + \psi(0) = 0$ and -1, respectively; dashed lines show the cavity response without the filter. A non-zero phase mismatch $\Delta\beta$ raises the input-power threshold required for a non-trivial CW. Figure 9.3(c) summarises how this threshold grows

with the mismatch $\Delta\beta$.

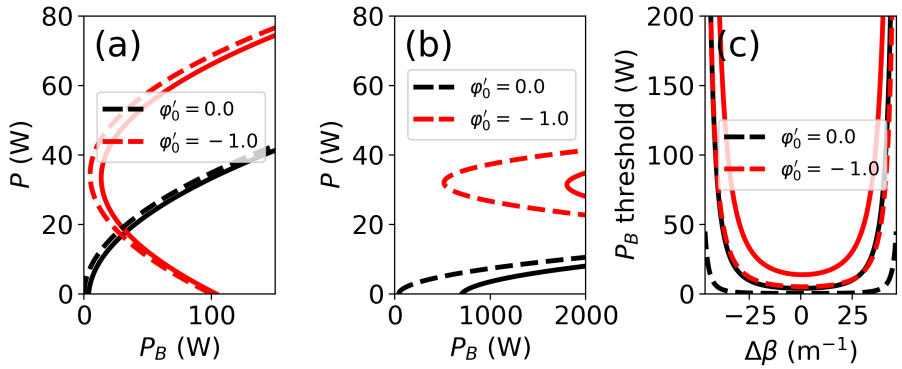

Figure 9.3: (a),(b) Intracavity power P vs input power P_B for non-trivial CWs with (solid) and without (dashed) the filter: (a) $\Delta\beta = 0$, (b) $\Delta\beta = 46.5$ m^{-1}. (c) Minimum input power required for positive P vs $\Delta\beta$. Parameters: $a = 0.6$ rad/ps, $b = -3$, $\Omega_f/(2\pi) = 0.2$ THz, $\alpha^{(1)} = 0.069$ km^{-1} (0.3 dB/km), $\Delta\beta_1 = 350$ ps/m, $\beta_{2,B} = 10$ ps^2/km, $L_1 = 4$ cm, $\kappa = 2.5$ m^{-1}W$^{-1/2}$, $\gamma = 1.4$ W^{-1}km^{-1}, $\alpha_T = 5\%$, and $L = 20$ m.

9.4 MI analysis

We analyse the MI of the intracavity CW solution starting from Eq. (9.6). Introduce a weak perturbation $\eta(Z,t)$, with $|\eta|^2 \ll P$, such that

$$A(Z,t) = \sqrt{P}\, e^{i\xi} + \eta(Z,t). \tag{9.9}$$

Substituting Eq. (9.9) into Eq. (9.6) and retaining only terms linear in η, we obtain

$$\begin{aligned} L\frac{\partial \eta}{\partial Z} =& \Big[-\alpha_T + i\varphi_0 - i\tfrac{\beta_2}{2} L \tfrac{\partial^2}{\partial t^2} + i2\gamma PL\Big]\eta + (\Phi + i\Psi) \star \eta \\ &+ \Big(i\gamma PL e^{2i\xi} + i\kappa L_{\text{eff}} B_{\text{in}} - (\kappa L_1)^2 \hat{I}(0) P e^{2i\xi}\Big)\eta^* \\ &- (\kappa L_1)^2 2P\big(I \star \eta\big). \end{aligned} \tag{9.10}$$

Fourier transforming Eq. (9.10) gives

$$L\frac{\partial}{\partial Z}\begin{pmatrix} \hat{\eta}(Z,\Omega) \\ \hat{\eta}^*(Z,-\Omega) \end{pmatrix} = M \begin{pmatrix} \hat{\eta}(Z,\Omega) \\ \hat{\eta}^*(Z,-\Omega) \end{pmatrix}, \tag{9.11}$$

with

$$M = \begin{pmatrix} d & 0 \\ 0 & d \end{pmatrix} + \begin{pmatrix} S & C \\ C^* & -S \end{pmatrix}, \tag{9.12a}$$

$$d(\Omega) = -\alpha_T + F_e(\Omega) + i\psi_o(\Omega) - (\kappa L_1)^2 2P\hat{I}_+(\Omega), \tag{9.12b}$$

$$S(\Omega) = i\varphi_0 + F_o(\Omega) + i\psi_e(\Omega) + i\tfrac{\beta_2}{2}L\Omega^2 + i2\gamma PL - (\kappa L_1)^2 2P\hat{I}_-(\Omega), \tag{9.12c}$$

$$C = i\gamma PLe^{2i\xi} + i\kappa L_{\text{eff}}B_{\text{in}} - (\kappa L_1)^2\hat{I}(0)Pe^{2i\xi}, \tag{9.12d}$$

where even/odd decompositions are $F_{e,o} = (F \pm F(-\Omega))/2$ and similarly for ψ, while $\hat{I}_\pm = (\hat{I} \pm \hat{I}^*(-\Omega))/2$. The eigenvalues of M are $\lambda_\pm = d \pm \sqrt{S^2 + |C|^2}$, giving the power gain

$$g(\Omega) = \frac{2}{L}\left\{-\alpha_T + F_e(\Omega) - (\kappa L_1)^2 2P\,\mathrm{Re}\big[\hat{I}_+(\Omega)\big] + \mathrm{Re}\sqrt{S^2 + |C|^2}\right\}. \tag{9.13}$$

From Figs. 9.2(b) and 9.2(c), we note that $\mathrm{Re}\,\hat{I}(\Omega)$ is nearly even, while $\mathrm{Im}\,\hat{I}(\Omega)$ is nearly odd, so $\hat{I}_-$ is negligible. Thus $\hat{I}$ mainly affects the gain via $\mathrm{Re}[\hat{I}_+(\Omega)]$, which suppresses gain near the carrier without altering the sidebands.

9.5 MI gain and OFC generation for nontrivial CWs

We first focus on the non-trivial CW solutions and examine their MI gain and OFC generation. To highlight the impact of the filter, we present analytical gain spectra vs φ_0 in Fig. 9.4(a) and Fig. 9.4(b), comparing cases with and without the filter. It is clear that the filter enables MI for parameter values that would otherwise be stable, specifically around $\varphi_0' = 0$ (i.e., $\varphi_0 = -\psi(0)$). The dependence of the MI gain on the phase-mismatch parameter $\Delta\beta$ and the GVM parameter $\Delta\beta_1$ is shown in Fig. 9.4(c) and Fig. 9.4(d), respectively. While $\Delta\beta$ has little influence, a vanishing $\Delta\beta_1$ suppresses MI gain. Indeed, a vanishing real part of $\hat{k}(0)$ suppresses the effective third-order nonlinearity. Moreover, Fig. 9.5 and Fig. 9.6 display analytical gain maps vs filter bandwidth, depth, and centre frequency, as well as dispersion, quadratic and Kerr nonlinearities, and intracavity power. Notably, the MI gain disappears and then reappears as κ increases [Fig. 9.6(b)]. This behaviour occurs because the intracavity power first drops below the MI threshold (31 W) and then exceeds it again as κ grows. Filter-induced sideband gain persists even without fibre Kerr nonlinearity, as

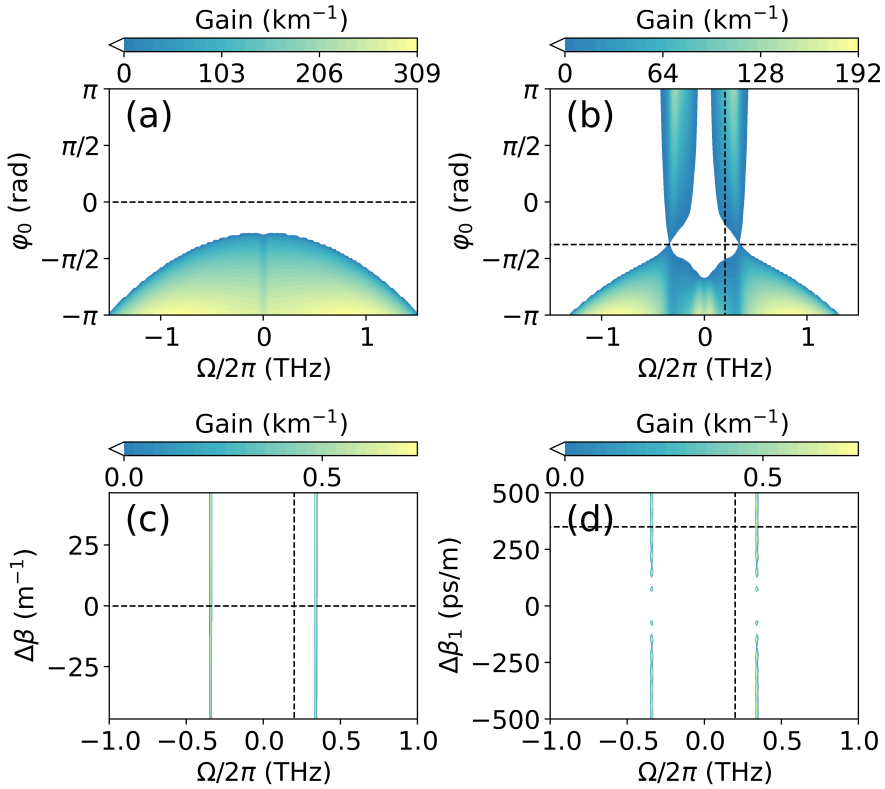

Figure 9.4: (a),(b) MI gain vs φ_0 without (a) and with (b) filtering. (c) MI gain vs $\Delta\beta$; (d) MI gain vs $\Delta\beta_1$, both with the filter present. Parameters: $P = 31$ W, $\beta_2 = 5$ ps^{2}km^{-1}, $\kappa = 2.5$ m^{-1}W$^{-1/2}$, $\gamma = 1.4$ W^{-1}km^{-1}, $\alpha_T = 5\%$, $L = 20$ m, $L_1 = 4$ cm, $\alpha^{(1)} = 0.069$ km^{-1} (0.3 dB/km), $\Delta\beta = 0$, $\Delta\beta_1 = 350$ ps/m, $\beta_{2,B} = 10$ ps^2/km, $a = 0.6$ rad/ps, $b = -3$, $\Omega_f/(2\pi) = 0.2$ THz, and $\varphi_0 = -\psi(0)$. Dashed horizontal lines mark the parameter values used in other panels; dashed vertical lines mark the filter central frequency.

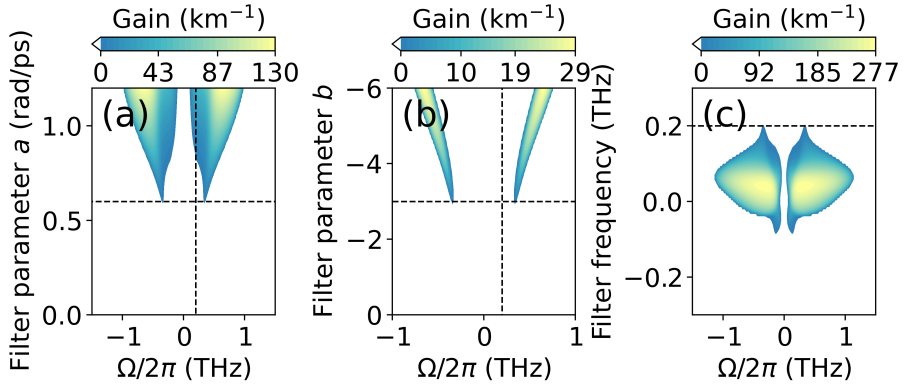

Figure 9.5: Analytical MI gain with filtering vs (a) filter bandwidth a, (b) filter depth b, and (c) filter central frequency $\omega_f/2\pi$. Parameters are as in Fig. 9.4. Dashed horizontal and vertical lines indicate parameter values and the filter centre, respectively.

seen in Fig. 9.6(d) in the limit $\gamma \to 0$, emphasising that MI survives when quadratic nonlinearity in the PPF dominates. While in our model the Kerr term arises from the nonlinear

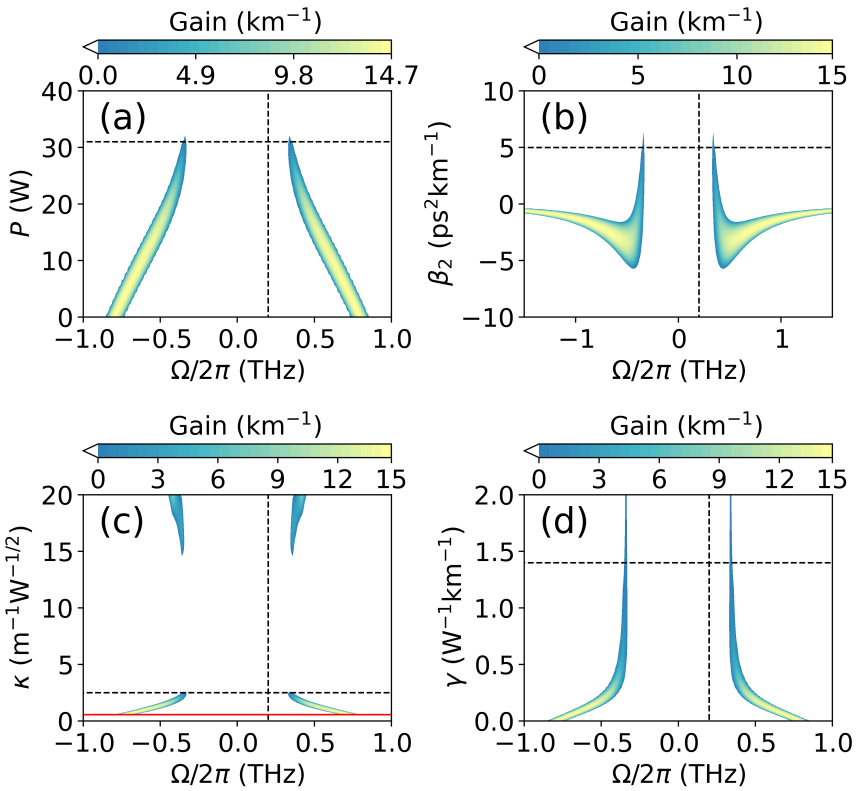

Figure 9.6: Analytical MI gain with filtering vs (a) intracavity power P, (b) dispersion β_2, (c) quadratic nonlinearity κ at fixed input power $P_B = 88$ W (red line marks the minimum κ for a CW), and (d) cubic nonlinearity γ at $P_B = 88$ W. Other parameters are as in Fig. 9.4.

SMF [106], the dominant nonlinearity in practice will depend on the specific experimental setup.

To validate the theory and explore the nonlinear stage of MI, we solved Eq. (9.6) numerically using a split-step Fourier method. Figures 9.7(a) and 9.7(c) confirm that the analytically predicted maximally unstable frequency matches the simulations. In the nonlinear regime, a stable roll pattern forms [Fig. 9.7(b)]; its spectrum is an OFC whose line spacing equals the offset of the maximally unstable sideband, as shown in Figs. 9.7(c) and 9.7(d). Because the MI-gain position can be tuned by adjusting the detuning between ω_0 and the filter frequency [Fig. 9.5(b)], the scheme enables OFC generation with a tunable repetition rate. Close to the MI threshold, stable rolls appear; for much larger gain, the nonlinear stage produces chaotic combs.

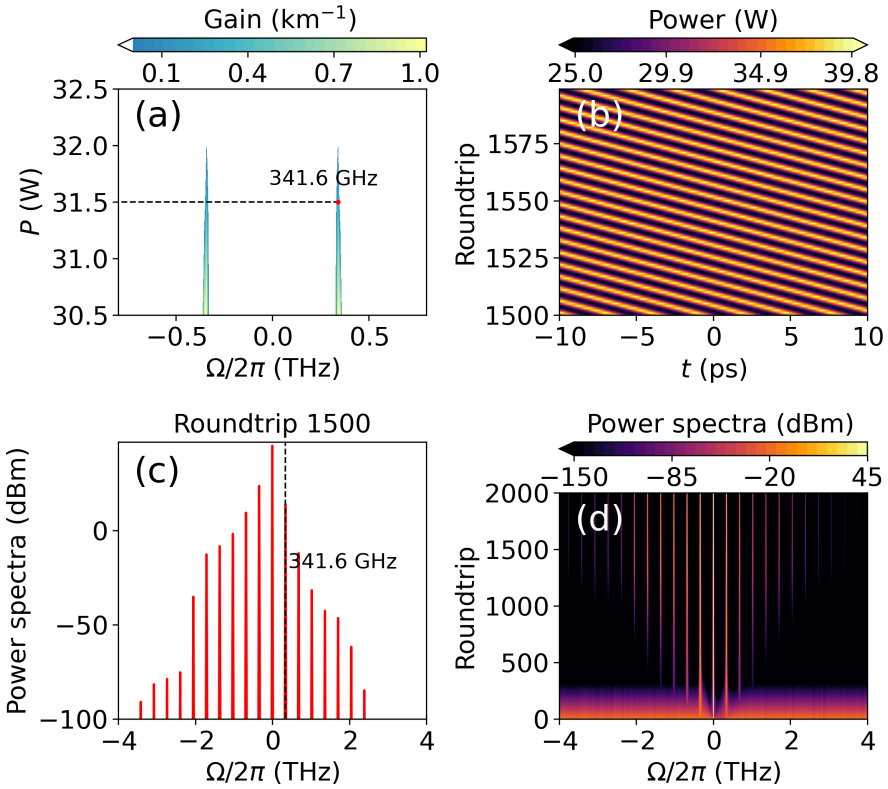

Figure 9.7: Numerical simulation results. (a) Analytical MI gain map with filtering vs intracavity power P; the frequency of maximum gain at $P = 31.5$ W is marked. (b) Field-power evolution between the 1500th and 1600th round trips; the initial condition is the steady state plus 1 mW of broadband noise. (c) Power spectrum at the 1500th round trip. (d) Power-spectrum evolution up to the 4000th round trip. Parameters are as in Fig. 9.4.

9.6 MI gain and OFC generation for trivial CWs

As noted in Section 9.3, non-trivial CW solutions exist only above a certain input-power threshold. We therefore examine the MI of trivial CWs below that threshold. Figure 9.8(a) shows that introducing the filter (increasing its strength from zero) produces new MI sidebands. Figure 9.8(b) confirms once again the possibility of OFC generation with a tunable repetition rate. The MI gain vs input power P_B is plotted in Fig. 9.8(c). The trivial solution becomes unstable to zero-mode perturbations above the power marked by the yellow dashed line; beyond this point, only non-trivial solutions remain 0-mode stable. At $P_B = 0.5$ W the peak gain occurs at $\Omega/2\pi = 490.1$ GHz, in perfect agreement with the simulated spectrum of Fig. 9.8(d), where a sparse OFC is generated.

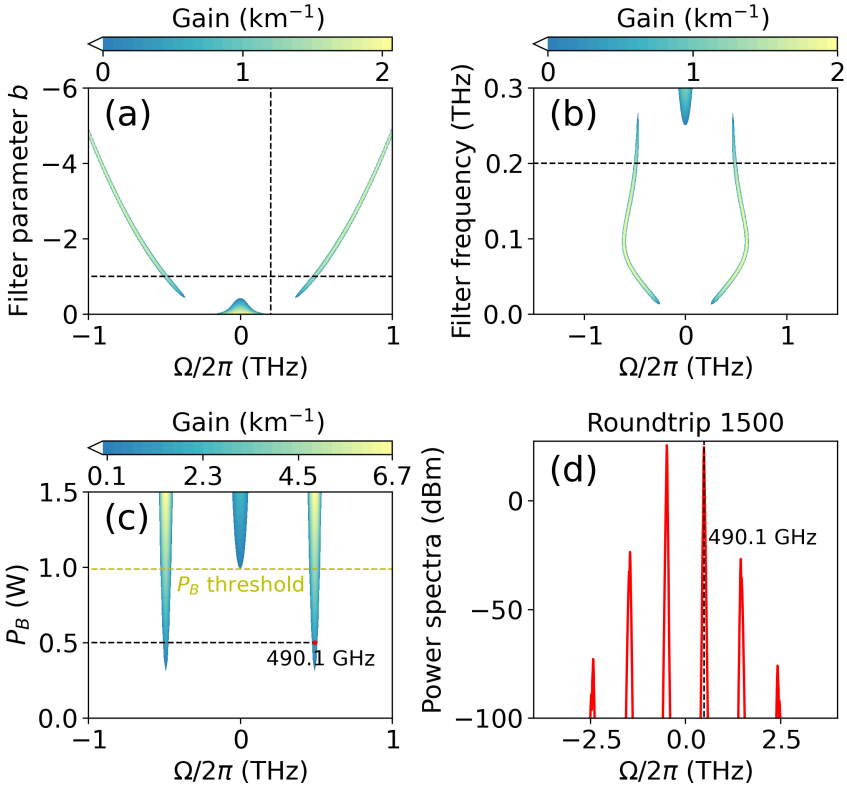

Figure 9.8: (a),(b) MI-gain maps vs filter strength (a) and filter central frequency (b). Dashed horizontal lines mark the chosen parameters, and the vertical line in (a) marks the filter centre. (c) MI gain vs input power P_B; the frequency of maximum gain at $P_B = 0.5$ W is indicated. The yellow dashed line is the input-power threshold for a positive non-trivial intracavity power P—also the stability limit of the trivial solution. (d) Power spectrum at the 1500th round trip. Parameters: $P_B = 0.5$ W, $\beta_2 = 5$ ps^{2}km^{-1}, $\kappa = 2.5$ m^{-1}W$^{-1/2}$, $\gamma = 1.4$ W^{-1}km^{-1}, $\alpha_T = 5\%$, $L = 20$ m, $L_1 = 4$ cm, $\alpha^{(1)} = 0.069$ km^{-1} (0.3 dB/km), $\Delta\beta = 0$, $\Delta\beta_1 = 350$ ps/m, $\beta_{2,B} = 10$ ps^2/km, $a = 0.6$ rad/ps, $b = -1$, $\Omega_f/(2\pi) = 0.2$ THz, and $\varphi_0 = -\psi(0)$.

9.7 Conclusions

We have presented analytical and numerical results on filter-induced MI in hybrid quadratic–cubic resonators, driven by asymmetric spectral losses between signal and idler. Analytical expressions for the parametric gain, covering a broad parameter range, agree excellently with numerical simulations. We further showed that the gain-through-filtering mechanism enables tunable optical-frequency-comb generation in quadratic–cubic resonators. The large GVM is not a fundamental requirement for MI in $\chi^{(2)}$ systems. Indeed, MI has been demonstrated both in conservative SHG and in intracavity $\chi^{(2)}$ configurations even in the absence of strong walk-off [115, 116]. We expect that the filter-induced MI could also be found in more general models for $\chi^{(2)}$ media, and this will be the subject of future investigations.

Chapter 10

Period-4 modulation instability in ring fibre cavities

The work presented in this chapter has been adapted from the following publications:
[4] M. Shi, M. Conforti, A. Mussot, and A. M. Perego. Period-4 modulation instability in ring fiber cavities. *Phys. Rev. A*, 111(1):013513, 2025.

10.1 Introduction

As discussed in Section 7.2, MI in ring fibre cavities can exhibit P1 or P2 modulation patterns. Spectral sidebands associated with P2 MI were observed experimentally in 1997 [100]. However, direct observation of the temporal dynamics of P2 MI has remained elusive for a long time due to the fast oscillation frequencies—in the THz range—and it has only recently been observed through time-domain, round trip-resolved measurements enabled by a time lens [117].

While P2 patterns are observable for stationary CW solutions, Haelterman described period-doubled CW solutions for a driven fibre cavity both analytically and numerically in the 1990s [118, 119, 120]. These solutions consist of two distinct CW power levels that alternate periodically between consecutive cavity round trips. In this chapter, we analyse the MI of period-doubled CW solutions in a passive ring fibre cavity and predicts the existence of a P4 temporal pattern, which repeats itself every four cavity round trips. We model the evolution of disturbances to the period-doubled CW solution by means of two coupled Ikeda maps, which allow us to compute CW solutions, perform a Floquet linear

stability analysis, and carry out full numerical simulations of the system dynamics. Our findings reveal that, under realistic conditions, there exists a configuration in which the period-doubled CW solutions are stable against 0-mode perturbations but modulationally unstable against perturbations oscillating at other frequencies, thereby enabling observation of P4 dynamics.

10.2 Period-doubled CW solutions

Based on the findings detailed in Ref. [118], the period-doubled CW solutions of Eqs. (7.1) can be derived. If we denote the CW envelopes in two consecutive round trips by $X(z)$ and $Y(z)$, respectively, the BCs [Eq. (7.1b)] give

$$Y(0) = \rho e^{i(\varphi_0+\gamma P_X L)} X(0) + \theta\sqrt{P_{\text{in}}}, \tag{10.1a}$$

$$X(0) = \rho e^{i(\varphi_0+\gamma P_Y L)} Y(0) + \theta\sqrt{P_{\text{in}}}, \tag{10.1b}$$

where $P_X = |X(0)|^2$ and $P_Y = |Y(0)|^2$. Eliminating $\theta\sqrt{P_{\text{in}}}$, one finds

$$\left[1 + \rho e^{i(\varphi_0+\gamma P_X L)}\right] X(0) = \left[1 + \rho e^{i(\varphi_0+\gamma P_Y L)}\right] Y(0). \tag{10.2}$$

The relationship between the two intracavity powers can be obtained by taking the modulus squared of both sides of Eq. (10.2):

$$P_Y = \frac{1 + \rho^2 + 2\rho\cos(\varphi_0 + \gamma P_X L)}{1 + \rho^2 + 2\rho\cos(\varphi_0 + \gamma P_Y L)} P_X. \tag{10.3}$$

Additionally, substituting Eq. (10.1a) into Eq. (10.2) yields the relationship between the input power P_{in} and the intracavity powers P_X and P_Y as follows:

$$\theta^2 P_{\text{in}} = \frac{1 + \rho^4 - 2\rho^2\cos[2\varphi_0 + \gamma(P_X + P_Y)L]}{1 + \rho^2 + 2\rho\cos(\varphi_0 + \gamma P_Y L)} P_X. \tag{10.4}$$

To obtain the relationship between the input and output powers, we first solved for P_Y implicitly from Eq. (10.3) for each value of P_X using the bisection method, and then substituted both P_X and P_Y into Eq. (10.4) to derive P_{in}. The resulting solutions are shown in Fig. 10.1(a). Since P_X and P_Y represent the intracavity powers of two consecutive round trips, the solutions for P_X inherently also apply to P_Y. Without loss of generality, we select

P_X to represent the intracavity powers in the demonstration. In Fig. 10.1(a), we observe not only the typical S-shaped curve (black and gray), which is characteristic of Eqs. (10.3) and (10.4), but also the emergence of new solutions—period-doubled CW solutions (red and pink). To determine how the intracavity power depends on each value of φ_0, we first implicitly obtained the relationship between P_X and P_Y from both Eqs. (10.3) and (10.4) using the bisection method within a specific range of P_Y ($0 < P_Y < 5.5$ W in our case), and then calculated the intersections of the two curves to determine P_X. The results are shown in Fig. 10.1(b).

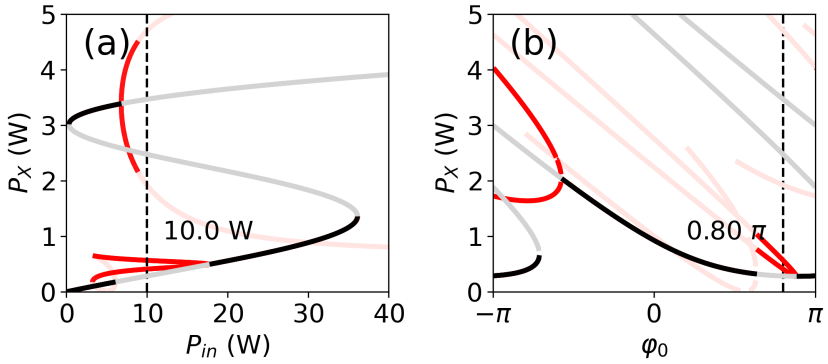

Figure 10.1: Period-doubled vs stationary CW solutions. (a) Intracavity power vs input pump power P_{in} with fixed $\varphi_0 = 0.8\pi$. (b) Intracavity power vs φ_0 with fixed $P_{\text{in}} = 10$ W. Black (gray) curves represent the stationary CW solutions which are stable (unstable) with respect to the 0-mode perturbations, whereas red (pink) curves represent the period-doubled CW solutions which are stable (unstable) with respect to the 0-mode perturbations. Parameters used are $\gamma = 2.5\ \text{W}^{-1}\text{km}^{-1}$, $\rho = \sqrt{0.8}$, $\theta = \sqrt{0.1}$, $L = 0.5$ km, and $\beta_2 = 0.4\ \text{ps}^2/\text{km}$. The two dashed lines indicate the parameters used in other panels.

Before focusing on the study of MI in period-doubled CW solutions, it is worth emphasising that for effective energy transfer from the pump to the sidebands via the four-wave mixing process, the CW solution must be stable against 0-mode perturbations. Figure 10.1 illustrates a scenario characterised by considerable parameter flexibility around the dashed lines, in which the lower-energy stationary CW solutions exhibit instability while the period-doubled CW solutions remain stable against 0-mode perturbations, rendering the latter the lowest-energy stable CW solutions.

10.3 Modulation instability of period-doubled CW solutions

To investigate the MI of a period-doubled CW solution, we introduce small frequency-dependent perturbations $\eta_n(z,t)$ to the CW fields described by Eq. (10.4), with $|\eta_n| \ll \sqrt{P_{X,Y}}$. Without loss of generality, we assume the intracavity power is P_X during the $2n$th round trip and P_Y during the $(2n+1)$th round trip, that is,

$$A_{2n,2n+1}(z,t) = \left[\sqrt{P_{X,Y}} + \eta_{2n,2n+1}(z,t)\right] e^{i\phi_{X,Y}(z)}, \tag{10.5}$$

where $\phi_{X,Y}(z) = \phi_{X,Y}(0) + \gamma P_{X,Y} z$ are the phases of the CW solutions. Substituting Eq. (10.5) into Eq. (7.1a) yields the evolution equations for the perturbations along the cavity,

$$\frac{\partial \eta_{2n,2n+1}}{\partial z} = -i\frac{\beta_2}{2}\frac{\partial^2 \eta_{2n,2n+1}}{\partial t^2} + i\gamma P_{X,Y}\left(\eta_{2n,2n+1} + \eta^*_{2n,2n+1}\right), \tag{10.6}$$

which, in the frequency domain, read

$$\frac{\partial}{\partial z}\begin{pmatrix} \hat{\eta}_{2n,2n+1}(z,\omega) \\ \hat{\eta}^*_{2n,2n+1}(z,-\omega) \end{pmatrix} = M^{\text{evo}}_{e,o}\begin{pmatrix} \hat{\eta}_{2n,2n+1}(z,\omega) \\ \hat{\eta}^*_{2n,2n+1}(z,-\omega) \end{pmatrix}. \tag{10.7}$$

Here, the evolution matrices for even (e) and odd (o) round trips are

$$M^{\text{evo}}_{e,o} = \begin{pmatrix} i\kappa_{X,Y} & i\gamma P_{X,Y} \\ -i\gamma P_{X,Y} & -i\kappa_{X,Y} \end{pmatrix}, \tag{10.8}$$

with $\kappa_{X,Y}(\omega) = \frac{\beta_2}{2}\omega^2 + \gamma P_{X,Y}$. Equations (10.7) admit exact solutions that relate the perturbations at $z = 0$ and $z = L$,

$$\begin{pmatrix} \hat{\eta}_{2n,2n+1}(L,\omega) \\ \hat{\eta}^*_{2n,2n+1}(L,-\omega) \end{pmatrix} = N^{\text{evo}}_{e,o}\begin{pmatrix} \hat{\eta}_{2n,2n+1}(0,\omega) \\ \hat{\eta}^*_{2n,2n+1}(0,-\omega) \end{pmatrix}, \tag{10.9}$$

where $N^{\text{evo}}_{e,o} = e^{LM^{\text{evo}}_{e,o}}$. Its rows are $\left(\cosh(q_{X,Y}L) + i\kappa_{X,Y}L\frac{\sinh(q_{X,Y}L)}{q_{X,Y}L},\ i\gamma P_{X,Y}L\frac{\sinh(q_{X,Y}L)}{q_{X,Y}L}\right)$ and $\left(-i\gamma P_{X,Y}L\frac{\sinh(q_{X,Y}L)}{q_{X,Y}L},\ \cosh(q_{X,Y}L) - i\kappa_{X,Y}L\frac{\sinh(q_{X,Y}L)}{q_{X,Y}L}\right)$, with $q_{X,Y}(\omega) = \sqrt{(\gamma P_{X,Y})^2 - \kappa^2_{X,Y}(\omega)}$ being the eigenvalues of $M^{\text{evo}}_{e,o}$.

On the other hand, the BCs for the perturbations follow from Eq. (7.1b) and read

$$\eta_{2n+1,2n+2}(0,t) = \rho e^{i(\varphi_0 + \gamma P_{X,Y}L \mp \phi_{YX})}\eta_{2n,2n+1}(L,t), \tag{10.10}$$

where $\phi_{YX} = \phi_Y(0) - \phi_X(0)$. The Fourier counterparts of Eqs. (10.10) read

$$\begin{pmatrix} \hat{\eta}_{2n+1,2n+2}(0,\omega) \\ \hat{\eta}^*_{2n+1,2n+2}(0,-\omega) \end{pmatrix} = N^{\mathrm{BC}}_{e,o} \begin{pmatrix} \hat{\eta}_{2n,2n+1}(L,\omega) \\ \hat{\eta}^*_{2n,2n+1}(L,-\omega) \end{pmatrix}. \tag{10.11}$$

Here, $N^{\mathrm{BC}}_{e,o}$ represents the boundary-condition matrices that link the fields at even or odd round trips to those of the subsequent round trips and reads

$$N^{\mathrm{BC}}_{e,o} = \begin{pmatrix} \rho e^{i\left(\varphi_0 + \gamma P_{X,Y} L \mp \phi_{YX}\right)} & 0 \\ 0 & \rho e^{-i\left(\varphi_0 + \gamma P_{X,Y} L \mp \phi_{YX}\right)} \end{pmatrix}. \tag{10.12}$$

Finally, we relate the perturbation spectral amplitudes between two consecutive round trips through

$$\begin{pmatrix} \hat{\eta}_{2n+2}(0,\omega) \\ \hat{\eta}^*_{2n+2}(0,-\omega) \end{pmatrix} = N \begin{pmatrix} \hat{\eta}_{2n}(0,\omega) \\ \hat{\eta}^*_{2n}(0,-\omega) \end{pmatrix}, \tag{10.13}$$

where we define $N = N^{\mathrm{BC}}_o N^{\mathrm{evo}}_o N^{\mathrm{BC}}_e N^{\mathrm{evo}}_e$. If Λ denotes the eigenvalue of N with the largest modulus, the perturbation gain in decibels per unit length is

$$g_{\mathrm{dB}} = \frac{10}{L} \log_{10} |\Lambda|. \tag{10.14}$$

The phase-matching condition in this case generalises Eq. (7.12)—taking into account the total phase shift accumulated over $2L$ and replacing P with the sum of the powers in two consecutive round trips, $P_X + P_Y$—and is expressed as

$$\beta_2 \omega^2 L + 2\varphi_0 + 2\gamma(P_X + P_Y)L = K\pi, \tag{10.15}$$

with $K = 0, \pm 1, \pm 2, \ldots$. Equation (10.15) generally provides a good quantitative prediction near the MI threshold.

In Figs. 10.2(a) and 10.2(b), we show the MI gain as a function of the phase shift φ_0 for a fixed average power $(P_X + P_Y)/2$. The blue regions correspond to MI of stationary CW solutions ($P_X = P_Y$), whereas the cyan regions correspond to MI of period-doubled CW solutions ($P_X \neq P_Y$). The period of MI for stationary CW solutions can be identified using the rules outlined in Section 7.2. Extending these rules to period-doubled CW solutions is

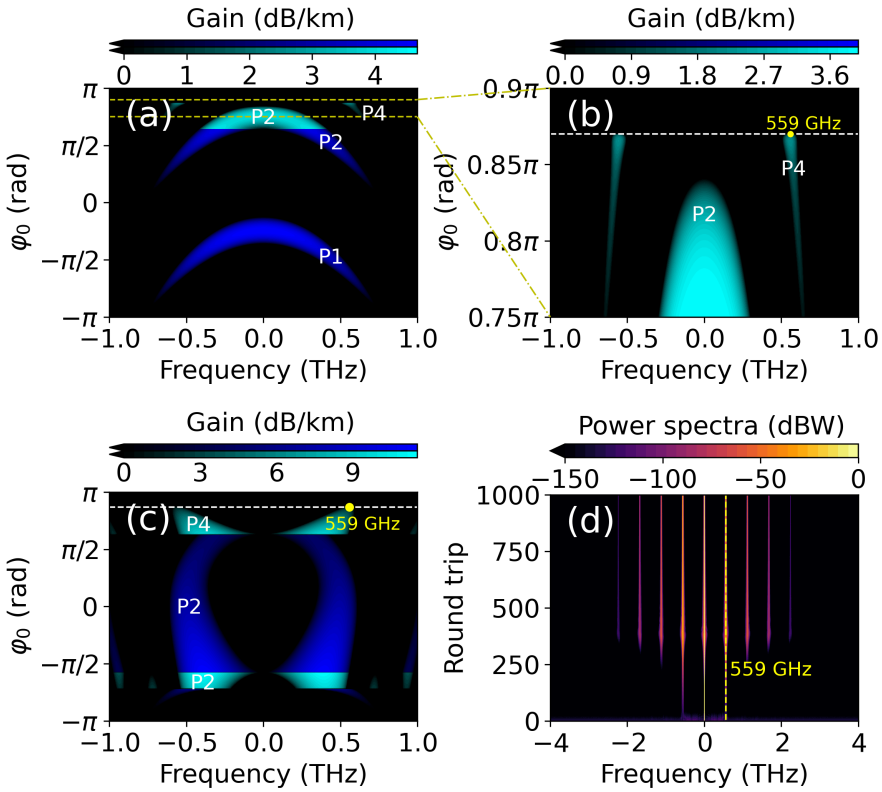

Figure 10.2: MI gain and cavity spectrum. (a) MI gain spectra for fixed average intracavity power $(P_X + P_Y)/2 = 0.312$ W: the blue regions correspond to MI of stationary CW solutions, whereas the cyan regions correspond to MI of period-doubled CW solutions [similarly for (b) and (c)]. (b) Close-up of (a); note that part of the P2 MI gain of stationary CW is obscured by the P2 MI gain of the period-doubled CW. (c) MI gain calculated for the lowest-power stable CW solutions at fixed input power. (d) Power-spectrum evolution over round trips. Other parameters: $P_{\text{in}} = 10$ W, $\varphi_0 = 0.87\pi$, $\gamma = 2.5$ W^{-1}km^{-1}, $\rho = \sqrt{0.8}$, $\theta = \sqrt{0.1}$, $L = 0.5$ km, $\beta_2 = 0.4$ ps^2/km, $\xi = 0.954$, and $\alpha = 0.046$ km^{-1} (equivalent to 0.2 dB/km).

straightforward: P2 MI appears when Λ is real and positive with an even K, whereas P4 MI occurs when Λ is real and negative with an odd K. Around $\varphi_0 = 0.8\pi$, the period-doubled CW solutions emerge and exhibit P4 MI.

To provide an experimentally accessible example, Fig. 10.2(c) displays MI gain spectra for a fixed input power P_{in}, focusing only on the lowest-power stable CW branch (i.e., the branch of smaller power values between the black and red curves in Fig. 10.1(d)).

In Fig. 10.2(d), we present the power-spectrum evolution over several cavity round trips obtained from numerical simulations at $\varphi_0 = 0.87\pi$, corresponding to the dashed horizontal line in Figs. 10.2(b) and 10.2(c). The detuning of the primary sidebands with respect to the pump frequency agrees excellently with the analytical prediction indicated by the vertical dashed line.

In Fig. 10.3, we report the P4 temporal MI patterns obtained from numerical simulations. The modulation exhibits a π phase shift not after every round trip—as in P2 MI—but instead after two round trips.

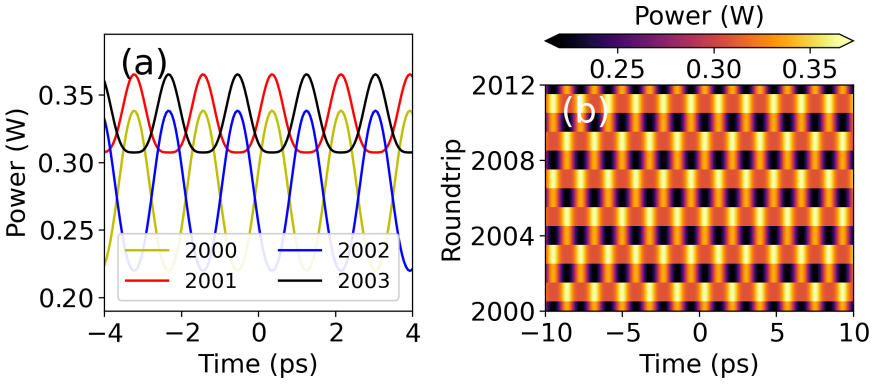

Figure 10.3: P4 MI temporal patterns from simulations. (a) P4 temporal patterns for four consecutive round trips (2000–2003) plotted in yellow, red, blue, and black, respectively. (b) P4 temporal patterns vs round trip number. Parameters are the same as in Fig. 10.2.

The problem addressed in this chapter is mathematically equivalent to MI in Möbius fibre resonators—two coupled ring cavities described by coupled Ikeda maps—in which P4 MI patterns were theoretically predicted [121]. However, the physical systems differ: P4 MI in Ref. [121] arises in two coupled cavities with mismatched parameters such as different detunings, whereas our work predicts P4 MI in a single ring fibre resonator, offering a simpler and more compact configuration.

10.4 Conclusions

We have investigated the highly nonlinear regime of MI in a multistable driven optical fibre cavity, focusing on the stability of period-doubled CW solutions. Using two coupled Ikeda maps, we have analytically and numerically predicted and characterized a P4 MI — a P2 growth of sidebands over a period-doubled pump — whose temporal pattern repeats after four consecutive cavity round trips. We derived an analytical expression for the MI gain, and its predictions are confirmed by numerical simulations. The P4 MI regime is achievable under experimentally accessible parameters. Our demonstration of P4 MI in a single nonlinear optical resonator broadens the understanding of Kerr-resonator dynamics, where studies of MI have traditionally focused on stationary CW solutions. Moreover, higher-period MI (beyond P4) can be attained using higher-period CW solutions, although

this requires significantly higher input power. A systematic theoretical investigation of the P-n mechanism, where n is an even number, will be a future objective.

Chapter 11

Conclusion

This thesis has investigated the fundamental and applied aspects of nonlinear optical effects in guided-wave systems, with a particular focus on two interconnected domains: parametric amplification in two coupled waveguides, emergence of MI and MI-driven frequency comb generation in fibre ring resonators.

In this thesis, we have explored a wide range of nonlinear optical effects and their applications, focusing primarily on dual-waveguide OPA, MI, and OFC generation across distinct physical platforms. Our work spans theoretical modelling, numerical simulations, and conceptual design for practical implementations, offering new insights into waveguide and resonator systems.

In the first part of the thesis, we began by demonstrating that coupling dispersion is a powerful physical mechanism for dispersion engineering in dual-waveguide parametric amplifiers. This finding opens new possibilities for broadband amplification, even in normally dispersive waveguides, by tailoring the gain spectrum through the coupling parameters. The ability to harness frequency-dependent coupling offers a versatile route to engineer amplifiers with desirable features such as flat gain profiles and loss compensation, suggesting utility in multi-core fibres and photonic circuits with complex topologies. Next, we analysed the robustness of equally pumped dual-waveguide parametric amplifiers against relative power and phase fluctuations. Our analytical and numerical results show that these systems maintain stable operation under realistic perturbations, providing useful design guidelines for photonic devices where gain uniformity and stability are critical. We then explored intermodal four-wave mixing in dual-core optical fibres, presenting both analytical and nu-

merical models for asymmetric gain and signal-idler generation into distinct supermodes. By identifying the interplay between pump imbalance and frequency-dependent coupling as a key control knob, we proposed a scheme for idler-free parametric amplification. This concept has implications for bandwidth efficiency and is adaptable to a variety of integrated platforms beyond conventional silica fibres.

In the second part of the thesis, we turned our attention to fibre ring resonators. We implemented the GTF method in a fibre ring resonator enhanced by an EDFA. Our experiments demonstrated reduced power thresholds and improved energy transfer to sidebands, indicating the effectiveness of intracavity gain in enhancing GTF-induced instabilities. These results contribute to the ongoing development of energy-efficient and spectrally broad OFC sources. Then, we investigated GTF-induced MI in hybrid quadratic–cubic resonators. Using a combination of analytical gain calculations and numerical simulations, we showed that spectral asymmetries introduced by filtering enable tunable OFC generation in parametrically driven resonators. Finally, we extended our analysis to the strongly nonlinear regime of driven Kerr resonators. We identified and characterised a P4 MI, where the system exhibits periodic behaviour over four cavity round trips. Our derivation of the MI gain, validated by simulations, offers the first demonstration of P4 MI in a single nonlinear resonator and enriches the landscape of known dynamical instabilities in optical cavities.

Overall, this thesis offers a unified treatment of parametric processes in waveguides and resonators across various nonlinear regimes. It provides both theoretical tools and practical design strategies for manipulating light through nonlinear interactions. Future work may focus on the role of nonlinear coupling in dual-waveguide systems, the impact of the randomness of the coupling strength on dual-waveguide OPA, experimental realisations of intermodal amplification schemes, on-chip integration of GTF-based comb sources, further exploration of multistability and pattern formation in complex resonators, and investigation of driven nonlinear dual-waveguide or dual-core fibre resonators.

List of References

[1] M. Shi, V. Ribeiro, and A. M. Perego. Parametric amplification in coupled nonlinear waveguides: the role of coupling dispersion. *Front. Photon.*, 4:1051294, 2023.

[2] M. Shi, V. Ribeiro, and A. M. Perego. On the resilience of dual-waveguide parametric amplifiers to pump power and phase fluctuations. *Appl. Phys. Lett.*, 122(10):101102, 2023.

[3] M. Shi, V. Ribeiro, and A. M. Perego. Parametric amplification based on intermodal four-wave mixing between different supermodes in coupled-core fibers. *Opt. Express*, 31(6):9760–9768, 2023.

[4] M. Shi, M. Conforti, A. Mussot, and A. M. Perego. Period-4 modulation instability in ring fiber cavities. *Phys. Rev. A*, 111(1):013513, 2025.

[5] M. Shi, N. Englebert, F. Leo, D. V. Skryabin, and A. M. Perego. Modulation instability and frequency comb generation in hybrid quadratic-cubic resonators with spectral filter. *Phys. Rev. A*, 112(2):023522, 2025.

[6] M. Shi, S. Negrini, N. Englebert, F. Leo, M. Conforti, A. Mussot, and A. M. Perego. Amplifier enhanced gain-through-filtering instability in a hybrid kerr cavity. *Opt. Express*, 33(21):43665–43675, 2025.

[7] V. Ribeiro, M. Shi, and A. M. Perego. Impact of zero-dispersion wavelength fluctuations in a coupled dual-core fiber optical parametric amplifier. *J. Lightwave Technol.*, 41(19):6235–6243, 2023.

[8] M. Gong, M. Shi, Y. Li, X. Xu, Z. Fei, Y. Qiao, J. Liu, A. He, and X. Liu. Resonant adhesion structure makes negative acoustic radiation force. *Phys. Fluids*, 35(5), 2023.

[9] G. P. Agrawal. Nonlinear fiber optics, 5th edition. Academic Press, Oxford, 2012.

[10] R. W. Boyd, A. L. Gaeta, and E. Giese. Nonlinear optics. In *Springer Handbook of Atomic, Molecular, and Optical Physics*. Springer, 2008.

[11] D. Thomson, A. Zilkie, J. E. Bowers, T. Komljenovic, G. T. Reed, L. Vivien, D. Marris-Morini, E. Cassan, L. Virot, J. Fédéli, et al. Roadmap on silicon photonics. *J. Opt.*, 18(7):073003, 2016.

[12] A. Gondarenko, J. S. Levy, and M. Lipson. High confinement micron-scale silicon nitride high q ring resonator. *Opt. Express*, 17(14):11366–11370, 2009.

[13] M. H. P. Pfeiffer, J. Liu, A. S. Raja, T. Morais, B. Ghadiani, and T. J. Kippenberg. Ultra-smooth silicon nitride waveguides based on the damascene reflow process: fabrication and loss origins. *Optica*, 5(7):884–892, 2018.

[14] M. M. Fejer, G. Magel, D. H. Jundt, and R. L. Byer. Quasi-phase-matched second harmonic generation: tuning and tolerances. *IEEE J. Quantum Electron.*, 28(11): 2631–2654, 1992.

[15] S. Trillo and S. Wabnitz. Parametric and raman amplification in birefringent fibers. *J. Opt. Soc. Am. B*, 9(7):1061–1082, 1992.

[16] A. S. Y. Hsieh, G. K. L. Wong, S. G. Murdoch, S. Coen, F. Vanholsbeeck, R. Leonhardt, and J. D. Harvey. Combined effect of raman and parametric gain on single-pump parametric amplifiers. *Opt. Express*, 15(13):8104–8114, 2007.

[17] A. S. Y. Hsieh, S. G. Murdoch, S. Coen, R. Leonhardt, and J. D. Harvey. Influence of raman susceptibility on optical parametric amplification in optical fibers. *Opt. Lett.*, 32(5):521–523, 2007.

[18] R. Soref and B. Bennett. Electrooptical effects in silicon. *IEEE J. Quantum Electron.*, 23(1):123–129, 1987.

[19] A. V. Buryak, P. Di Trapani, D. V. Skryabin, and S. Trillo. Optical solitons due to quadratic nonlinearities: from basic physics to futuristic applications. *Phys. Rep.*, 370 (2):63–235, 2002.

[20] R. Stolen. Phase-matched-stimulated four-photon mixing in silica-fiber waveguides. *IEEE J. Quantum Electron.*, 11(3):100–103, 1975.

[21] R. Stolen and J. Bjorkholm. Parametric amplification and frequency conversion in optical fibers. *IEEE J. Quantum Electron.*, 18(7):1062–1072, 1982.

[22] R. Carman, R. Chiao, and P. Kelley. Observation of degenerate stimulated four-photon interaction and four-wave parametric amplification. *Phys. Rev. Lett.*, 17(26): 1281, 1966.

[23] G. Cappellini and S. Trillo. Third-order three-wave mixing in single-mode fibers: exact solutions and spatial instability effects. *J. Opt. Soc. Am. B*, 8(4):824–838, 1991.

[24] R. Schiek. Nonlinear refraction caused by cascaded second-order nonlinearity in optical waveguide structures. *J. Opt. Soc. Am. B*, 10(10):1848–1855, 1993.

[25] F. Leo, T. Hansson, I. Ricciardi, M. D. Rosa, S. Coen, S. Wabnitz, and M. Erkintalo. Walk-off-induced modulation instability, temporal pattern formation, and frequency comb generation in cavity-enhanced second-harmonic generation. *Phys. Rev. Lett.*, 116(3), 2016.

[26] M. E. Mahric. *Fiber Optical Parametric Amplifiers, Oscillators and Related Devices: Theory, Applications, and Related Devices.* Cambridge University Press, 2007.

[27] P. A. Andrekson and M. Karlsson. Fiber-based phase-sensitive optical amplifiers and their applications. *Adv. Opt. Photon.*, 12(2):367–428, 2020.

[28] A. Hasegawa and W. Brinkman. Tunable coherent ir and fir sources utilizing modulational instability. *IEEE J. Quantum Electron.*, 16(7):694–697, 1980.

[29] Z. Ye, P. Zhao, K. Twayana, M. Karlsson, P. A. Andrekson, and V. Torres-Company. Ultralow-loss meter-long dispersion-engineered silicon nitride waveguides. In *Conference on Lasers and Electro-Optics*, page SF1C.5. Optical Society of America, 2021.

[30] Z. Ye, P. Zhao, K. Twayana, M. Karlsson, V. Torres-Company, and P. A. Andrekson. Overcoming the quantum limit of optical amplification in monolithic waveguides. *Sci. Adv.*, 7(38):eabi8150, 2021.

[31] V. I. Bespalov and V. I. Talanov. Filamentary structure of light beams in nonlinear liquids. *Soviet Journal of Experimental and Theoretical Physics Letters*, 3:307, 1966.

[32] K. Tai, A. Hasegawa, and A. Tomita. Observation of modulational instability in optical fibers. *Phys. Rev. Lett.*, 56:135–138, 1986.

[33] T. Fortier and E. Baumann. 20 years of developments in optical frequency comb technology and applications. *Commun. Phys.*, 2:153, 2019.

[34] A. M. Perego and A. Ellis. *Optical Frequency Combs, Trends in Sources and Applications*. CRC Press, Boca Raton, 2024.

[35] J. M. Dudley, G. Genty, and S. Coen. Supercontinuum generation in photonic crystal fiber. *Rev. Mod. Phys.*, 78(4):1135–1184, 2006.

[36] P. Del'Haye, A. Schliesser, O. Arcizet, T. Wilken, R. Holzwarth, and T. J. Kippenberg. Optical frequency comb generation from a monolithic microresonator. *Nature*, 450 (7173):1214–1217, 2007.

[37] T. J. Kippenberg, R. Holzwarth, and S. A. Diddams. Microresonator-based optical frequency combs. *Science*, 332(6029):555–559, 2011.

[38] T. Udem, R. Holzwarth, and T. W. Hänsch. Optical frequency metrology. *Nature*, 416(6877):233–237, 2002.

[39] S. T. Cundiff and J. Ye. Colloquium: Femtosecond optical frequency combs. *Rev. Mod. Phys.*, 75:325–342, 2003.

[40] P. Everitt, M. Sooriyabandara, M. Guasoni, P. Wigley, C. Wei, G. McDonald, K. Hardman, P. Manju, J. Close, C. Kuhn, et al. Observation of a modulational instability in bose-einstein condensates. *Phys. Rev. A*, 96(4):041601, 2017.

[41] V. E. Zakharov et al. Collapse of langmuir waves. *Sov. Phys. JETP*, 35(5):908–914, 1972.

[42] V. E. Zakharov. Stability of periodic waves of finite amplitude on the surface of a deep fluid. *J. Appl. Mech. Tech. Phy.*, 9(2):190–194, 1968.

[43] A. Mecozzi. Parametric amplification and squeezed-light generation in a nonlinear directional coupler. *Opt. Lett.*, 13(10):925–927, 1988.

[44] S. Trillo, S. Wabnitz, G. I. Stegeman, and E. M. Wright. Parametric amplification and modulational instabilities in dispersive nonlinear directional couplers with relaxing nonlinearity. *J. Opt. Soc. Am. B*, 6(5):889–900, 1989.

[45] V. Ribeiro, M. Karlsson, and P. Andrekson. Parametric amplification with a dual-core fiber. *Opt. Express*, 25(6):6234–6243, 2017.

[46] V. Ribeiro, A. Lorences-Riesgo, P. Andrekson, and M. Karlsson. Noise in phase-(in)sensitive dual-core fiber parametric amplification. *Opt. Express*, 26(4):4050–4059, 2018.

[47] A. D. Szabo, V. Ribeiro, C. B. Gaur, A. A. I. Ali, A. Mussot, Y. Quiquempois, G. Bouwmans, and N. J. Doran. Dual-polarization c+l-band wavelength conversion in a twin-core highly nonlinear fibre. *OFC 2021 Virtual conference, Paper MB5.4*, 2021.

[48] V. Ribeiro and A. M. Perego. Parametric amplification in lossy nonlinear waveguides with spatially dependent coupling. *Opt. Express*, 30(10):17614–17624, 2022.

[49] V. Ribeiro and A. M. Perego. Theory of parametric amplification in coupled lossy waveguides. In *Conference on Lasers and Electro-Optics*, page JTh3A.12. Optical Society of America, 2022.

[50] M. Karlsson, J. Schröder, P. Zhao, and P. A. Andrekson. Analytic theory for parametric gain in lossy integrated waveguides. In *Conference on Lasers and Electro-Optics*, page JTh3A.5. Optical Society of America, 2021.

[51] P. Zhao, Z. Ye, K. Vijayan, C. Naveau, J. Schröder, M. Karlsson, and P. A. Andrekson. Waveguide tapering for improved parametric amplification in integrated nonlinear si3n4 waveguides. *Opt. Express*, 28(16):23467–23477, 2020.

[52] S. Trillo and S. Wabnitz. Nonlinear dynamics of parametric wave-mixing interactions in optics: instabilities and chaos. In *Guided Wave Nonlinear Optics*, pages 489–534. Springer, 1992.

[53] C. J. Benton and D. V. Skryabin. Coupling induced anomalous group velocity dispersion in nonlinear arrays of silicon photonic wires. *Opt. Express*, 17(7):5879–5884, 2009.

[54] C. E. D. Nobriga, G. D. Hobbs, W. J. Wadsworth, J. C. Knight, D. V. Skryabin, A. Samarelli, M. Sorel, and R. M. D. L. Rue. Supermode dispersion and waveguide-to-slot mode transition in arrays of silicon-on-insulator waveguides. *Opt. Lett.*, 35 (23):3925–3927, 2010.

[55] W. Ding, O. K. Staines, G. D. Hobbs, A. V. Gorbach, C. D. Nobriga, W. J. Wadsworth, J. C. Knight, D. V. Skryabin, M. J. Strain, M. Sorel, and R. M. D. L. Rue. Modulational instability in a silicon-on-insulator directional coupler: role of the coupling-induced group velocity dispersion. *Opt. Lett.*, 37(4):668–670, 2012.

[56] J. H. Li, K. S. Chiang, and K. W. Chow. Modulation instabilities in two-core optical fibers. *J. Opt. Soc. Am. B*, 28(7):1693–1701, 2011.

[57] J. H. Li, K. S. Chiang, B. A. Malomed, and K. W. Chow. Modulation instabilities in birefringent two-core optical fibres. *J. Phys. B: At. Mol. Opt. Phys.*, 45(16):165404, 2012.

[58] K. Nithyanandan, R. V. J. Raja, and K. Porsezian. Modulational instability in a twin-core fiber with the effect of saturable nonlinear response and coupling coefficient dispersion. *Phys. Rev. A*, 87:043805, 2013.

[59] A. A. Nair, K. Porsezian, and M. Jayaraju. Impact of higher order dispersion and nonlinearities on modulational instability in a dual-core optical fiber. *Eur. Phys. J. D*, 72:6, 2018.

[60] J. H. Li, T. T. Sun, Y. Q. Ma, Y. Chen, Z. L. Cao, F. L. Xian, D. Z. Wang, and W. Wang. Modulation instabilities in nonlinear two-core optical fibers with fourth order dispersion. *Optik*, 208:164134, 2020. ISSN 0030-4026.

[61] J. H. Li, T. T. Sun, Y. Q. Ma, Y. Y. Chen, Z. L. Cao, and F. L. Xian. The effects of fourth-order dispersion on modulation instabilities in two-core optical fibers with asymmetric CW state. *Phys. Scripta*, 95(11):115502, 2020.

[62] J. Hansryd, P. A. Andrekson, M. Westlund, and Li.

[63] A. Mecozzi, C. Antonelli, and M. Shtaif. Coupled-core fiber optics: An analytical study of the impact of core imperfections on multicore systems. *Opt. Express*, 14(24): 11839–11851, 2006.

[64] V. Gordienko, M. F. C. Stephens, A. E. El-Taher, and N. J. Doran. Ultra-flat wide-band single-pump raman-enhanced parametric amplification. *Opt. Express*, 25(5): 4810–4818, 2017.

[65] S. Olsson, H. Eliasson, E. Astra, M. Karlsson, and P. A. Andrekson. Long-haul optical transmission link using low-noise phase-sensitive amplifiers. *Nat. Commun.*, 9:2513, 2018.

[66] L. Instruments. Moku:Pro's Phasemeter. `https://www.liquidinstruments.com`, 2022.

[67] Thorlabs. 1550 nm 1x2 Single Mode Fused Fiber Optic Couplers Taps. `https://www.thorlabs.com/newgrouppage9.cfm?objectgroup_id=9567`, 2022.

[68] A. Mussot, E. Louvergneaux, N. Akhmediev, F. Reynaud, L. Delage, and M. Taki. Optical fiber systems are convectively unstable. *Phys. Rev. Lett.*, 101:113904, 2008.

[69] M. I. Kolobov, A. Mussot, A. Kudlinski, E. Louvergneaux, and M. Taki. Third-order dispersion drastically changes parametric gain in optical fiber systems. *Phys. Rev. A*, 83:035801, 2011.

[70] M. Droques, B. Barviau, A. Kudlinski, M. Taki, A. Boucon, T. Sylvestre, and A. Mussot. Symmetry-breaking dynamics of the modulational instability spectrum. *Opt. Lett.*, 36(8):1359–1361, 2011.

[71] Z. Lali-Dastjerdi, K. Rottwitt, M. Galili, and C. Peucheret. Asymmetric gain-saturated spectrum in fiber optical parametric amplifiers. *Opt. Express*, 20(14):15530–15539, 2012.

[72] T. Tanemura, Y. Ozeki, and K. Kikuchi. Modulational instability and parametric amplification induced by loss dispersion in optical fibers. *Phys. Rev. Lett.*, 93:163902, 2004.

[73] A. M. Perego, S. K. Turitsyn, and K. Staliunas. Gain through losses in nonlinear optics. *Light: Sci. Appl.*, 7:43, 2018.

[74] R. El-Ganainy, J. I. Dadap, and R. M. Osgood. Optical parametric amplification via non-hermitian phase matching. *Opt. Lett.*, 40(21):5086–5089, 2015.

[75] V. Gordienko, F. M. Ferreira, V. Ribeiro, and N. Doran. Design of an interferometric fiber optic parametric amplifier for the rejection of unwanted four-wave mixing products. *Opt. Express*, 31(5):8226–8239, 2023.

[76] R. Essiambre, M. A. Mestre, R. Ryf, A. H. Gnauck, R. W. Tkach, A. R. Chraplyvy, Y. Sun, X. Jiang, and R. Lingle. Experimental investigation of inter-modal four-wave mixing in few-mode fibers. *IEEE Photon. Technol. Lett.*, 25(6):539–542, 2013.

[77] H. Pourbeyram, E. Nazemosadat, and A. Mafi. Detailed investigation of intermodal four-wave mixing in smf-28: blue-red generation from green. *Opt. Express*, 23(11): 14487–14500, 2015.

[78] Y. Xiao, R. Essiambre, M. Desgroseilliers, A. M. Tulino, R. Ryf, S. Mumtaz, and G. P. Agrawal. Theory of intermodal four-wave mixing with random linear mode coupling in few-mode fibers. *Opt. Express*, 22(26):32039–32059, 2014.

[79] S. M. M. Friis, I. Begleris, Y. Jung, K. Rottwitt, P. Petropoulos, D. J. Richardson, P. Horak, and F. Parmigiani. Inter-modal four-wave mixing study in a two-mode fiber. *Opt. Express*, 24(26):30338–30349, 2016.

[80] J. H. Li, K. S. Chiang, and K. W. Chow. Modulation instabilities in two-core optical fibers. *J. Opt. Soc. Am. B*, 28(7):1693–1701, 2011.

[81] M. Nakazawa, K. Suzuki, and H. A. Haus. Modulational instability oscillation in nonlinear dispersive ring cavity. *Phys. Rev. A*, 38:5193–5196, 1988.

[82] M. Haelterman, S. Trillo, and S. Wabnitz. Dissipative modulation instability in a nonlinear dispersive ring cavity. *Opt. Commun.*, 91(5):401 – 407, 1992.

[83] M. Haelterman, S. Trillo, and S. Wabnitz. Additive-modulation-instability ring laser in the normal dispersion regime of a fiber. *Opt. Lett.*, 17(10):745–747, 1992.

[84] L. A. Lugiato and R. Lefever. Spatial dissipative structures in passive optical systems. *Phys. Rev. Lett.*, 58(21):2209, 1987.

[85] L. Lugiato, F. Prati, M. Gorodetsky, and T. Kippenberg. From the lugiato–lefever equation to microresonator-based soliton kerr frequency combs. *Philosophical Transactions of the Royal Society A: Mathematical, Physical and Engineering Sciences*, 376 (2135):20180113, 2018.

[86] F. Castelli, M. Brambilla, A. Gatti, F. Prati, and L. A. Lugiato. The lle, pattern formation and a novel coherent source. *Eur. Phys. J. D*, 71(4):84, 2017.

[87] S. A. Diddams, K. Vahala, and T. Udem. Optical frequency combs: Coherently uniting the electromagnetic spectrum. *Science*, 369(6501):eaay3676, 2020.

[88] A. Parriaux, K. Hammani, and G. Millot. Electro-optic frequency combs. *Adv. Opt. Photon.*, 12(1):223–287, 2020.

[89] A. L. Gaeta, M. Lipson, and T. J. Kippenberg. Photonic-chip-based frequency combs. *Nat. Photonics*, 13:158–169, 2019.

[90] A. M. Perego et al. Optical frequency combs in fibre resonators. In A. M. Perego and A. D. Ellis, editors, *Optical Frequency Combs. Trends in Sources and Applications*, chapter 7, pages 153–174. CRC Press, Boca Raton, 2024.

[91] F. Leo et al. Temporal cavity solitons in one-dimensional kerr media as bits in an all-optical buffer. *Nat. Photonics*, 4:471–476, 2010.

[92] D. Braje, L. Hollberg, and S. Diddams. Brillouin-enhanced hyperparametric generation of an optical frequency comb in a monolithic highly nonlinear fiber cavity pumped by a cw laser. *Phys. Rev. Lett.*, 102(19):193902, 2009.

[93] T. Bunel, M. Conforti, Z. Ziani, J. Lumeau, A. Moreau, A. Fernandez, O. Llopis, J. Roul, A. M. Perego, K. K. Y. Wong, and A. Mussot. Observation of modulation instability kerr frequency combs in a fiber fabry–pérot resonator. *Opt. Lett.*, 48(2): 275–278, 2023.

[94] T. Bunel, M. Conforti, Z. Ziani, J. Lumeau, A. Moreau, A. Fernandez, O. Llopis, G. Bourcier, and A. Mussot. 28 thz soliton frequency comb in a continuous-wave pumped fiber fabry–pérot resonator. *APL Photonics*, 9(1):010804, 2024.

[95] M. Nie, K. Jia, Y. Xie, S. Zhu, Z. Xie, and S. Huang. Synthesized spatiotemporal mode-locking and photonic flywheel in multimode mesoresonators. *Nat. Commun.*, 13(1):6395, 2022.

[96] F. Bessin, A. M. Perego, K. Staliunas, S. K. Turitsyn, A. Kudlinski, M. Conforti, and A. Mussot. Gain-through-filtering enables tuneable frequency comb generation in passive optical resonators. *Nat. Commun.*, 10(1), 2019.

[97] A. M. Perego, A. Mussot, and M. Conforti. Theory of filter-induced modulation instability in driven passive optical resonators. *Phys. Rev. A*, 103(1):013522, 2021.

[98] K. Ikeda. Multiple-valued stationary state and its instability of the transmitted light by a ring cavity system. *Opt. Commun.*, 30(2):257–261, 1979.

[99] H. Nakatsuka, S. Asaka, H. Itoh, K. Ikeda, and M. Matsuoka. Observation of bifurcation to chaos in an all-optical bistable system. *Phys. Rev. Lett.*, 50(2):109, 1983.

[100] S. Coen and M. Haelterman. Modulational instability induced by cavity boundary conditions in a normally dispersive optical fiber. *Phys. Rev. Lett.*, 79:4139–4142, 1997.

[101] M. Conforti, F. Copie, A. Mussot, A. Kudlinski, and S. Trillo. Parametric instabilities in modulated fiber ring cavities. *Opt. Lett.*, 41(21):5027, 2016.

[102] N. Englebert, C. M. Arabí, P. Parra-Rivas, S. Gorza, and F. Leo. Temporal solitons in a coherently driven active resonator. *Nat. Photonics*, 15(7):536–541, 2021.

[103] H. Bao, A. Cooper, M. Rowley, L. Di Lauro, J. S. Totero Gongora, S. T. Chu, B. E. Little, G. Oppo, R. Morandotti, D. J. Moss, et al. Laser cavity-soliton microcombs. *Nat. Photonics*, 13(6):384–389, 2019.

[104] A. Haboucha, H. Leblond, M. Salhi, A. Komarov, and F. Sanchez. Analysis of soliton pattern formation in passively mode-locked fiber lasers. *Phys. Rev. A*, 78(4), 2008.

[105] E. D. Black. An introduction to Pound–Drever–Hall laser frequency stabilization. *Am. J. Phys.*, 69(1):79–87, 2001.

[106] N. Englebert, F. De Lucia, P. Parra-Rivas, C. Mas Arabí, P. Sazio, S. Gorza, and F. Leo. Parametrically driven kerr cavity solitons. *Nat. Photonics*, 15(11):857–861, 2021.

[107] S. Mosca, M. Parisi, I. Ricciardi, F. Leo, T. Hansson, M. Erkintalo, P. Maddaloni, P. D. Natale, S. Wabnitz, and M. D. Rosa. Modulation instability induced frequency comb generation in a continuously pumped optical parametric oscillator. *Phys. Rev. Lett.*, 121(9), 2018.

[108] M. Zhang, B. Buscaino, C. Wang, A. Shams-Ansari, C. Reimer, R. Zhu, J. M. Kahn, and M. Lončar. Broadband electro-optic frequency comb generation in a lithium niobate microring resonator. *Nature*, 568(7752):373–377, 2019. ISSN 1476-4687.

[109] J. Lu, D. N. Puzyrev, V. V. Pankratov, D. V. Skryabin, F. Yang, Z. Gong, J. B. Surya, and H. X. Tang. Two-colour dissipative solitons and breathers in microresonator second-harmonic generation. *Nat. Commun.*, 14:2798, 2023.

[110] F. D. Lucia, D. Huang, C. Corbari, N. Healy, and P. J. A. Sazio. Optical fiber poling by induction. *Opt. Lett.*, 39(22):6513–6516, 2014.

[111] F. De Lucia, R. Bannerman, N. Englebert, M. M. A. Nunez Velazquez, F. Leo, J. Gates, S. Gorza, J. Sahu, and P. J. A. Sazio. Single is better than double: theoretical and experimental comparison between two thermal poling configurations of optical fibers. *Opt. Express*, 27(20):27761–27776, 2019.

[112] D. V. Skryabin. Coupled-mode theory for microresonators with quadratic nonlinearity. *J. Opt. Soc. Am. B*, 37(9):2604–2614, 2020.

[113] D. N. Puzyrev, V. V. Pankratov, A. Villois, and D. V. Skryabin. Bright-soliton frequency combs and dressed states in chi(2) microresonators. *Phys. Rev. A*, 104: 013520, 2021.

[114] D. N. Puzyrev and D. V. Skryabin. Carrier-resolved real-field theory of multi-octave frequency combs. *Optica*, 10:770, 2023.

[115] S Trillo and P Ferro. Modulational instability in second-harmonic generation. *Opt. Lett.*, 20(5):438–440, 1995.

[116] S. Trillo and M. Haelterman. Pulse-train generation through modulational instability in intracavity second-harmonic generation. *Opt. Lett.*, 21(15):1114–1116, 1996.

[117] F. Bessin, F. Copie, M. Conforti, A. Kudlinski, A. Mussot, and S. Trillo. Real-time characterization of period-doubling dynamics in uniform and dispersion oscillating fiber ring cavities. *Phys. Rev. X*, 9:041030, 2019.

[118] M. Haelterman. Period-doubling bifurcations and modulational instability in the nonlinear ring cavity: an analytical study. *Opt. Lett.*, 17(11):792, 1992.

[119] M. Haelterman. Simple model for the study of period-doubling instabilities in the nonlinear ring cavity. *Appl. Phys. Lett.*, 61:2756 – 2758, 1992.

[120] M. Haelterman. Ikeda instability and transverse effects in nonlinear ring resonators. *Opt. Commun.*, 100:389 – 398, 1993.

[121] C. Maitland, M. Conforti, A. Mussot, and F. Biancalana. Stationary states and instabilities of a möbius fiber resonator. *Phys. Rev. Res.*, 2:043195, 2020.

Appendix A

Derivation of nonlinear Schrödinger equation

Maxwell's equations in matter are

$$\nabla \times \mathbf{E} = -\frac{\partial \mathbf{B}}{\partial t}, \tag{A.1}$$

$$\nabla \times \mathbf{H} = \mathbf{J}_f + \frac{\partial \mathbf{D}}{\partial t}, \tag{A.2}$$

$$\nabla \cdot \mathbf{D} = \rho_f, \tag{A.3}$$

$$\nabla \cdot \mathbf{B} = 0, \tag{A.4}$$

where

$$\mathbf{D} = \epsilon_0 \mathbf{E} + \mathbf{P}, \tag{A.5}$$

$$\mathbf{H} = \frac{1}{\mu_0}\,\mathbf{B} - \mathbf{M}, \tag{A.6}$$

$$\rho_f = \rho - (-\nabla \cdot \mathbf{P}), \tag{A.7}$$

$$\mathbf{J}_f = \mathbf{J} - (\nabla \times \mathbf{M} + \frac{\partial \mathbf{P}}{\partial t}). \tag{A.8}$$

Considering a material with no free charge, no free current, and being nonmagnetic, i.e., $\mathbf{J}_f = 0$, $\rho_f = 0$, $\mathbf{M} = 0$, we obtain

$$\nabla \times \nabla \times \mathbf{E} = \nabla \times (-\frac{\partial \mathbf{B}}{\partial t}) = -\mu_0 \frac{\partial^2 \mathbf{D}}{\partial t^2} = -\mu_0 \epsilon_0 \frac{\partial^2 \mathbf{E}}{\partial t^2} - \mu_0 \frac{\partial^2 \mathbf{P}}{\partial t^2}, \tag{A.9}$$

The polarization $\mathbf{P}$ is usually given by the Taylor series in $\mathbf{E}$,

$$\begin{aligned}
\mathbf{P}(\mathbf{r}, t) &= \epsilon_0(\chi^{(1)} \cdot \mathbf{E} + \chi^{(2)} : \mathbf{E}\mathbf{E} + \chi^{(3)} \vdots \mathbf{E}\mathbf{E}\mathbf{E} + \ldots) \\
&= \epsilon_0 \sum_i \tilde{i} \left[\sum_j \chi^{(1)}_{ij} E_j + \sum_{jk} \chi^{(2)}_{ijk} E_j E_k + \sum_{jkl} \chi^{(3)}_{ijkl} E_j E_k E_l + \ldots \right] \\
&= \mathbf{P}_{\mathrm{L}} + \mathbf{P}_{\mathrm{NL}},
\end{aligned} \tag{A.10}$$

where the first linear term is explicitly denoted as $\mathbf{P}_{\mathrm{L}}$, and the others are represented by $\mathbf{P}_{\mathrm{NL}}$. However, if the material cannot response instantaneously, the product should be replaced by convolution over time, as χ^i is frequency dependent in this case. As $\nabla \cdot \mathbf{E}$ is usually negligible, especially when the slowly varying amplitude approximation (SVEA) is valid [10], we can approximate $\nabla \times \nabla \times \mathbf{E} = \nabla(\nabla \cdot \mathbf{E}) - \nabla^2 E \approx -\nabla^2 E$. As a result,

$$\nabla^2 \mathbf{E} - \mu_0 \epsilon_0 \frac{\partial^2 \mathbf{E}}{\partial t^2} - \mu_0 \frac{\partial^2 \mathbf{P}_{\mathrm{L}}}{\partial t^2} = \mu_0 \frac{\partial^2 \mathbf{P}_{\mathrm{NL}}}{\partial t^2}. \tag{A.11}$$

For the linear part of $\mathbf{P}$, in consideration the frequency dependency of $\chi^{(1)}$, we have, in the frequency domain,

$$\tilde{\mathbf{P}}_{\mathrm{L}}(\mathbf{r}, \omega) = \epsilon_0 \chi^{(1)}(\omega) \cdot \tilde{\mathbf{E}}(\mathbf{r}, \omega). \tag{A.12}$$

In the absence of the nonlinear source term, Eq. (A.11) gives the wave equation in the frequency domain as

$$\nabla^2 \tilde{\mathbf{E}}(\mathbf{r}, \omega) + \epsilon(\omega) \frac{\omega^2}{c^2} \tilde{\mathbf{E}}(\mathbf{r}, \omega) = 0 \tag{A.13}$$

where $c = 1/\sqrt{\mu_0 \epsilon_0}$ and $\epsilon(\omega) = 1 + \chi^{(1)}(\omega)$. Both ϵ and $\chi^{(1)}$ are rank-2 tensors.

In a $\chi^{(3)}$ medium like silica glasses, where $\chi^{(2)}$ vanishes due to the inversion symmetry, if we assume the nonlinear response is instantaneous, we have

$$\mathbf{P}_{\mathrm{NL}} = \epsilon_0 \chi^{(3)} \vdots \mathbf{EEE}. \tag{A.14}$$

In the case of a polarized pulse (along x-axis), we have

$$\mathbf{E}(\mathbf{r}, t) = \frac{\hat{x}}{2} E(\mathbf{r}, t) + c.c. = \frac{\hat{x}}{2} U(\mathbf{r}, t) e^{i(\beta_0 z - \omega_0 t)} + c.c., \tag{A.15}$$

where $\hat{x}$ is a unit vector along x-axis, ω_0 is the central angular frequency of $\mathbf{E}$, U is the envelope and $\beta_0 = \beta(\omega_0)$ is the propagation constant at ω_0. Thus

$$\begin{aligned} \frac{\hat{x}}{2} P_{\mathrm{NL}}(\mathbf{r}, t) + c.c. &= \mathbf{P}_{\mathrm{NL}}(\mathbf{r}, t) \\ &= \hat{x} \epsilon_0 \chi^{(3)}_{xxxx} \left[\frac{1}{2} U(\mathbf{r}, t) e^{i[\beta_0 z - \omega_0 t]} + c.c. \right]^3 \\ &= \frac{\hat{x}}{2} \epsilon_0 \chi^{(3)}_{xxxx} \left[\frac{3}{4} |U(\mathbf{r}, t)|^2 U(\mathbf{r}, t) e^{i[\beta_0 z - \omega_0 t]} + \frac{1}{4} U(\mathbf{r}, t)^3 e^{i[3\beta_0 z - 3\omega_0 t]} \right] + c.c., \end{aligned} \tag{A.16}$$

where terms with $\chi^{(3)}_{yxxx}$ and $\chi^{(3)}_{zxxx}$ are ignored. Here, the wave with $3\omega_0$ can be ignored in practice due to the phase mismatch, which leads to

$$P_{\mathrm{NL}}(\mathbf{r}, t) = \epsilon_0 \epsilon_{\mathrm{NL}}(\mathbf{r}, t) E(\mathbf{r}, t) \tag{A.17}$$

with

$$\epsilon_{\mathrm{NL}}(\mathbf{r}, t) = \frac{3}{4} \chi^{(3)}_{xxxx} |U(\mathbf{r}, t)|^2. \tag{A.18}$$

And in the frequency domain,

$$\tilde{P}_{\mathrm{NL}}(\mathbf{r}, \omega) \approx \epsilon_0 \epsilon_{\mathrm{NL}}(\mathbf{r}, t) \tilde{E}(\mathbf{r}, \omega). \tag{A.19}$$

Finally, from Eq. (A.11), we obtain

$$\nabla^2 \tilde{E}(\mathbf{r},\omega) + \epsilon(\omega)\frac{\omega^2}{c^2}\tilde{E}(\mathbf{r},\omega) = 0, \tag{A.20}$$

where

$$\epsilon(\omega) = 1 + \chi^{(1)}_{xx}(\omega) + \epsilon_{\mathrm{NL}}. \tag{A.21}$$

In considering the relation between $E(\mathbf{r},\omega)$ and $U(\mathbf{r},\omega)$ as follows,

$$\tilde{E}(\mathbf{r},\omega) = \tilde{U}(\mathbf{r},\omega-\omega_0)e^{i\beta_0 z}, \tag{A.22}$$

substituting this relation into Eq. (A.20), we obtain the equation of the envelope function in frequency domain as follows,

$$\nabla^2\tilde{U}(\mathbf{r},\omega-\omega_0) + 2i\beta_0\frac{\partial\tilde{U}(\mathbf{r},\omega-\omega_0)}{\partial z} + \left[\epsilon(\omega)\frac{\omega^2}{c^2} - \beta_0^2\right]\tilde{U}(\mathbf{r},\omega-\omega_0) = 0. \tag{A.23}$$

Performing the separation of variables as follows:

$$U(x,y,z,t) = F(x,y)A(z,t), \tag{A.24}$$

we can rewrite several variables,

$$\tilde{U}(\mathbf{r},\omega) = F(x,y)\tilde{A}(z,\omega), \tag{A.25a}$$

$$E(\mathbf{r},t) = F(x,y)A(z,t)e^{i[\beta_0 z-\omega_0 t]}, \tag{A.25b}$$

$$\tilde{E}(\mathbf{r},\omega) = F(x,y)\tilde{A}(z,\omega-\omega_0)e^{i\beta_0 z}. \tag{A.25c}$$

Either substituting Eq. (A.25a) into Eq. (A.23) or substituting Eq. (A.25c) into Eq. (A.20) gives

$$\frac{\partial_x^2F(x,y)+\partial_y^2F(x,y)}{F(x,y)} + \frac{\partial_z^2\tilde{A}(z,\omega-\omega_0)}{\tilde{A}(z,\omega-\omega_0)} + 2i\beta_0\frac{\partial_z\tilde{A}(z,\omega-\omega_0)}{\tilde{A}(z,\omega-\omega_0)} + \epsilon(\omega)\frac{\omega^2}{c^2} - \beta_0^2 = 0. \tag{A.26}$$

Then we can introduce a space-independent parameter $\lambda(\omega)$ to obtain

$$\partial_x^2F(x,y) + \partial_y^2F(x,y) + \left[\epsilon(\omega)\frac{\omega^2}{c^2} - \lambda(\omega)^2\right]F(x,y) = 0, \tag{A.27a}$$

$$\partial_z^2\tilde{A}(z,\omega-\omega_0) + 2i\beta_0\partial_z\tilde{A}(z,\omega-\omega_0) + \left[\lambda(\omega)^2-\beta_0^2\right]\tilde{A}(z,\omega-\omega_0) = 0. \tag{A.27b}$$

Here, λ can be solved as an eigenvalue problem by Eq. (A.27a), and reads

$$\lambda(\omega) \approx \beta(\omega) + i\frac{\alpha}{2} + \beta_{\mathrm{NL}}(\omega_0), \tag{A.28}$$

$$\beta_{\mathrm{NL}}(\omega_0) \approx \frac{\omega_0\bar{n}_2\iint|E(\mathbf{r},t)|^2|F(x,y)|^2dxdy}{c\iint|F(x,y)|^2dxdy} = \gamma(\omega_0)|A(z,t)|^2, \tag{A.29}$$

where $\beta(\omega)$ is the propagation constant when ϵ_{NL} and absorbation is not included, α is the linear absorbation coefficient (the nonlinear absorbation is ignored), $\beta_{\mathrm{NL}}(\omega_0)$ is the

order-zero modification, and $\gamma(\omega_0)$ is defined as

$$\gamma(\omega_0) = \frac{\omega_0 \bar{n}_2 \iint |F(x,y)|^4 dxdy}{c \iint |F(x,y)|^2 dxdy}. \tag{A.30}$$

Then with the approximations $\partial_z^2 \tilde{A} \approx 0$ and $\lambda(\omega)^2 - \beta_0^2 \approx 2\beta_0[\lambda(\omega) - \beta_0]$, Eq. (A.27b) becomes

$$\begin{aligned}\partial_z \tilde{A}(z, \omega - \omega_0) &= i\left[\lambda(\omega) - \beta_0\right] \tilde{A}(z, \omega - \omega_0) \\ &= i[\beta(\omega) - \beta_0]\tilde{A}(z, \omega - \omega_0) + i\gamma(\omega_0)|A(z,t)|^2 \tilde{A}(z, \omega - \omega_0) - \frac{\alpha}{2}\tilde{A}(z, \omega - \omega_0),\end{aligned} \tag{A.31}$$

or

$$\partial_z \tilde{A}(z, \omega) = i[\beta(\omega_0 + \omega) - \beta_0]\tilde{A}(z, \omega) + i\gamma(\omega_0)|A(z,t)|^2 \tilde{A}(z, \omega) - \frac{\alpha}{2}\tilde{A}(z, \omega). \tag{A.32}$$

Considering the Taylor series of $\beta(\omega)$ around $\omega = \omega_0$,

$$\beta(\omega) = \beta_0 + \beta_1(\omega_0)(\omega - \omega_0) + \frac{\beta_2(\omega_0)}{2}(\omega - \omega_0)^2 + ... = \sum_{n=0}^{\infty} \frac{\beta_n(\omega_0)}{n!}(\omega - \omega_0)^n, \tag{A.33}$$

and the following correspondence between the frequency and time domain:

$$\beta(\omega) \leftrightarrow \sum_{n=0}^{\infty} \frac{\beta_n(\omega_0)}{n!}(i\partial_t)^n, \tag{A.34}$$

we find the time-domain equation from Eq. A.32 as follows:

$$\frac{\partial A(z,t)}{\partial z} = i\sum_{n=1}^{\infty} \frac{\beta_n(\omega_0)}{n!}(i\partial_t)^n A(z,t) + i\gamma(\omega_0)|A(z,t)|^2 A(z,t) - \frac{\alpha}{2}A(z,t). \tag{A.35}$$

If we define retarted time $t' = t - \beta_1 z$, we have

$$dA = \frac{\partial A}{\partial z}dz + \frac{\partial A}{\partial t}d(t' + \beta_1 z) = (\frac{\partial A}{\partial z} + \beta_1 \frac{\partial A}{\partial t})dz + \frac{\partial A}{\partial t}dt', \tag{A.36}$$

so that if we use z and t' as the independent variables, i.e. $A = A'(z, t')$, we find

$$\frac{\partial A'}{\partial z} = \frac{\partial A}{\partial z} + \beta_1 \frac{\partial A}{\partial t}, \quad \frac{\partial A'}{\partial t'} = \frac{\partial A}{\partial t}. \tag{A.37}$$

Thus Eq. (A.35) can be rewritten as

$$\frac{\partial A'(z,t')}{\partial z} = i\sum_{n=2}^{\infty} \frac{\beta_n(\omega_0)}{n!}(i\partial_t')^n A'(z,t') + i\gamma(\omega_0)|A'(z,t')|^2 A'(z,t') - \frac{\alpha}{2}A'(z,t'), \tag{A.38}$$

Here, the summation starts from 2. The most common NLSE truncates the summation at $n = 2$.

Appendix B

Split-Step Fourier Method

The Split-Step Fourier Method (SSFM) is a numerical technique for solving partial differential equations of the general form [9]

$$\frac{\partial A(z,t)}{\partial z} = \left(\hat{D} + \hat{N}\right) A(z,t), \tag{B.1}$$

where $A(z,t)$ is the complex field envelope, $\hat{D}$ represents the linear dispersive operator, and $\hat{N}$ denotes the nonlinear operator. This form is typical in equations such as the nonlinear Schrödinger equation.

The key idea of the SSFM is to approximate the evolution over a small step Δz by splitting the linear and nonlinear parts, treating each separately:

$$A(z+\Delta z,t) \approx e^{\hat{D}\Delta z/2} e^{\hat{N}\Delta z} e^{\hat{D}\Delta z/2} A(z,t) + \mathcal{O}(\Delta z^3), \tag{B.2}$$

which is accurate to second order in Δz using the symmetric splitting.

B.1 Linear Step

The linear operator $\hat{D}$ often involves derivatives in time t, such as

$$\hat{D} = -i\frac{\beta_2}{2}\frac{\partial^2}{\partial t^2}, \tag{B.3}$$

for the case of second-order dispersion. This term is evaluated in the Fourier domain, where derivatives become multiplications,

$$\mathcal{F}\left[\frac{\partial^2 A}{\partial t^2}\right] = -(2\pi f)^2 \tilde{A}(f), \tag{B.4}$$

where $\mathcal{F}[\cdot]$ represents Fouier transform and f is frequency, so the linear propagation becomes

$$\tilde{A}(z+\Delta z, f) = \tilde{A}(z,f) \exp\left(-i\frac{\beta_2}{2}(2\pi f)^2 \Delta z\right). \tag{B.5}$$

B.2 Nonlinear Step

The nonlinear operator $\hat{N}$ is applied in the time domain and may include terms like

$$\hat{N} = i\gamma|A(z,t)|^2. \tag{B.6}$$

This gives the nonlinear update as follows:

$$A(z+\Delta z,t) = A(z,t)\exp\left(i\gamma|A(z,t)|^2\Delta z\right). \tag{B.7}$$

B.3 Algorithm Summary

The SSFM proceeds as follows for each propagation step Δz:

1. Linear half-step: Apply $\exp(\hat{D}\Delta z/2)$ in Fourier space.
2. Nonlinear full-step: Apply $\exp(\hat{N}\Delta z)$ in time domain.
3. Linear half-step: Apply $\exp(\hat{D}\Delta z/2)$ in Fourier space again.

This approach exploits the efficiency of the Fast Fourier Transform (FFT) to handle the dispersive terms, making the SSFM especially suitable for simulating long-distance wave propagation in nonlinear media. SSFM can also be extended to generalised forms of the NLSE featuring additional terms, such as LLE and parametrically driven NLSE discussed in this thesis.

Appendix C

Other results on asymmetrically pumped dual-core OPA

C.1 Mathematical analysis of the asymmetric gain

As stated in the main text, the amplitude of the supermodes as a function of z, $E_{\pm}(z)$, can be obtained by solving the following equation,

$$\partial_z(e_{s+}, e_{i+}, e_{s-}, e_{i-})^T = iM(e_{s+}, e_{i+}, e_{s-}, e_{i-})^T, \tag{C.1}$$

whose solution is

$$(e_{s+}, e_{i+}, e_{s-}, e_{i-})^T = \sum_{j=1}^{4} a_j \mathbf{v}_j e^{i\lambda_j z}, \tag{C.2}$$

where λ_j and $\mathbf{v}_j$ are respectively the eigenvalues and eigenvectors of matrix M, and the coefficients a_j are determined by the initial conditions as

$$(a_1, a_2, a_3, a_4)^T = (\mathbf{v}_1, \mathbf{v}_2, \mathbf{v}_3, \mathbf{v}_4)^{-1}(e_{s+}, e_{i+}, e_{s-}, e_{i-})^T. \tag{C.3}$$

As an exmaple, we chose the anomalous dispersion case and plotted the imaginary part of four eigenvalues which is shown in Fig. C.1 (a). A nonzero imaginary part of eigenvalues implies gain. Without loss of generality, we assume λ_1 possessing a minimum (negative) imaginary part, then the term $a_1\mathbf{v}_1 e^{i\lambda_1 z}$ becomes dominant for large z, i.e.

$$(e_{s+}, e_{i+}, e_{s-}, e_{i-})^T \approx a_1\mathbf{v}_1 e^{i\lambda_1 z}. \tag{C.4}$$

As a result, assuming that $\mathbf{v}_1 = (v_1, v_2, v_3, v_4)^T$, the gain difference between signals and idlers is given by

$$G_{\pm}^{\text{diff}} = 10\log\frac{|e_{s\pm}|^2}{|e_{i\pm}|^2} = 10\log\left|\frac{v_{2\mp1}}{v_{3\mp1}}\right|^2, \tag{C.5}$$

here G_{+}^{diff} refers to supermode "+" while G_{-}^{diff} refers to supermode "-" respectively. As shown in Fig. C.1(b), the gain difference between e_{s-} and e_{i-} at around 5 THz is about 20 dB. In addition, Fig. C.1(c)-(d) show the impact of C_1 on the minimum imaginary part of eigenvalues $\text{Im}(\lambda_1)$ and the gain difference between e_{s-} and e_{i-} respectively. From Fig. C.1(d), we can see that C_1 plays an important role in obtaining asymmetric gain spectrum. In summary, the sign of C_1 and the sign of Ω together determine whether the gain spectrum

of one supermode is idler-free or signal-free. For fixed C_1, one can always adjust the input signal detuning respective to the pump waves or select the output supermode to obtain a supermode with an idler-free gain spectrum.

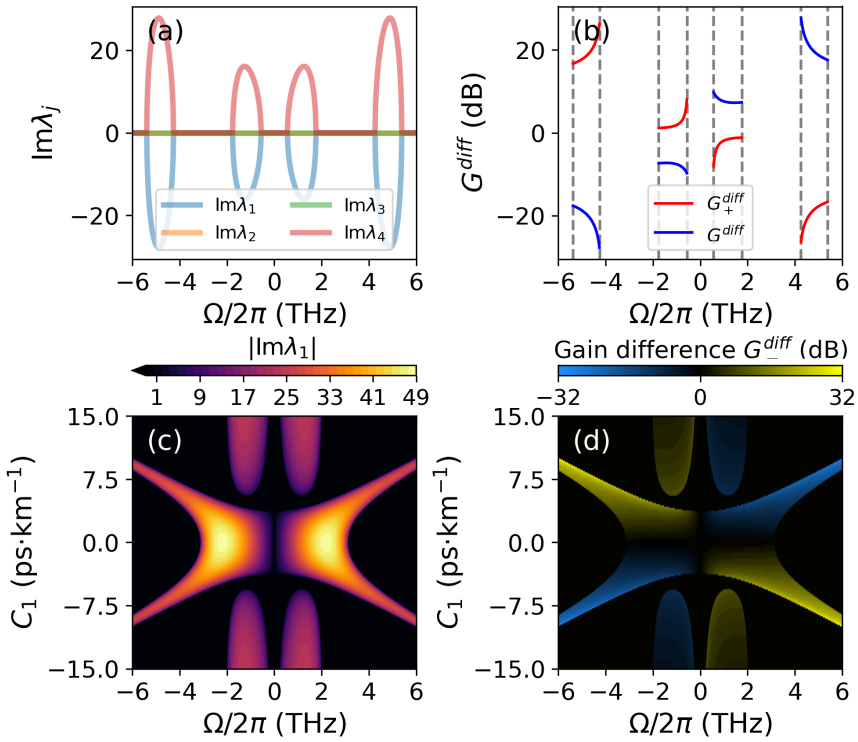

Figure C.1: Eigenvalues and gain difference between signals and idlers estimated by eigenvectors. (a) Imaginary part of eigenvalues; (b) Gain difference estimated through eigenvectors. (c) Map of the absolute value of the eigenvalues minimum imaginary part versus frequency and C_1. (d) Map of estimated gain difference between e_{s-} and e_{i-} versus frequency and C_1. Parameters used are $\beta_2 = \mp 0.5$ ps^{2}km^{-1}, $\gamma = 10$ W^{-1}km^{-1}, $P_p = 5.4$ W, $C_0 = 15$ km^{-1}, $C_2 = 0$, and $z = 0.1$ km. The value of C_1 in in (a) and (b) is -7.5ps $\cdot$ km^{-1} . Note that $\mathrm{Im}(\lambda_2) = 0$ everywhere and its line is covered by $\mathrm{Im}(\lambda_3)$.

C.2 Gain spectrum of individual waveguides modes

To have a direct understanding of how the separation of signals and idlers between different supermodes is produced, we simulated the PI amplifier for individual waves in two waveguides and the results are shown in Fig. C.2. We can see that the gain is almost symmetric for $C_1 = -7.5$ ps $\cdot$ km^{-1}. In addition, the phase difference between two individual modes is shown in Fig. C.3, from which, it is clear that the idlers (frequency range between -6 and -4 THz) have a phase difference close to zero, whereas the signals (frequency range between +4 and +6 THz) have relative phase close to π. As a result, the two supermodes are one idler-free and the other one signal free respectively.

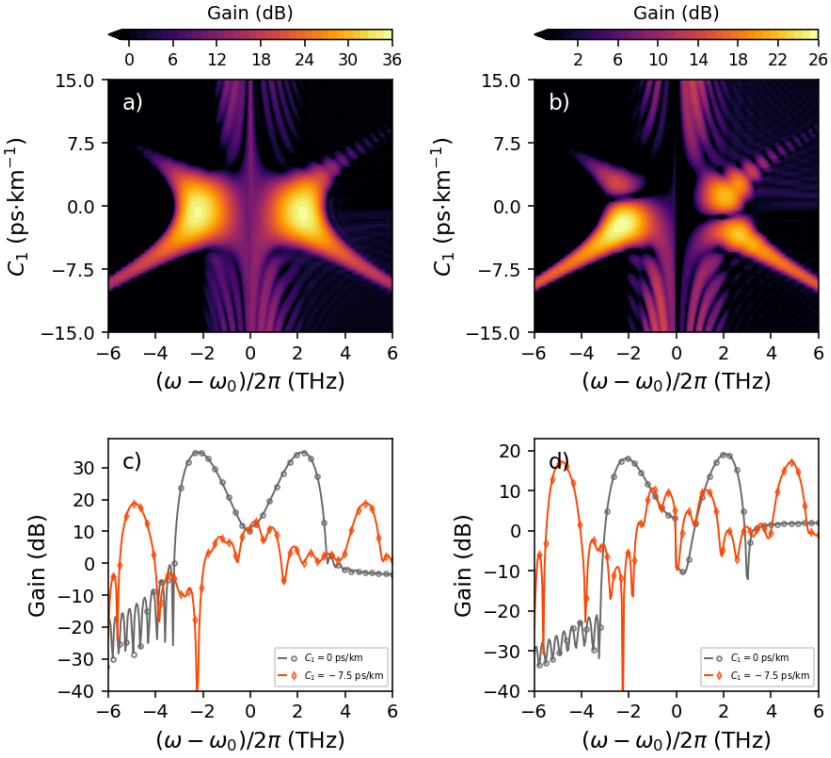

Figure C.2: PI amplifier for individual modes. (a) and (b) Map of parametric analytical gain versus frequency and C_1 in anomalous dispersion regime for waveguide 1 and 2 respectively; (c) and (d) comparison of gain spectrum versus frequency between theory (continuous line) and numerics (dots) for anomalous dispersion regime with $C_1 = -7.5$ ps$\cdot$km^{-1} for waveguide 1 and 2 respectively. Parameters used are $\beta_2 = \mp 0.5$ ps^{2}km^{-1}, $\gamma = 10$ W^{-1}km^{-1}, $P_p = 5.4$ W, $C_0 = 15$ km^{-1}, $C_2 = 0$, and $z = 0.1$ km.

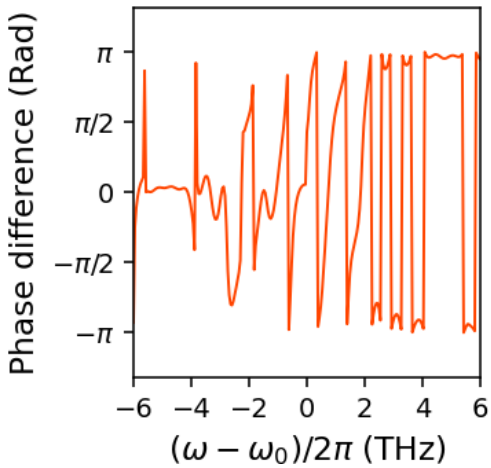

Figure C.3: Phase difference of two individual modes. Here $C_1 = -7.5$ ps$\cdot$km^{-1} and other parameters used are like in Fig. C.2.